

Theoretical investigations of the spin-1/2
triangular lattice antiferromagnet Cs_2CuCl_4 in
the spin-liquid and high-magnetic-field regimes

Dissertation
zur Erlangung des Doktorgrades
der Naturwissenschaften

vorgelegt beim Fachbereich Physik der
Johann Wolfgang Goethe-Universität
in Frankfurt am Main

von
Simon Streib
aus
Frankfurt am Main

Frankfurt (2016)
(D30)

vom Fachbereich Physik der
Johann Wolfgang Goethe-Universität
als Dissertation angenommen.

Dekan: Prof. Dr. René Reifarth

Gutachter: Prof. Dr. Peter Kopietz
Prof. Dr. Roser Valentí
Prof. Dr. Götz Uhrig

Datum der Disputation: 11.01.2016

Science is the belief in the ignorance of experts.

— Richard P. Feynman, *What Is Science*, Phys. Teach. **7**, 313 (1969)

Alle Wissenschaft hat nach unserer Auffassung die Function Erfahrung zuersetzen. Sie muss daher zwar einerseits in dem Gebiete der Erfahrung bleiben, eilt aber doch andererseits der Erfahrung voraus, stets einer Bestätigung aber auch Widerlegung gegenwärtig. Wo weder eine Bestätigung noch eine Widerlegung möglich ist, dort hat die Wissenschaft nichts zu schaffen. Sie bewegt sich immer nur auf dem Gebiete der unvollständigen Erfahrung.

— Ernst Mach, *Die Mechanik in ihrer Entwicklung* (1883)

Contents

Abstract	7
Inhaltsangabe	9
1 Introduction	11
1.1 Cs_2CuCl_4	11
1.1.1 Effective Hamiltonian	11
1.1.2 Exchange and Dzyaloshinskii-Moriya interactions	13
1.1.3 Phase diagram	14
1.2 Representations of the spin-1/2 operators	15
1.2.1 Holstein-Primakoff transformation	16
1.2.2 Jordan-Wigner transformation	16
1.2.3 Hard-core bosons	17
1.2.4 Majorana fermions	18
1.2.5 Abrikosov pseudofermions	18
1.3 Hartree-Fock and mean-field approximations	19
1.4 Diagrammatic methods	20
1.4.1 Path integral formalism and Wick's theorem	20
1.4.2 One-particle Green function and self-energy	22
1.4.3 Feynman diagram representation of the self-energy	22
1.4.4 Calculation of Matsubara sums	23
1.4.5 Origin of the convergence factor	25
1.4.6 Convergence of the partition function	26
2 Majorana spin-liquid and dimensional reduction	29
2.1 Introduction	29
2.2 Rotationally invariant Majorana mean-field theory	30
2.3 Majorana mean-field theory in a magnetic field	38
2.4 Summary and conclusions	43
3 Ultrasound properties of the spin-liquid phase	45
3.1 Introduction	45
3.2 Spin-phonon model	46
3.3 Jordan-Wigner transformation and Hartree-Fock approximation	47
3.4 Phonon self-energy	49

3.5	Summary and conclusions	55
4	Hard-core boson approach in high magnetic fields	57
4.1	Introduction	57
4.2	Hard-core boson model for Cs_2CuCl_4	58
4.3	Implementing the self-consistent ladder approximation	60
4.3.1	Hartree-Fock decoupling	61
4.3.2	Self-consistent ladder approximation	62
4.4	Numerical results for the one-dimensional XY model	68
4.5	Numerical results for Cs_2CuCl_4	70
4.5.1	Spectral function	71
4.5.2	Magnetic moment and magnetic susceptibility	73
4.5.3	Internal energy and specific heat	74
4.6	Summary and conclusions	78
A	Phonon energy and damping from the phonon self-energy	79
B	Numerical details	81
B.1	Calculation of the spectral function	81
B.2	Brillouin zone discretization	82
C	Spin mean-field approximation	85
D	Deutsche Zusammenfassung	87
D.1	Majorana-Spinflüssigkeit und dimensionale Reduktion	90
D.2	Ultraschallphysik in der Spinflüssigkeitsphase	96
D.3	Hardcore-Boson-Ansatz in starken Magnetfeldern	103
Publications		113
Bibliography		115
Danksagung		123
Lebenslauf		125

Abstract

The phenomenon of magnetism has been known to humankind for at least over 2500 years and many useful applications of magnetism have been developed since then, starting from the compass to modern information storage and processing devices. While technological applications are an important part of the continuing interest in magnetic materials, their fundamental properties are still being studied, leading to new physical insights at the forefront of physics. The magnetism of magnetic materials is a pure quantum effect due to the electrons that carry an intrinsic spin of 1/2. The physics of interacting quantum spins in magnetic insulators is the main subject of this thesis.

We focus here on a theoretical description of the antiferromagnetic insulator Cs_2CuCl_4 . This material is highly interesting because it is a nearly ideal realization of the two-dimensional antiferromagnetic spin-1/2 Heisenberg model on an anisotropic triangular lattice, where the Cu^{2+} ions carry a spin of 1/2 and the spins interact via exchange couplings. Due to the geometric frustration of the triangular lattice, there exists a spin-liquid phase with fractional excitations (spinons) at finite temperatures in Cs_2CuCl_4 . This spin-liquid phase is characterized by strong short-range spin correlations without long-range order. From an experimental point of view, Cs_2CuCl_4 is also very interesting because the exchange couplings are relatively weak leading to a saturation field of only $B_c \approx 8.5$ T. All relevant parts of the phase diagram are therefore experimentally accessible. A recurring theme in this thesis will be the use of bosonic or fermionic representations of the spin operators which each offer in different situations suitable starting points for an approximate treatment of the spin interactions. The methods which we develop in this thesis are not restricted to Cs_2CuCl_4 but can also be applied to other materials that can be described by the spin-1/2 Heisenberg model on a triangular lattice; one important example is the material class $\text{Cs}_2\text{Cu}(\text{Cl}_{4-x}\text{Br}_x)$ where chlorine is partially substituted by bromine which changes the strength of the exchange couplings and the degree of frustration.

Our first topic is the finite-temperature spin-liquid phase in Cs_2CuCl_4 . We study this regime by using a Majorana fermion representation of the spin-1/2 operators motivated by theoretical and experimental evidence for fermionic excitations in this spin-liquid phase. Within a mean-field theory for the Majorana fermions, we determine the magnetic field dependence of the critical temperature for the crossover from spin-liquid to paramagnetic behavior and

we calculate the specific heat and magnetic susceptibility in zero magnetic field. We find that the Majorana fermions can only propagate in one dimension along the direction of the strongest exchange coupling; this reduction of the effective dimensionality of excitations is known as dimensional reduction.

The second topic is the behavior of ultrasound propagation and attenuation in the spin-liquid phase of Cs_2CuCl_4 , where we consider longitudinal sound waves along the direction of the strongest exchange coupling. Due to the dimensional reduction of the excitations in the spin-liquid phase, we expect that we can describe the ultrasound physics by a one-dimensional Heisenberg model coupled to the lattice degrees of freedom via the exchange-striction mechanism. For this one-dimensional problem we use the Jordan-Wigner transformation to map the spin-1/2 operators to spinless fermions. We treat the fermions within the self-consistent Hartree-Fock approximation and we calculate the change of the sound velocity and attenuation as a function of magnetic field using a perturbative expansion in the spin-phonon couplings. We compare our theoretical results with experimental data from ultrasound experiments, where we find good agreement between theory and experiment.

Our final topic is the behavior of Cs_2CuCl_4 in high magnetic fields larger than the saturation field $B_c \approx 8.5$ T. At zero temperature, Cs_2CuCl_4 is then fully magnetized and the ground state is therefore a ferromagnet where the excitations have an energy gap. The elementary excitations of this ferromagnetic state are spin-flips (magnons) which behave as hard-core bosons. At finite temperatures there will be thermally excited magnons that interact via the hard-core interaction and via additional exchange interactions. We describe the thermodynamic properties of Cs_2CuCl_4 at finite temperatures and calculate experimentally observable quantities, e.g., magnetic susceptibility and specific heat. Our approach is based on a mapping of the spin-1/2 operators to hard-core bosons, where we treat the hard-core interaction by the self-consistent ladder approximation and the exchange interactions by the self-consistent Hartree-Fock approximation. We find that our theoretical results for the specific heat are in good agreement with the available experimental data.

Inhaltsangabe

Magnetische Phänomene sind der Menschheit schon seit mindestens über 2500 Jahren bekannt und viele nützliche Anwendungen von magnetischen Eigenschaften sind seitdem entwickelt worden, angefangen beim Kompass bis zu modernen Anwendungen in der Datenspeicherung und -verarbeitung. Während technologische Anwendungen ein wichtiger Grund für das andauernde Interesse an magnetischen Materialien sind, so werden auch weiterhin deren fundamentale Eigenschaften untersucht, was immer wieder zu neuen, grundlegenden physikalischen Erkenntnissen geführt hat. Der Magnetismus von magnetischen Materialien ist ein reiner Quanteneffekt, verursacht durch die Elektronen, die einen intrinsischen Spin von $1/2$ haben. Das Hauptthema dieser Dissertation ist die Physik von wechselwirkenden Quantenspins in magnetischen Isolatoren.

Wir konzentrieren uns dabei auf eine theoretische Beschreibung des antiferromagnetischen Isolators Cs_2CuCl_4 . Dieses Material ist interessant, da es eine nahezu ideale Realisierung eines zweidimensionalen, antiferromagnetischen Spin- $1/2$ -Heisenberg-Modells auf einem anisotropen Dreiecksgitter darstellt, wobei die Cu^{2+} -Ionen einen Spin von $1/2$ haben und über Austauschkopplungen miteinander wechselwirken. Aufgrund der geometrischen Frustration des Dreiecksgitters existiert in Cs_2CuCl_4 eine Spinflüssigkeitsphase mit fraktionalen Anregungen (Spinonen) bei endlichen Temperaturen. Das Hauptmerkmal der Spinflüssigkeitsphase sind starke, kurzreichweitige Spinkorrelation ohne langreichweite Ordnung. Cs_2CuCl_4 ist auch aus experimenteller Sicht besonders interessant, da die Austauschkopplungen relativ schwach sind, wodurch das Saturierungsfeld bei nur $B_c \approx 8.5$ T liegt. Damit sind alle relevanten Bereiche des Phasendiagramms experimentell erreichbar. Ein wiederkehrendes Thema in dieser Dissertation wird die Verwendung von bosonischen oder fermionischen Darstellungen der Spinoperatoren sein, die jeweils für verschiedene Situationen geeignete Ausgangspunkte für eine genäherte Beschreibung der Spinwechselwirkungen darstellen. Die Methoden, die wir in dieser Arbeit entwickeln, sind dabei nicht auf Cs_2CuCl_4 beschränkt, sondern können auch auf andere Materialien angewendet werden, die durch ein Spin- $1/2$ -Heisenberg-Modell auf einem Dreiecksgitter beschrieben werden können, wobei ein wichtiges Beispiel die Materialklasse $\text{Cs}_2\text{Cu}(\text{Cl}_{4-x}\text{Br}_x)$ ist, bei der Chlor teilweise durch Brom substituiert wird, wodurch die Stärke der Austauschkopplungen und die Frustration variiert werden können.

Das erste Thema dieser Arbeit ist die Spinflüssigkeitsphase in Cs_2CuCl_4

bei endlichen Temperaturen. Wir untersuchen diese Phase, indem wir die Majorana-Fermion-Darstellung der Spin-1/2-Operatoren verwenden, was motiviert wird durch theoretische und experimentelle Hinweise auf fermionische Anregungen in dieser Spinflüssigkeitsphase. Im Rahmen einer Meanfield-Theorie für die Majorana-Fermionen bestimmen wir die Magnetfeldabhängigkeit der kritischen Temperatur für den Übergang von der Spinflüssigkeitsphase zur paramagnetischen Phase und wir berechnen die spezifische Wärme und magnetische Suszeptibilität für den Fall, dass kein externes Magnetfeld anliegt. Ein zentrales Ergebnis ist, dass die Majorana-Fermionen nur in einer Dimension entlang der Richtung der stärksten Austauschkopplung propagieren können; dieser Effekt ist unter dem Begriff der dimensionalen Reduktion bekannt.

Unser zweites Thema ist das Verhalten von Ultraschallausbreitung und -dämpfung in der Spinflüssigkeitsphase von Cs_2CuCl_4 . Wir betrachten longitudinale Schallwellen entlang der Richtung der stärksten Austauschkopplung. Aufgrund der dimensionalen Reduktion der Anregungen in der Spinflüssigkeitsphase erwarten wir, dass wir die Ultraschallphysik mit einem eindimensionalen Heisenberg-Modell beschreiben können, bei dem die Spinfreiheitsgrade an die Gitterschwingungen gekoppelt sind. Für dieses eindimensionale Problem verwenden wir die Jordan-Wigner-Transformation, um die Spin-1/2-Operatoren auf spinlose Fermionen abzubilden. Wir behandeln die Fermionen im Rahmen einer selbstkonsistenten Hartree-Fock-Näherung und wir berechnen die Änderung der Schallgeschwindigkeit und -dämpfung als Funktion des Magnetfeldes, indem wir eine Störungsentwicklung in den Spin-Phonon-Kopplungen durchführen. Dabei vergleichen wir unsere Ergebnisse mit experimentellen Daten aus Ultraschallexperimenten, wobei wir eine gute Übereinstimmung finden.

Das letzte Thema ist das Verhalten von Cs_2CuCl_4 in starken Magnetfeldern oberhalb des Saturierungsfeldes $B_c \approx 8.5$ T. Am Temperaturnullpunkt ist Cs_2CuCl_4 dann vollständig magnetisiert und der Grundzustand ist damit ein Ferromagnet, dessen Anregungen eine Energielücke zum Grundzustand aufweisen. Die elementaren Anregungen dieses ferromagnetischen Zustands sind Spinflips (Magnonen), die sich wie Hardcore-Bosonen verhalten. Bei endlichen Temperaturen werden thermisch angeregte Magnonen auftreten, die miteinander über die Hardcore-Wechselwirkung und Austauschkopplungen wechselwirken. Wir beschreiben die thermodynamischen Eigenschaften von Cs_2CuCl_4 bei endlichen Temperaturen und berechnen experimentell beobachtbare Größen, z.B. die magnetische Suszeptibilität und die spezifische Wärme. Dazu bilden wir die Spin-1/2-Operatoren auf Hardcore-Bosonen ab und behandeln die Hardcore-Wechselwirkung mit der selbstkonsistenten Leiternäherung und die Austauschkopplungen mit der selbstkonsistenten Hartree-Fock-Näherung. Unsere theoretischen Ergebnisse für die spezifische Wärme stimmen gut mit den vorhandenen experimentellen Daten überein.

Chapter 1

Introduction

1.1 Cs_2CuCl_4

Since the main topic of this thesis is the theoretical description of Cs_2CuCl_4 , we start by introducing the main properties of this material. Cs_2CuCl_4 is an antiferromagnetic insulator with an orthorhombic crystal structure (*Pnma*) and lattice parameters $a = 9.65 \text{ \AA}$, $b = 7.48 \text{ \AA}$, and $c = 12.26 \text{ \AA}$ (at $T = 0.3 \text{ K}$ [1]). The CuCl_4^{2-} tetrahedra form triangular lattices in the bc planes and are separated by Cs^{2+} ions along the a axis. The Cu^{2+} ions carry each a spin of $1/2$ where the spins are isotropic Heisenberg spins because the orbital momentum is quenched by strong crystal fields. The electrons that carry the spin of $1/2$ at the Cu^{2+} lattice sites are localized due to a strong on-site repulsion which means that Cs_2CuCl_4 is a Mott insulator where the spins interact via super-exchange routes mediated by the non-magnetic Cl^- ions. Cs_2CuCl_4 has been intensively studied due to its interesting properties, e.g., spin-liquid behavior with spinon excitations [P2, 1–12], Bose-Einstein condensation of magnons at the quantum critical point [13–17], and a rich phase diagram for in-plane magnetic fields [2, 18–23]. In the past two decades, the physical properties of Cs_2CuCl_4 have been explored experimentally by investigating a diverse range of observables: dynamic structure factor [1, 2, 13], electron spin resonance spectra [24], magnetic susceptibility [19], magneto-caloric effect [25], nuclear magnetic resonance relaxation rate [11], specific heat [14, 15], and ultrasound velocity and attenuation [P3, 26, 27].

1.1.1 Effective Hamiltonian

It has been established that the magnetic behavior of Cs_2CuCl_4 can be described by the following two-dimensional antiferromagnetic spin- $1/2$ Heisenberg model in an external magnetic field along the crystallographic a axis [13],

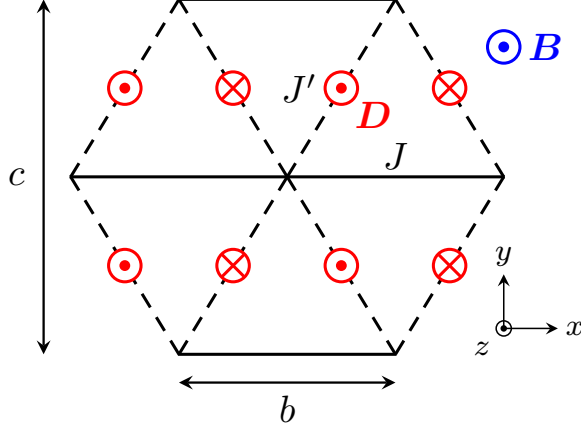


Figure 1.1: Part of the anisotropic triangular lattice formed by the spins of Cs_2CuCl_4 . The stronger exchange coupling J connects nearest-neighbor spins along the crystallographic b axis, while the weaker exchange coupling J' connects nearest-neighbor spins along the diagonals. There are also weak Dzyaloshinskii-Moriya interactions $\mathbf{D} = \pm D\hat{z}$ connecting neighboring spins along the diagonals where the direction of \mathbf{D} is indicated by \odot for $+\hat{z}$ and \otimes for $-\hat{z}$. We consider only the case where the magnetic field $\mathbf{B} = B\hat{z}$ is along the a axis perpendicular to the plane of the lattice.

$$\mathcal{H} = \frac{1}{2} \sum_{ij} [J_{ij} \mathbf{S}_i \cdot \mathbf{S}_j + \mathbf{D}_{ij} \cdot (\mathbf{S}_i \times \mathbf{S}_j)] - h \sum_i S_i^z, \quad (1.1)$$

where the summations run over all N lattice sites, $h = g\mu_B B$ is the Zeeman energy associated with an external magnetic field $\mathbf{B} = B\hat{z}$, and $g = 2.19(1)$ is the effective g -factor [13]. The spin-1/2 operators $\mathbf{S}_i = \mathbf{S}(\mathbf{R}_i)$ are located at the lattice sites \mathbf{R}_i of an anisotropic triangular lattice with lattice constants b and c , as shown in Fig. 1.1. The exchange couplings $J_{ij} = J(\mathbf{R}_i - \mathbf{R}_j)$ connect nearest neighbors along the crystallographic b axis and along the diagonals with $J(\pm\delta_1) = J$ and $J(\pm\delta_2) = J(\pm\delta_3) = J'$, where the three elementary lattice vectors are (see Fig. 2.1 in the following chapter)

$$\delta_1 = b\hat{x}, \quad \delta_2 = -\frac{b}{2}\hat{x} + \frac{c}{2}\hat{y}, \quad \delta_3 = -\frac{b}{2}\hat{x} - \frac{c}{2}\hat{y}. \quad (1.2)$$

Here, \hat{x} , \hat{y} , and \hat{z} are the unit vectors of our Cartesian coordinate system. Due to the fact that inversion symmetry is broken for Cs_2CuCl_4 , there are also Dzyaloshinskii-Moriya interactions $\mathbf{D}_{ij} = D(\mathbf{R}_i - \mathbf{R}_j)\hat{z}$ connecting neighboring spins along the diagonals with $D(\pm\delta_2) = D(\pm\delta_3) = \mp D$. The precise form of the Hamiltonian (1.1) and the values of the interaction constants have been measured by inelastic neutron scattering experiments in magnetic fields higher than the saturation field $B_c = 8.44(1)$ T. The accepted values are [13]: $J = 0.374(5)$ meV = 4.34(6) K, $J'/J = 0.34(3)$, and $D/J = 0.053(5)$. There is also a weak interlayer coupling $J''/J = 0.045(5)$, which we neglect because it is only

important at very low temperatures $T \lesssim 0.1$ K and in the antiferromagnetically ordered phase in magnetic fields $B < B_c$ which we do not consider in this thesis. We mention here that the methods which we develop in this thesis are not restricted to Cs₂CuCl₄ but can also be applied to other materials that can be described by the spin-1/2 Heisenberg model (1.1). The most important example is the material class Cs₂Cu(Cl_{4-x}Br_x), where chlorine is partially substituted by bromine which changes the strength of the exchange couplings and the ratio J'/J [28–31].

1.1.2 Exchange and Dzyaloshinskii-Moriya interactions

The exchange interactions between the spins in the Hamiltonian (1.1) are of quantum mechanical origin and are due to the Pauli principle and the strong Coulomb repulsion between the electrons. The dipole-dipole interactions due to the magnetic dipole moments of the electrons are much smaller and can be neglected. The spin-1/2 Heisenberg model can be derived from the Hubbard model in the strong-coupling limit. In the simplest case, the Hubbard model describes electrons on a lattice interacting via a repulsive on-site interaction $U > 0$,

$$\mathcal{H} = \sum_{ij,\sigma} t_{ij} c_{i\sigma}^\dagger c_{j\sigma} + U \sum_i c_{i\uparrow}^\dagger c_{i\uparrow} c_{i\downarrow}^\dagger c_{i\downarrow}, \quad (1.3)$$

where $c_{i\sigma}^\dagger$ and $c_{i\sigma}$ are the creation and annihilation operators of fermions with spin σ at lattice site i . At half filling (one electron per lattice site), the Hubbard model can be mapped in the strong-coupling Mott limit, $U \gg t_{ij}$, to the spin-1/2 Heisenberg model [32],

$$\mathcal{H} = \frac{1}{2} \sum_{ij} J_{ij} \left(\mathbf{S}_i \cdot \mathbf{S}_j - \frac{1}{4} \right), \quad (1.4)$$

with exchange couplings $J_{ij} = 4|t_{ij}|^2/U$. If we apply an external magnetic field to the Hubbard model, there will be two effects. There will be the Zeeman energy $-h \sum_i S_i^z$ and the hopping matrix elements t_{ij} will acquire a Peierls phase, $t_{ij} \rightarrow t_{ij} e^{i\lambda_{ij}}$ [32]. This implies that the exchange couplings J_{ij} do not change when a magnetic field is applied because they do not depend on the phase of t_{ij} . In the case of Cs₂CuCl₄ we do not have direct exchange interactions, but super-exchange interactions, where the hopping processes are not directly from one Cu²⁺ site to the next but are mediated by the non-magnetic Cl⁻ sites. For a microscopic derivation of the effective Hamiltonian of Cs₂CuCl₄ via *ab initio* methods, we refer to Ref. [30].

In Cs₂CuCl₄ the inversion symmetry is broken, allowing Dzyaloshinskii-Moriya (DM) interactions [33, 34] which are antisymmetric exchange interactions given by

$$\mathcal{H}_{\text{DM}} = \frac{1}{2} \sum_{ij} \mathbf{D}_{ij} \cdot (\mathbf{S}_i \times \mathbf{S}_j). \quad (1.5)$$

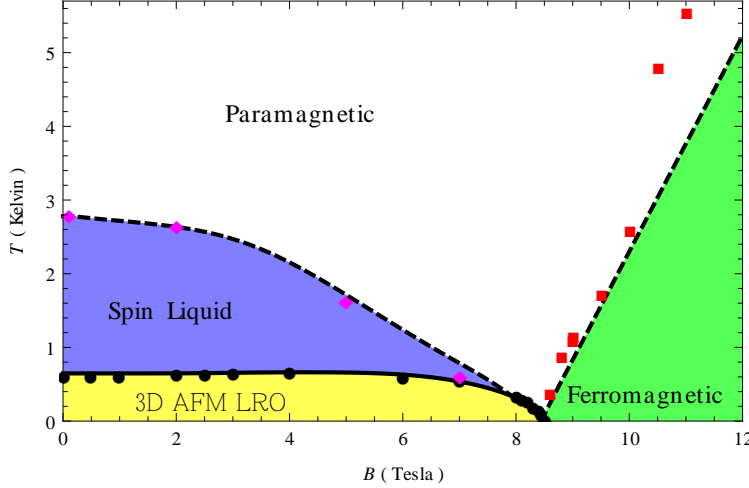


Figure 1.2: Schematic phase diagram of Cs_2CuCl_4 (redrawn from Fig. 1 of Ref. [1]) as a function of temperature T and an external magnetic field $B\hat{z}$ along the crystallographic a axis. The experimental data points for the crossover from the paramagnetic to the ferromagnetic phase (squares) and for the phase transition from the ordered to the spin-liquid phase (black circles) have been obtained from Ref. [14], while the experimental data points for the crossover from the spin-liquid to the paramagnetic phase (diamonds) are from Ref. [35].

The components of the antisymmetric exchange couplings \mathbf{D}_{ij} are related to the value of the corresponding exchange coupling J_{ij} and can be estimated as follows [34],

$$|\mathbf{D}_{ij}| \approx \frac{\Delta g}{g} |J_{ij}|, \quad \Delta g = g - 2. \quad (1.6)$$

For Cs_2CuCl_4 the DM interactions are along the diagonals (see Fig. 1.1) with the corresponding exchange coupling $J'/J = 0.34$. With $g = 2.19$, the estimate (1.6) gives $D/J \approx 0.03$ which is not too far off from the measured value $D/J = 0.053(5)$.

1.1.3 Phase diagram

The phase diagram of Cs_2CuCl_4 as a function of the temperature T and an external magnetic field $B\hat{z}$ perpendicular to the plane of the triangular lattice is shown schematically in Fig. 1.2. Strictly speaking, there are only two phases: a paramagnetic phase where the spin-rotational invariance with respect to the z axis is not broken and an antiferromagnetically ordered phase (labeled *3D AFM LRO*) with spontaneously broken spin-rotational invariance. The anti-ferromagnetic phase is stabilized by the interplane interaction J'' and occurs at temperatures below the Néel temperature, which is at zero magnetic field given by $T_N = 0.62(1)$ K [1]. The other two phases indicated in Fig. 1.2

belong to the paramagnetic phase. We partition the paramagnetic phase into three subphases: a spin-liquid phase characterized by strong short-range spin correlations, a ferromagnetic phase where the spins are nearly completely polarized, and a paramagnetic regime. The dashed lines in Fig. 1.2 separating these subphases are not phase transitions but indicate the crossover from one regime to the other. The crossover line from the spin-liquid phase to the paramagnetic regime is determined by the maximum of the magnetic susceptibility which indicates the point at which the spin correlations become important. The crossover line from the ferromagnetic phase to the paramagnetic regime is given by the size of the energy gap $\Delta = g\mu_B(B - B_c)$ where for temperatures below the energy gap the spins are nearly completely polarized. At $T = 0$ and $B = B_c \approx 8.5$ T there is a quantum critical point at the quantum phase transition from the ferromagnetic to the antiferromagnetic phase which can be described as a Bose-Einstein condensation of magnons [13–17].

1.2 Representations of the spin-1/2 operators

The spin-1/2 operators fulfill the commutation relations

$$[S_i^+, S_j^-] = 2\delta_{ij}S_i^z, \quad [S_i^\pm, S_j^z] = \mp\delta_{ij}S_i^\pm, \quad (1.7)$$

where $S_i^\pm = S_i^x \pm iS_i^y$ and $S_i^2 = 3/4$. Additionally, the spin-1/2 operators obey an on-site exclusion principle [36],

$$S_i^+ S_i^- + S_i^- S_i^+ = 1, \quad (S_i^+)^2 = (S_i^-)^2 = 0. \quad (1.8)$$

These commutation relations are much more complicated than the simple (anti-) commutation relations of bosons and fermions,

$$\left[b_i, b_j^\dagger \right] = \delta_{ij}, \quad \left[b_i^\dagger, b_j^\dagger \right] = [b_i, b_j] = 0, \quad (1.9a)$$

$$\left\{ c_i, c_j^\dagger \right\} = \delta_{ij}, \quad \left\{ c_i^\dagger, c_j^\dagger \right\} = \{c_i, c_j\} = 0, \quad (1.9b)$$

where b_i^\dagger and b_i are bosonic creation and annihilation operators, c_i^\dagger and c_i are fermionic creation and annihilation operators, and $\{c_i, c_j^\dagger\} = c_i c_j^\dagger + c_j^\dagger c_i$ is the anticommutator. The advantage of bosonic and fermionic operators is that there exists Wick's theorem for such operators which relates averages of time ordered products of bosonic or fermionic operators to averages of pairs. Wick's theorem allows the use of Green function methods and Feynman diagrams [37, 38]. Therefore it is in many cases sensible to represent the spin operators in terms of bosonic or fermionic operators. While there are many different ways of representing spin operators in terms of bosonic or fermionic operators [39], we will only discuss the widely used Holstein-Primakoff transformation [40], the three spin-1/2 representations which we will use later on, and the mapping to Abrikosov pseudofermions.

1.2.1 Holstein-Primakoff transformation

The Holstein-Primakoff transformation maps the spin operators for arbitrary spin S to bosonic creation and annihilation operators [40],

$$S_i^z = S - \hat{n}_i, \quad \hat{n}_i = b_i^\dagger b_i, \quad (1.10\text{a})$$

$$S_i^+ = \sqrt{2S} \sqrt{1 - \frac{\hat{n}_i}{2S}} b_i, \quad (1.10\text{b})$$

$$S_i^- = \sqrt{2S} b_i^\dagger \sqrt{1 - \frac{\hat{n}_i}{2S}}. \quad (1.10\text{c})$$

While this transformation preserves the spin commutation relations (1.7), the Hilbert space of the bosons has to be restricted to $\hat{n}_i \leq 2S$ to prevent the occurrence of unphysical states. Since such a restriction is difficult to implement, this constraint is usually ignored. In a spin-wave calculation, we would then expand the operators to order $1/S$,

$$S_i^+ = \sqrt{2S} \left(b_i - \frac{\hat{n}_i b_i}{4S} + \dots \right), \quad (1.11\text{a})$$

$$S_i^- = \sqrt{2S} \left(b_i^\dagger - \frac{b_i^\dagger \hat{n}_i}{4S} + \dots \right). \quad (1.11\text{b})$$

We see that this procedure is well justified if the average occupation n_i per lattice is small compared to the spin S ($n_i \ll S$). This means that this method is restricted to low temperatures and can describe small fluctuation around an ordered spin configuration. The antiferromagnetically ordered phase in Cs_2CuCl_4 has been extensively studied within spin-wave theory [18, 27, 41–43]. Since we do not want to describe this antiferromagnetic phase or be restricted to the low-temperature regime, we will not use the Holstein-Primakoff transformation in this thesis. In the case of $S = 1/2$ and low dimensions, the condition $n_i \ll S$ is not necessarily fulfilled even at low temperatures, which has been discussed in Ref. [36] for the antiferromagnetic spin-1/2 Heisenberg model on a two-dimensional square lattice.

1.2.2 Jordan-Wigner transformation

A very powerful method for one-dimensional spin-1/2 chains with nearest-neighbor exchange couplings is the Jordan-Wigner transformation which maps the spin-1/2 operators to spinless fermions [44, 45],

$$S_i^+ = (S_i^-)^\dagger = c_i^\dagger e^{i\pi \sum_{j < i} c_j^\dagger c_j}, \quad S_i^z = c_i^\dagger c_i - 1/2. \quad (1.12)$$

The advantage of this transformation is that it is an exact one-to-one mapping which does not require any additional constraints on the Hilbert space of the fermions. The state without a fermion on a lattice site corresponds to the spin-down state and the state with a fermion to the spin-up state. Due to the Pauli

exclusion principle there can either be one or no fermion on a given lattice sites (the fermions are spinless). Therefore the dimension of the Hilbert space of the fermions is 2^N (where N is the number of spins), which is also the dimension of the original Hilbert space of N spins with spin 1/2. The disadvantage of this transformation is the phase factor $\exp(i\pi \sum_{j < i} c_j^\dagger c_j)$ which implements the correct spin commutation relations and is difficult to deal with. Fortunately, for a simple chain model with nearest-neighbor exchange couplings, these phase factors cancel exactly in the Hamiltonian. To illustrate this, we consider the XY model in one dimension which is given by

$$\mathcal{H}_{1D} = J \sum_i (S_i^x S_{i+1}^x + S_i^y S_{i+1}^y) - h \sum_i S_i^z. \quad (1.13)$$

By applying the Jordan-Wigner transformation, we obtain a Hamiltonian which is quadratic in the fermionic operators and can be easily diagonalized via a Fourier transform to momentum space,

$$\mathcal{H}_{1D} = \sum_k (J \cos k - h) c_k^\dagger c_k + \frac{Nh}{2}, \quad (1.14)$$

with

$$c_k = \frac{1}{\sqrt{N}} \sum_j e^{-ikj} c_j, \quad c_k^\dagger = \frac{1}{\sqrt{N}} \sum_j e^{ikj} c_j^\dagger. \quad (1.15)$$

We see that the phase factors $\exp(i\pi \sum_{j < i} c_j^\dagger c_j)$ do not occur in the transformed Hamiltonian for this simple model. Unfortunately, the phase factors do not cancel in higher-dimensional models or models with exchange couplings beyond nearest neighbors [44]. Therefore, the Jordan-Wigner transformation is best suited for one-dimensional chain models with nearest-neighbor exchange couplings.

1.2.3 Hard-core bosons

A mapping closely related to the Jordan-Wigner transformation is the mapping of the spin-1/2 operators to hard-core bosons [46, 47],

$$S_i^+ = b_i, \quad S_i^- = b_i^\dagger, \quad S_i^z = 1/2 - b_i^\dagger b_i, \quad (1.16)$$

where the hard-core boson operators satisfy the commutation relation

$$[b_i, b_j^\dagger] = \delta_{ij} (1 - 2b_i^\dagger b_i), \quad (1.17)$$

and the occupation number per site is restricted to $\hat{n}_i = 0$ or 1 , with $\hat{n}_i = b_i^\dagger b_i$. The state without a bosons on a lattice site corresponds to the spin-up state and the state with a boson to the spin-down state. The hard-core boson

constraint and the commutation relation (1.17) can be realized by treating the hard-core bosons as canonical bosons with an infinite on-site repulsion,

$$\mathcal{H}_U = \frac{U}{2} \sum_i b_i^\dagger b_i^\dagger b_i b_i, \text{ with } U \rightarrow \infty. \quad (1.18)$$

The advantage of this mapping is that it can be used for any kind of spin-1/2 model in any dimensions because the mapping (1.16) does not include any phase factors. The disadvantage is that we have to deal with the infinite on-site interaction which has to be treated non-perturbatively. It has been recently shown in Ref. [48] that the infinite on-site interaction can be treated within a self-consistent ladder approximation when the excited states are separated by an energy gap from the ground state. For our spin model (1.1), this is the case when the magnetic field is larger than the saturation field B_c .

1.2.4 Majorana fermions

We can map the spin-1/2 operators to Majorana fermions [49] by introducing for each lattice site \mathbf{R}_i three Majorana fermions η_i^x , η_i^y , and η_i^z satisfying the anticommutation relations

$$\left\{ \eta_i^\alpha, \eta_j^\beta \right\} = \delta_{ij} \delta^{\alpha\beta}. \quad (1.19)$$

The spin algebra can be reproduced by setting

$$S_i^x = -i\eta_i^y \eta_i^z, \quad S_i^y = -i\eta_i^z \eta_i^x, \quad S_i^z = -i\eta_i^x \eta_i^y. \quad (1.20)$$

Note that with our normalization $(\eta_i^\alpha)^2 = 1/2$. The above Majorana representation has been used previously by several authors to study quantum spin systems [50–56]. Moreover, a coherent state path integral for the Majorana fermions can be constructed [56] so that the usual field theoretical methods can be used to study the underlying spin model. An advantage of the above Majorana representation is that it does not introduce any unphysical states without needing any additional constraints. On the other hand, for a system consisting of an even number N of spins, the Majorana Hilbert space has $2^{3N/2}$ states and consists of $2^{N/2}$ identical copies of the 2^N -dimensional spin Hilbert space [55].

1.2.5 Abrikosov pseudofermions

Another possibility is to use Abrikosov pseudofermions [39, 57], where the spin-operator at lattice site \mathbf{R}_i is expressed in terms of a pair of canonical fermion operators $c_{i\uparrow}$ and $c_{i\downarrow}$ as

$$\mathbf{S}_i = (c_{i\uparrow}^\dagger, c_{i\downarrow}^\dagger) \frac{\boldsymbol{\sigma}}{2} \begin{pmatrix} c_{i\uparrow} \\ c_{i\downarrow} \end{pmatrix}. \quad (1.21)$$

Here, the components of the vector σ are the usual Pauli matrices. One disadvantage of the representation (1.21) is that the fermionic Hilbert space contains two unphysical states per lattice site, corresponding to empty and doubly occupied sites. In order to describe the physical spin system, these unphysical states must be projected out. According to Popov and Fedotov [58], this can be done by formally imposing on the system a fictitious imaginary chemical potential $\mu_f = i\pi T/2$. In frequency space, this is equivalent to replacing the fermionic Matsubara frequencies $2\pi T(n+1/2)$ by semionic ones, $2\pi T(n+1/4)$. If no further approximations are made, the semionic Matsubara frequencies automatically eliminate the unphysical states from the fermionic Hilbert space. Recently, this procedure has been used to study the triangular lattice anti-ferromagnet by means of a diagrammatic Monte Carlo method [59, 60]. To avoid the complications associated with an imaginary chemical potential, it is sometimes sufficient to implement the projection only on average, which formally amounts to setting $\mu_f = 0$. Unfortunately, at finite temperature this approximation can introduce uncontrollable errors [61].

1.3 Hartree-Fock and mean-field approximations

Hartree-Fock and mean-field approximations are variational methods where the original Hamiltonian \mathcal{H} is replaced by an exactly solvable approximate Hamiltonian \mathcal{H}_{MF} with variational parameters. The variational procedure is based on the Bogoliubov inequality for the free energy [62],

$$F \leq F_{\text{MF}} + \langle \mathcal{H} - \mathcal{H}_{\text{MF}} \rangle_{\text{MF}}, \quad (1.22)$$

where F is the exact free energy of the original Hamiltonian \mathcal{H} , F_{MF} is the free energy of the approximate Hamiltonian \mathcal{H}_{MF} , and $\langle \dots \rangle_{\text{MF}}$ denotes the expectation value with respect to \mathcal{H}_{MF} , which can be exactly calculated. The variational parameters of \mathcal{H}_{MF} can then be obtained by minimizing the right hand side of Eq. (1.22), leading to self-consistency equations for the variational parameters. In the mean-field calculations in this thesis, we use an equivalent method [62] where we start not by minimizing Eq. (1.22), but instead we replace the interaction terms in the original Hamiltonian by quartic terms where parts of the interactions term have been replaced by their expectation values. We then demand that the expectation values have to be calculated self-consistently. For example, we can approximate the following bosonic interaction (with $i \neq j$),

$$\begin{aligned} b_i^\dagger b_i b_j^\dagger b_j &\approx n_i b_j^\dagger b_j + n_j b_i^\dagger b_i - n_i n_j \\ &+ \tau_{ji} b_i^\dagger b_j + \tau_{ij} b_j^\dagger b_i - \tau_{ij} \tau_{ji}, \end{aligned} \quad (1.23)$$

where the variational parameters n_i and τ_{ij} have to fulfill the self-consistency equations

$$n_i = \langle b_i^\dagger b_i \rangle, \quad \tau_{ij} = \langle b_i^\dagger b_j \rangle. \quad (1.24)$$

The Hartree-Fock decoupling in Eq. (1.23) is based on a partial Wick contraction where the constant terms $n_i n_j$ and $\tau_{ij} \tau_{ji}$ have to be subtracted to get the correct expectation value $\langle b_i^\dagger b_i b_j^\dagger b_j \rangle \approx n_i n_j + \tau_{ij} \tau_{ji}$ within the Hartree-Fock approximation. For fermions, the analogous Hartree-Fock decoupling is (with $i \neq j$)

$$\begin{aligned} c_i^\dagger c_i c_j^\dagger c_j &\approx n_i c_j^\dagger c_j + n_j c_i^\dagger c_i - n_i n_j \\ &- \tau_{ji} c_i^\dagger c_j - \tau_{ij} c_j^\dagger c_i + \tau_{ij} \tau_{ji}, \end{aligned} \quad (1.25)$$

where the different signs in the second line are due to the anticommutation relations of the fermions, and the self-consistency equations are given by

$$n_i = \langle c_i^\dagger c_i \rangle, \quad \tau_{ij} = \langle c_i^\dagger c_j \rangle. \quad (1.26)$$

1.4 Diagrammatic methods

When we map the spin operators to bosonic or fermionic operators, we can use Wick's theorem and the coherent state path integral formalism from which we can derive an expansion of the self-energy in terms of Feynman diagrams [37]. Below we summarize some important results but we refer to the textbook [37] for more details and derivations.

1.4.1 Path integral formalism and Wick's theorem

We consider now a Hamiltonian of the following form describing interacting bosons or fermions on a lattice,

$$\mathcal{H} = \sum_{\mathbf{k}} \xi_{\mathbf{k}} b_{\mathbf{k}}^\dagger b_{\mathbf{k}} + \frac{1}{2N} \sum_{\mathbf{k}, \mathbf{k}', \mathbf{q}} V_{\mathbf{q}} b_{\mathbf{k}+\mathbf{q}}^\dagger b_{\mathbf{k}'-\mathbf{q}}^\dagger b_{\mathbf{k}'} b_{\mathbf{k}}, \quad (1.27)$$

where the creation and annihilation operators $b_{\mathbf{k}}^\dagger$ and $b_{\mathbf{k}}$ can be either bosonic or fermionic and the momentum index \mathbf{k} has N different possible values. We assume that the interaction has inversion symmetry, $V_{\mathbf{q}} = V_{-\mathbf{q}}$, and only depends on the momentum transfer \mathbf{q} . We can write the partition function in the path integral formalism as

$$\mathcal{Z} = \text{Tr } e^{-\beta \mathcal{H}} = \int \mathcal{D} [\bar{b}, b] e^{-S[\bar{b}, b]}, \quad (1.28)$$

where b is now a complex field for bosons and a Grassmann field for fermions, \bar{b} is the complex conjugate field to b or an independent Grassmann field for

fermions, and $\beta = 1/T$ is the inverse temperature.¹ The action $S[\bar{b}, b]$ is given in Matsubara frequency space by

$$S[\bar{b}, b] = - \int_K G_0^{-1}(K) \bar{b}_K b_K + \frac{1}{2} \int_{K, K', Q} V_{\mathbf{q}} \bar{b}_{K+Q} \bar{b}_{K'-Q} b_{K'} b_K, \quad (1.29)$$

where we have introduced the composite index $K = (\mathbf{k}, i\omega_k)$ with the corresponding sum

$$\int_K = \frac{1}{\beta N} \sum_{\mathbf{k}} \sum_{\omega_k}, \quad (1.30)$$

and the bare Green function is given by

$$G_0(K) = \frac{1}{i\omega_k - \xi_{\mathbf{k}}}. \quad (1.31)$$

The Matsubara frequencies ω_k are defined by

$$\omega_k = \begin{cases} \frac{2\pi k}{\beta} & , \text{ bosons}, \\ \frac{2\pi(k+\frac{1}{2})}{\beta} & , \text{ fermions}, \end{cases} \quad (1.32)$$

with $k \in \mathbb{Z}$. The integral measure is

$$\int \mathcal{D} [\bar{b}, b] = \prod_{\mathbf{k}} \prod_{\omega_k} \frac{d\bar{b}_K db_K}{\tilde{\mathcal{N}}}, \quad (1.33)$$

where $\tilde{\mathcal{N}}$ is a normalization constant which is not important for the calculation of correlation functions. The fields in imaginary time and in Matsubara frequency space are related by

$$b_{\mathbf{k}}(\tau) = \frac{1}{\beta\sqrt{N}} \sum_{\omega_k} e^{-i\omega_k\tau} b_K, \quad (1.34a)$$

$$\bar{b}_{\mathbf{k}}(\tau) = \frac{1}{\beta\sqrt{N}} \sum_{\omega_k} e^{i\omega_k\tau} \bar{b}_K. \quad (1.34b)$$

We note that expectation values of products of fields in imaginary time correspond to expectation values of time-ordered products of operators in imaginary time [37]. We can now state Wick's theorem in the functional integral formulation,

$$\begin{aligned} & \frac{\int \mathcal{D} [\bar{b}, b] b_{K_1} \dots b_{K_n} \bar{b}_{Q_n} \dots \bar{b}_{Q_1} e^{-\int_K \bar{b}_K M_{K,Q} b_Q}}{\int \mathcal{D} [\bar{b}, b] e^{-\int_K \bar{b}_K M_{K,Q} b_Q}} \\ &= (\beta N)^n \sum_P \zeta^P M_{K_{P_n} Q_n}^{-1} \dots M_{K_{P_1} Q_1}^{-1}, \end{aligned} \quad (1.35)$$

¹Throughout this thesis we use natural units, i.e. $k_B = 1$ and $\hbar = 1$, unless indicated otherwise. This means that temperatures and frequencies are measured in units of energy.

where \sum_P is the sum over all permutations P and $\zeta = 1$ for bosons and $\zeta = -1$ for fermions. Wick's theorem enables us to calculate expectation values with respect to a quadratic action where the result consists of products of the bare Green function. When the action is not quadratic, we can expand the exponential of the non-quadratic part, leaving us again with a quadratic action. Therefore we can perform a perturbative expansion in terms of the interaction strength which can be represented by Feynman diagrams [37, 38].

1.4.2 One-particle Green function and self-energy

The one-particle Green function $G(K)$ and the corresponding irreducible self-energy $\Sigma(K)$ are defined via the functional average

$$\langle b_K \bar{b}_K \rangle = -\beta N G(K) = -\beta N \frac{1}{G_0^{-1}(K) - \Sigma(K)}, \quad (1.36)$$

where

$$\langle \dots \rangle = \frac{\int \mathcal{D} [\bar{b}, b] \dots e^{-S[\bar{b}, b]}}{\int \mathcal{D} [\bar{b}, b] e^{-S[\bar{b}, b]}}. \quad (1.37)$$

In the non-interacting case with $V_{\mathbf{q}} = 0$, we recover via Wick's theorem (1.35) the bare Green function,

$$\langle b_K \bar{b}_K \rangle_0 = -\beta N G_0(K) = -\beta N \frac{1}{i\omega_k - \xi_{\mathbf{k}}}. \quad (1.38)$$

If we perform a perturbative expansion of the Green function $G(K)$ in terms of the interaction vertices $V_{\mathbf{q}}$ and the bare propagators $G_0(K)$, then the self-energy consists, in terms of Feynman diagrams, of all the diagrams (without external propagators $[G_0(K)]^2$) which cannot be separated into two diagrams by cutting a single propagator line; these diagrams are called irreducible. This can be seen by expanding Eq. (1.36),

$$\begin{aligned} G(K) &= G_0(K) + G_0(K)\Sigma(K)G_0(K) \\ &+ G_0(K)\Sigma(K)G_0(K)\Sigma(K)G_0(K) + \dots, \end{aligned} \quad (1.39)$$

where the second term is given by all irreducible diagrams with external propagators $[G_0(K)]^2$ and the third term is given by all irreducible diagrams which can be separated at only one point into two parts, and so on. Summing this infinite series recovers all contribution to the Green function $G(K)$ which confirms the identification of the self-energy with the irreducible diagrams without external propagators.

1.4.3 Feynman diagram representation of the self-energy

We now summarize the rules for obtaining the perturbative expansion of the self-energy in terms of Feynman diagrams. We restrict us here to the bosonic

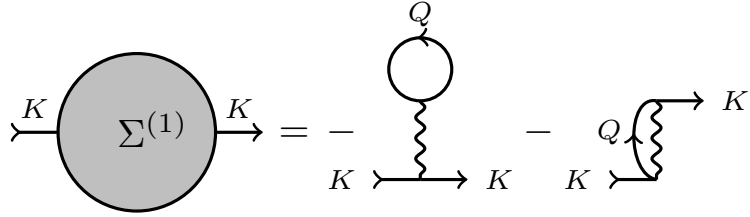


Figure 1.3: First order contributions to the self-energy $\Sigma(K)$.

case since in this thesis we are not going to use Feynman diagram methods for fermions. First, we define the basic building blocks of our Feynman diagrams. A directed line with index K corresponds to the bare Green function $G_0(K)$ and a vertex, represented by a wiggly line with an ingoing and an outgoing line at each end, corresponds to an interaction V_q , where q is the momentum transfer at the vertex. If we are now given a Feynman diagram, we can translate the diagram to an algebraic expression by using these definitions for lines and vertices, multiplying each, and finally summing over all free indices (using the sum defined in Eq. (1.30)). A free index is an index K which is not fixed by external indices or momentum and frequency conservation. The n th order contribution to the self-energy $\Sigma(K)$ is then obtained by drawing all (topologically different) connected diagrams with two external legs K containing n vertices and $2n - 1$ connected lines and finally multiplying by an overall factor $(-1)^n$. As an example, we show in Fig. 1.3 the first order contributions to the self-energy $\Sigma(K)$. Translating these diagrams into algebraic expressions, we obtain

$$\Sigma^{(1)}(K) = - \int_Q V_0 G_0(Q) e^{i\omega_q 0^+} - \int_Q V_{q-k} G_0(Q) e^{i\omega_q 0^+}. \quad (1.40)$$

We note that whenever a propagator line $G_0(Q)$ starts and ends at the same vertex, a convergence factor $e^{i\omega_q 0^+}$ has to be included [37]. The origin of this convergence factor is the time ordering at the interaction vertex, which we explain in Sec. 1.4.5.

1.4.4 Calculation of Matsubara sums

When working in Matsubara frequency space, we encounter Matsubara sums of the following type,

$$R = \frac{1}{\beta} \sum_{\omega_n} g(i\omega_n), \quad (1.41)$$

where the sum is over Matsubara frequencies

$$\omega_n = \begin{cases} \frac{2\pi n}{\beta}, & \text{bosons,} \\ \frac{2\pi(n+\frac{1}{2})}{\beta}, & \text{fermions,} \\ \frac{2\pi(n+\frac{1}{4})}{\beta}, & \text{semions,} \end{cases} \quad (1.42)$$

with $n \in \mathbb{Z}$. The semionic frequencies occur when the Popov-Fedotov method for the Abrikosov pseudofermion representation of the spin-1/2 operators is used (see Sec. 1.2.5). Although the evaluation of the Matsubara sum R is a standard textbook calculation [63], we go through the essential steps and generalize the textbook result to the semionic case. We first introduce the complex auxiliary function $n(z)$ with simple poles at $z = i\omega_n$,

$$n(z) = \frac{1}{e^{\beta z} - \zeta}, \quad (1.43)$$

where

$$\zeta = \begin{cases} 1, & \text{bosons,} \\ -1, & \text{fermions,} \\ i, & \text{semions.} \end{cases} \quad (1.44)$$

Using the residue theorem, we find

$$\zeta \int_{\mathcal{C}} \frac{dz}{2\pi i} g(z) n(z) = \zeta \sum_{\omega_n} \text{Res}[n(z)] g(z)|_{z=i\omega_n} = \frac{1}{\beta} \sum_{\omega_n} g(i\omega_n), \quad (1.45)$$

where the integration path \mathcal{C} is shown in Fig. 1.4(a) and we have used

$$\text{Res } n(z)|_{z=i\omega_n} = \frac{1}{\zeta \beta}. \quad (1.46)$$

If we now blow up the integration path without crossing any poles of $g(z)$, we see that the integral is determined by the poles z_p of $g(z)$, as shown in Fig. 1.4(b), assuming that $g(z)n(z)$ vanishes faster than $1/|z|$ for $|z| \rightarrow \infty$,

$$\zeta \int_{\mathcal{C}} \frac{dz}{2\pi i} g(z) n(z) = -\zeta \sum_{z_p} \text{Res}[g(z)] \left. \frac{1}{e^{\beta z} - \zeta} \right|_{z=z_p}. \quad (1.47)$$

Therefore, we can evaluate the Matsubara sum R by considering the poles z_p of $g(z)$,

$$R = \frac{1}{\beta} \sum_{\omega_n} g(i\omega_n) = -\zeta \sum_{z_p} \text{Res}[g(z)] \left. \frac{1}{e^{\beta z} - \zeta} \right|_{z=z_p}. \quad (1.48)$$

As a simple example, we consider the case

$$g(i\omega) = \frac{e^{i\omega 0^+}}{i\omega - \xi}, \quad (1.49)$$

where we find

$$R = \frac{1}{\beta} \sum_{\omega_n} \frac{e^{i\omega_n 0^+}}{i\omega_n - \xi} = -\zeta \frac{1}{e^{\beta \xi} - \zeta}. \quad (1.50)$$

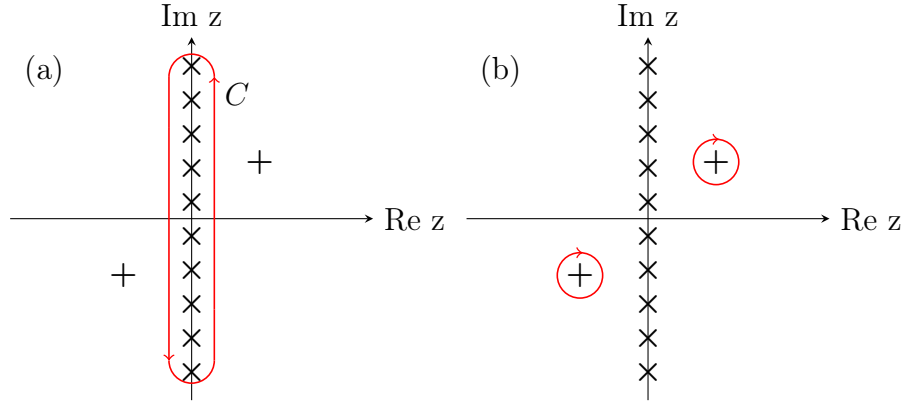


Figure 1.4: (a) Integration path C for the Matsubara summation in Eq. (1.45), where \times indicates the Matsubara frequencies $i\omega_n$ and $+$ the poles z_p of $g(z)$. (b) Deformed integration path where only the poles of $g(z)$ contribute.

1.4.5 Origin of the convergence factor

In Sec. 1.4.3 we have noted that whenever a propagator line $G_0(K)$ starts and ends at the same vertex, a convergence factor $e^{i\omega_k 0^+}$ has to be included. To explain the origin of this convergence factor, we have to consider the exact discrete imaginary time formulation of the path integral, where the partition function for bosons ($\zeta = 1$) or fermions ($\zeta = -1$) is [37]

$$\mathcal{Z} = \lim_{L \rightarrow \infty} \int \prod_{l=1}^L \prod_{\mathbf{k}} \frac{1}{\mathcal{N}} d\bar{b}_{\mathbf{k},l} db_{\mathbf{k},l} e^{-S[\bar{b},b]}, \quad (1.51)$$

where

$$\mathcal{N} = \begin{cases} 2\pi i, & \text{bosons,} \\ 1, & \text{fermions,} \end{cases} \quad (1.52)$$

and the action is given by

$$S[\bar{b}, b] = \epsilon \sum_{l=1}^L \sum_{\mathbf{k}} \bar{b}_{\mathbf{k},l} \left(\frac{b_{\mathbf{k},l} - b_{\mathbf{k},l-1}}{\epsilon} \right) + \epsilon \sum_{l=1}^L \mathcal{H} [\bar{b}_{\mathbf{k},l}, b_{\mathbf{k},l-1}], \quad (1.53)$$

with $\epsilon = \beta/L$. The term $\mathcal{H} [\bar{b}_{\mathbf{k},l}, b_{\mathbf{k},l-1}]$ is just the Hamiltonian \mathcal{H} where the creation and annihilation operators have been replaced by the corresponding fields. The crucial point is that the fields $\bar{b}_{\mathbf{k},l}$ in $\mathcal{H} [\bar{b}_{\mathbf{k},l}, b_{\mathbf{k},l-1}]$ are given at an infinitesimally later time $\tau_l = \epsilon l$ than the fields $b_{\mathbf{k},l-1}$ given at $\tau_{l-1} = \epsilon(l-1)$,

$$\tau_l - \tau_{l-1} = \epsilon l - \epsilon(l-1) = \epsilon. \quad (1.54)$$

If we now have the case that a propagator starts and ends at the same interaction vertex

$$\bar{b}_{\mathbf{k}+\mathbf{q},l} \bar{b}_{\mathbf{k}'-\mathbf{q},l} b_{\mathbf{k}',l-1} b_{\mathbf{k},l-1}, \quad (1.55)$$

then this propagator is given by the expectation value

$$-\langle b_{\mathbf{k},l-1} \bar{b}_{\mathbf{k},l} \rangle_0 = G_0(\mathbf{k}, \tau_{l-1} - \tau_l) = G_0(\mathbf{k}, -\epsilon). \quad (1.56)$$

This infinitesimal time $-\epsilon$ is important due to the discontinuity of the propagator at $\tau = 0$ [37],

$$G_0(\mathbf{k}, \tau) = \begin{cases} -[1 + \zeta n_\zeta(\xi_{\mathbf{k}})] e^{-\xi_{\mathbf{k}} \tau}, & \tau \geq 0, \\ -\zeta n_\zeta(\xi_{\mathbf{k}}) e^{-\xi_{\mathbf{k}} \tau}, & \tau < 0. \end{cases} \quad (1.57)$$

Transforming to Matsubara frequencies, we find

$$G_0(\mathbf{k}, -\epsilon) = \frac{1}{\beta} \sum_{\omega_k} e^{i\omega_k \epsilon} G_0(K), \quad (1.58)$$

where we see that the convergence factor $e^{i\omega_k \epsilon} = e^{i\omega_k 0^+}$ has to be included whenever a propagator $G_0(K)$ starts and ends at the same vertex.

1.4.6 Convergence of the partition function

In the simple case of non-interacting bosons or fermions, we also need a convergence factor $e^{i\omega_k 0^+}$ when calculating the partition function using Matsubara frequencies instead of the discrete imaginary time formalism. We consider now non-interacting bosons or fermions with dispersion $\xi_{\mathbf{k}}$ where \mathbf{k} is an index with N possible values. The Hamiltonian is then simply

$$\mathcal{H}_0 = \sum_{\mathbf{k}} \xi_{\mathbf{k}} b_{\mathbf{k}}^\dagger b_{\mathbf{k}}, \quad (1.59)$$

and the partition function is given by

$$\mathcal{Z}_0 = \int \mathcal{D}[\bar{b}, b] e^{-S_0[\bar{b}, b]}, \quad (1.60)$$

with the action

$$S_0[\bar{b}, b] = - \int_K (i\omega_k - \xi_{\mathbf{k}}) \bar{b}_K b_K. \quad (1.61)$$

The integral measure is given by

$$\int \mathcal{D}[\bar{b}, b] = \int \prod_{\omega_k} \prod_{\mathbf{k}} \frac{1}{N} \left(\frac{1}{\beta N \epsilon} \right)^\zeta d\bar{b}_K db_K, \quad (1.62)$$

which follows from the Fourier transform to Matsubara frequencies of the integral measure in Eq. (1.51).² Performing the Gaussian integral, we get

$$\mathcal{Z}_0 = \prod_{\mathbf{k}} \prod_{\omega_k} [-\epsilon(i\omega_k - \xi_{\mathbf{k}})]^{-\zeta}, \quad (1.63)$$

$$F_0 = -\frac{1}{\beta} \ln \mathcal{Z}_0 = \frac{\zeta}{\beta} \sum_{\mathbf{k}} \sum_{\omega_k} \ln [-\epsilon(i\omega_k - \xi_{\mathbf{k}})], \quad (1.64)$$

where we note that the free energy F_0 and therefore the partition function \mathcal{Z}_0 do not converge. This can be fixed by introducing a convergence factor $e^{i\omega_k 0^+}$ [64],

$$F_0 = \frac{\zeta}{\beta} \sum_{\mathbf{k}} \sum_{\omega_k} e^{i\omega_k 0^+} \ln [-\epsilon(i\omega_k - \xi_{\mathbf{k}})], \quad (1.65)$$

which leads to the correct result

$$F_0 = \frac{\zeta}{\beta} \sum_{\mathbf{k}} \ln (1 - \zeta e^{-\beta \xi_{\mathbf{k}}}). \quad (1.66)$$

However, the justification of this convergence factor is not made entirely clear in the literature [64] because the usual arguments would only lead to a convergence factor for the Green function inside the logarithm. Therefore, we give here a simple and convincing argument for the convergence factor outside the logarithm. First, we consider the expectation value $\langle b_{\mathbf{k}}^\dagger b_{\mathbf{k}} \rangle$ which can be expressed in terms of the Green function,

$$\langle b_{\mathbf{k}}^\dagger b_{\mathbf{k}} \rangle = \langle \bar{b}_{\mathbf{k}}(\tau) b_{\mathbf{k}}(\tau - 0^+) \rangle = -\zeta G_0(\mathbf{k}, \tau = -0^+). \quad (1.67)$$

Using the Fourier transform

$$G_0(\mathbf{k}, \tau) = \frac{1}{\beta} \sum_{\omega_k} e^{-i\omega_k \tau} G_0(K), \quad (1.68)$$

we find

$$\langle b_{\mathbf{k}}^\dagger b_{\mathbf{k}} \rangle = -\frac{\zeta}{\beta} \sum_{\omega_k} e^{i\omega_k 0^+} G_0(K). \quad (1.69)$$

Now, the same expectation value can also be calculated by differentiating F_0 given by Eq. (1.65),

$$\begin{aligned} \langle b_{\mathbf{k}}^\dagger b_{\mathbf{k}} \rangle &= \frac{\partial}{\partial \xi_{\mathbf{k}}} F_0 = \frac{\partial}{\partial \xi_{\mathbf{k}}} \frac{\zeta}{\beta} \sum_{\mathbf{k}'} \sum_{\omega_k} e^{i\omega_k 0^+} \ln [-\epsilon(i\omega_k - \xi_{\mathbf{k}'})] \\ &= -\frac{\zeta}{\beta} \sum_{\omega_k} e^{i\omega_k 0^+} G_0(K), \end{aligned} \quad (1.70)$$

²This can be derived by calculating $\sum_l \bar{b}_{\mathbf{k},l} b_{\mathbf{k},l} = \frac{L}{N\beta^2} \sum_{\omega_k} \bar{b}_K b_K$, from which we see that the Fourier transform is a unitary transformation times $\sqrt{\frac{L}{N\beta^2}}$, giving the term $(\frac{L}{N\beta^2})^\zeta$. We note that although this term has no obvious continuum limit ($L \rightarrow \infty$), the quantity L cancels out in the calculation of the partition function [64].

where we see that the convergence factor outside the logarithm is necessary to be consistent with Eq. (1.69).

While we have shown here that the partition function of non-interacting bosons or fermions can be calculated with Matsubara sums, it is easier to calculate the partition function \mathcal{Z}_0 directly or within the discrete imaginary time formalism. Fortunately, the subtleties related to the integral measure and the convergence of \mathcal{Z}_0 are not relevant for calculations of $\mathcal{Z}/\mathcal{Z}_0$ and Green functions where the in the continuum limit ill-defined terms cancel out.

Chapter 2

Majorana spin-liquid and dimensional reduction

2.1 Introduction

In this chapter, we shall focus on the finite-temperature spin-liquid phase of Cs_2CuCl_4 in the regime where the external magnetic field is not too close to the critical field $B_c \approx 8.5$ T. Because in this part of the phase diagram the temperature is large compared with the inter-plane interaction J'' and the Dzyaloshinskii-Moriya interaction D , these interactions can be neglected for our purpose. It is therefore reasonable to describe the spin-liquid phase of Cs_2CuCl_4 within a purely two-dimensional triangular lattice antiferromagnetic Heisenberg model,

$$\mathcal{H} = \frac{1}{2} \sum_{ij} J_{ij} \mathbf{S}_i \cdot \mathbf{S}_j - h \sum_i S_i^z, \quad (2.1)$$

where the spin $S = 1/2$ operators $\mathbf{S}_i = \mathbf{S}_{\mathbf{R}_i}$ are localized on the sites \mathbf{R}_i of a distorted triangular lattice and the exchange couplings $J_{ij} = J(\mathbf{R}_i - \mathbf{R}_j)$ are only finite if $\mathbf{R}_i - \mathbf{R}_j$ connect nearest-neighbor sites on the lattice. At this point, we assume different exchange couplings $J_\mu = J(\pm \boldsymbol{\delta}_\mu)$ in each of the three directions $\boldsymbol{\delta}_1$, $\boldsymbol{\delta}_2$ and $\boldsymbol{\delta}_3$ shown in Fig. 2.1, where $\mu = 1, 2, 3$ labels the directions. Later, we shall set $J_1 = J = 4.34$ K and $J_2 = J_3 = J' = 1.49$ K to describe Cs_2CuCl_4 .

Given the fact that in Cs_2CuCl_4 the ratio $J'/J \approx 1/3$ is not really small, it is at first sight reasonable to expect that the nature of the spin-liquid phase is such that the elementary excitations of the spin liquid can propagate coherently in all directions on the two-dimensional lattice. However, a theory where the elementary excitations of the spin liquid resemble the one-dimensional fermionic spinon excitations of a Heisenberg chain has been highly successful [6, 7, 65], suggesting that the spin-liquid phase in Cs_2CuCl_4 supports elementary excitations which can only propagate coherently along the direction $\boldsymbol{\delta}_1$ of the strongest bond. In a simple picture, this dimensional reduction in Cs_2CuCl_4 arises from a strong frustration-induced reduction of the effective coupling J'

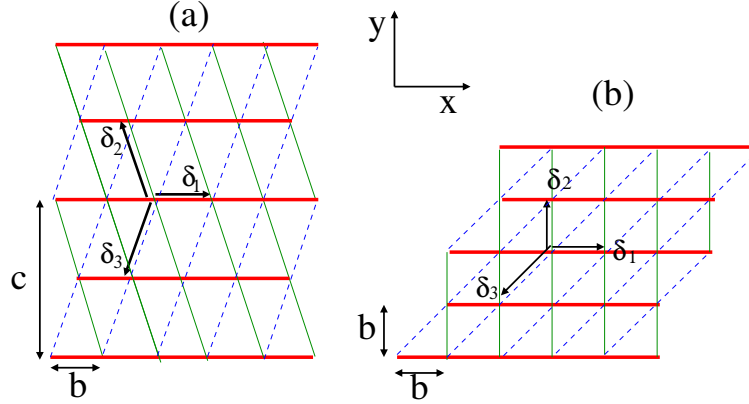


Figure 2.1: (a) Anisotropic triangular lattice with nearest-neighbor exchange coupling J_1 (thick lines), J_2 (thin lines) and J_3 (thin dashed lines); the corresponding link vectors are $\delta_1 = b\hat{x}$, $\delta_2 = -\frac{b}{2}\hat{x} + \frac{c}{2}\hat{y}$ and $\delta_3 = -\frac{b}{2}\hat{x} - \frac{c}{2}\hat{y}$. To describe Cs_2CuCl_4 , we should set $J_1 = J = 4.34$ K and $J_2 = J_3 = J' = 1.49$ K; the lattice structure is orthorhombic with in-plane lattice parameters $b = 7.48$ Å and $c = 12.26$ Å; the crystallographic a axis is perpendicular to the plane of the paper. (b) Topologically equivalent square lattice with diagonal bonds.

associated with the weaker bonds [9]. However, a quantitative microscopic conformation of this scenario using many-body methods is rather involved. In this work, we shall show that a straightforward mean-field theory based on the well-known representation of the spin operators in terms of Majorana fermions [49] naturally explains the dimensional reduction in Cs_2CuCl_4 . Specifically, we find that an anisotropic spin-liquid state where the fractionalized fermionic excitations can only propagate coherently along the direction of the strongest bond minimizes the free energy already at the mean-field level.

If the external magnetic field has a component parallel to the layers, the phase diagram of quasi-two dimensional frustrated antiferromagnets is more complex, as discussed in a series of recent theoretical works by Starykh and co-authors [20–22]. Here we consider only the case where the magnetic field points along the crystallographic a axis.

The results presented in this chapter have been published in [P2].

2.2 Rotationally invariant Majorana mean-field theory

A recent NMR study [11] of Cs_2CuCl_4 found evidence that the spin-liquid phase in this material exhibits gapless fermionic excitations. To describe this phase theoretically, one should therefore express the spin operators of the underlying Heisenberg model in terms of fermionic degrees of freedom. Here, we shall use the fermionic representation based on Majorana fermions [49], as described in

Sec. 1.2.4; introducing for each lattice site \mathbf{R}_i three Majorana fermions η_i^x , η_i^y , and η_i^z , the spin algebra can be reproduced by setting

$$S_i^x = -i\eta_i^y\eta_i^z, \quad S_i^y = -i\eta_i^z\eta_i^x, \quad S_i^z = -i\eta_i^x\eta_i^y. \quad (2.2)$$

For our mean-field calculation we simply ignore the redundancy introduced by the mapping to Majorana fermions (see Sec. 1.2.4 and Ref. [55]).

In this section, we focus on the case of the vanishing external magnetic field, so that our Hamiltonian has spin-rotational invariance. To describe a spin-liquid state, we require that our mean-field decoupling neither breaks spin-rotational nor lattice-translational invariance. For the isotropic triangular lattice antiferromagnet such a Majorana mean-field theory has recently been developed by Biswas *et al.* [55]. Following this work, we introduce the Majorana bond operators

$$C_{ij}^\alpha = \eta_i^\alpha\eta_j^\alpha, \quad (2.3)$$

and use the operator identity

$$\mathbf{S}_i \cdot \mathbf{S}_j = \frac{1}{2} \sum_{\alpha \neq \beta} \eta_i^\alpha \eta_j^\alpha \eta_i^\beta \eta_j^\beta = \frac{1}{2} \sum_{\alpha \neq \beta} C_{ij}^\alpha C_{ij}^\beta \quad (2.4)$$

to write the Heisenberg Hamiltonian (2.1) for vanishing magnetic field as

$$\mathcal{H} = \frac{1}{4} \sum_{ij} \sum_{\alpha \neq \beta} J_{ij} C_{ij}^\alpha C_{ij}^\beta. \quad (2.5)$$

Performing now a simple mean-field decoupling,

$$C_{ij}^\alpha C_{ij}^\beta \rightarrow C_{ij}^\alpha \langle C_{ij}^\beta \rangle + \langle C_{ij}^\alpha \rangle C_{ij}^\beta - \langle C_{ij}^\alpha \rangle \langle C_{ij}^\beta \rangle, \quad (2.6)$$

and assuming spin-rotational invariance so that the expectation values

$$\langle C_{ij}^\alpha \rangle = \langle \eta_i^\alpha \eta_j^\alpha \rangle \equiv iZ_{ij} \quad (2.7)$$

are independent of the flavor index α , we obtain the mean-field Hamiltonian

$$\mathcal{H}_{\text{MF}} = i \sum_{ij\alpha} t_{ij} \eta_i^\alpha \eta_j^\alpha + U_0, \quad (2.8)$$

with hopping energies

$$t_{ij} = J_{ij} Z_{ij} = -t_{ji}, \quad (2.9)$$

and the interaction energy

$$U_0 = \frac{3}{2} \sum_{ij} J_{ij} Z_{ij}^2. \quad (2.10)$$

Note that by definition $Z_{ij} = -Z_{ji}$. Assuming that the mean-field state is translationally invariant, we may set

$$Z_{\mathbf{R}_i, \mathbf{R}_i \pm \delta_\mu} = \pm Z_\mu. \quad (2.11)$$

It is then useful to introduce the lattice Fourier transform of the Majorana fermions,

$$\eta_{\mathbf{R}_i}^{\alpha} = \frac{1}{\sqrt{N}} \sum_{\mathbf{k}} e^{i\mathbf{k}\cdot\mathbf{R}_i} \eta_{\mathbf{k}}^{\alpha}, \quad (2.12)$$

where the \mathbf{k} sum is over a full unit cell in the reciprocal space of the underlying Bravais lattice. Our mean-field Hamiltonian (2.8) can then be written as

$$\mathcal{H}_{\text{MF}} = \frac{1}{2} \sum_{\mathbf{k}, \alpha} \varepsilon_{\mathbf{k}} \eta_{-\mathbf{k}}^{\alpha} \eta_{\mathbf{k}}^{\alpha} + U_0, \quad (2.13)$$

with mean-field energy dispersion

$$\varepsilon_{\mathbf{k}} = -4 \sum_{\mu=1}^3 J_{\mu} Z_{\mu} \sin(\mathbf{k} \cdot \boldsymbol{\delta}_{\mu}), \quad (2.14)$$

and interaction energy

$$U_0 = 3N \sum_{\mu=1}^3 J_{\mu} Z_{\mu}^2. \quad (2.15)$$

Using the anticommutation relation

$$\{\eta_{\mathbf{k}}^{\alpha}, \eta_{\mathbf{k}'}^{\alpha}\} = \delta_{\mathbf{k}, -\mathbf{k}'} \quad (2.16)$$

together with the symmetry

$$\varepsilon_{-\mathbf{k}} = -\varepsilon_{\mathbf{k}}, \quad (2.17)$$

we can write the mean-field Hamiltonian (2.13) as

$$\mathcal{H}_{\text{MF}} = \sum_{\mathbf{k}, \varepsilon_{\mathbf{k}} > 0} \sum_{\alpha} \left(\varepsilon_{\mathbf{k}} \eta_{-\mathbf{k}}^{\alpha} \eta_{\mathbf{k}}^{\alpha} - \frac{1}{2} \varepsilon_{\mathbf{k}} \right) + U_0. \quad (2.18)$$

We now define the complex conjugated operators

$$(\eta_{\mathbf{k}}^{\alpha})^{\dagger} \equiv \eta_{-\mathbf{k}}^{\alpha}, \text{ for } \varepsilon_{\mathbf{k}} > 0. \quad (2.19)$$

Due to the symmetry (2.17), this identification uniquely defines for all pairs $\eta_{\mathbf{k}}^{\alpha}$ and $\eta_{-\mathbf{k}}^{\alpha}$ one conjugated operator $(\eta_{\mathbf{k}}^{\alpha})^{\dagger}$ and one non-conjugated operator $\eta_{\mathbf{k}}^{\alpha}$ with the usual anticommutation relation of complex fermions,

$$\left\{ \eta_{\mathbf{k}}^{\alpha}, (\eta_{\mathbf{k}'}^{\alpha})^{\dagger} \right\} = \delta_{\mathbf{k}, \mathbf{k}'}. \quad (2.20)$$

Therefore, we get a Hamiltonian of complex fermions,

$$\mathcal{H}_{\text{MF}} = \sum_{\mathbf{k}, \varepsilon_{\mathbf{k}} > 0} \sum_{\alpha} \left[\varepsilon_{\mathbf{k}} (\eta_{\mathbf{k}}^{\alpha})^{\dagger} \eta_{\mathbf{k}}^{\alpha} - \frac{1}{2} \varepsilon_{\mathbf{k}} \right] + U_0. \quad (2.21)$$

At finite temperature, the mean-field free energy $F = -\frac{1}{\beta} \ln \mathcal{Z}$ is then straightforward to calculate,

$$\begin{aligned} F &= -\frac{3}{\beta} \sum_{\mathbf{k}, \varepsilon_{\mathbf{k}} > 0} \left[\ln(1 + e^{-\beta\varepsilon_{\mathbf{k}}}) + \frac{\beta}{2} \varepsilon_{\mathbf{k}} \right] + U_0 \\ &= -\frac{3}{2\beta} \sum_{\mathbf{k}} \ln(1 + e^{-\beta\varepsilon_{\mathbf{k}}}) + U_0, \end{aligned} \quad (2.22)$$

leading via the conditions $\partial F_{\text{MF}} / \partial Z_{\mu} = 0$ to the three self-consistency equations

$$Z_{\mu} = \frac{1}{N} \sum_{\mathbf{k}} f(\varepsilon_{\mathbf{k}}) \sin(\mathbf{k} \cdot \boldsymbol{\delta}_{\mu}), \quad \mu = 1, 2, 3. \quad (2.23)$$

Here, $f(\varepsilon_{\mathbf{k}}) = 1/(e^{\beta\varepsilon_{\mathbf{k}}} + 1)$ is the Fermi function.

Let us now analyze the possible solutions of the above mean-field equations. At sufficiently high temperatures Eq. (2.23) has only the trivial solution $Z_{\mu} = 0$ for all directions μ , but there is a critical temperature below which at least one of the order parameters Z_{μ} is finite. In the vicinity of the critical temperature, the order parameters are small and we may expand the free energy in powers of the Z_{μ} . We obtain

$$\frac{\beta F}{N} = -\frac{3 \ln 2}{2} + \frac{\beta U_0}{N} - \frac{3\beta^2}{16N} \sum_{\mathbf{k}} \varepsilon_{\mathbf{k}}^2 + \frac{\beta^4}{128N} \sum_{\mathbf{k}} \varepsilon_{\mathbf{k}}^4 + \mathcal{O}(Z_{\mu}^6). \quad (2.24)$$

To carry out the momentum integrations over the first Brillouin zone, it is convenient to map the unit cell in reciprocal space onto a rectangle using the volume-preserving transformation

$$k_x = k_1, \quad k_y = k_2 + \frac{2b}{c} k_1. \quad (2.25)$$

Note that with the definitions of the lattice constants shown in Fig. 2.1 (a) the volume of the Brillouin zone is $V_{\text{BZ}} = (2\pi/b)(4\pi/c)$. In the thermodynamic limit $N \rightarrow \infty$, the Brillouin zone integration of any function $f(k_x, k_y)$ can then be written as

$$\begin{aligned} \frac{1}{N} \sum_{\mathbf{k}} f(k_x, k_y) &= \frac{1}{V_{\text{BZ}}} \int_0^{2\pi} dk_1 \int_0^{4\pi} dk_2 f(k_1, k_2 + \frac{2b}{c} k_1) \\ &= \int_0^{2\pi} \frac{dq_1}{2\pi} \int_0^{2\pi} \frac{dq_2}{2\pi} f\left(\frac{q_1}{b}, \frac{q_1 + q_2}{c/2}\right), \end{aligned} \quad (2.26)$$

where in the last line we have set $q_1 = bk_1$ and $q_2 = \frac{c}{2}k_2$. This transformation maps the original anisotropic triangular lattice onto a square lattice, as shown in Fig. 2.1(b). Using the fact that with these definitions $\mathbf{k} \cdot \boldsymbol{\delta}_1 = q_1$, $\mathbf{k} \cdot \boldsymbol{\delta}_2 = q_2$, and $\mathbf{k} \cdot \boldsymbol{\delta}_3 = -q_1 - q_2$, the mean-field energy dispersion can be written as

$$\varepsilon_{\mathbf{k}} = -4[t_1 \sin q_1 + t_2 \sin q_2 - t_3 \sin(q_1 + q_2)], \quad (2.27)$$

where we have defined the hopping energies

$$t_\mu = J_\mu Z_\mu. \quad (2.28)$$

The Brillouin zone integrations in Eq. (2.24) can now easily be carried out,

$$\frac{1}{N} \sum_{\mathbf{k}} \varepsilon_{\mathbf{k}}^2 = 8 \sum_{\mu} t_\mu^2, \quad (2.29)$$

$$\frac{1}{N} \sum_{\mathbf{k}} \varepsilon_{\mathbf{k}}^4 = 96 [t_1^4 + t_2^4 + t_3^4 + 4(t_1^2 t_2^2 + t_2^2 t_3^2 + t_3^2 t_1^2)]. \quad (2.30)$$

Defining $K_\mu = \beta J_\mu$, we obtain for the dimensionless free energy per site,

$$\begin{aligned} \frac{\beta F}{N} = & -\frac{3}{2} \ln 2 + \frac{3}{2} \sum_{\mu} K_\mu (2 - K_\mu) Z_\mu^2 + \frac{3}{4} \sum_{\mu} K_\mu^4 Z_\mu^4 \\ & + 3[(K_1 K_2 Z_1 Z_2)^2 + (K_2 K_3 Z_2 Z_3)^2 + (K_3 K_1 Z_3 Z_1)^2] \\ & + \mathcal{O}(Z_\mu^6). \end{aligned} \quad (2.31)$$

Minimization gives the following three conditions

$$\frac{K_1 - 2}{K_1} = K_1^2 Z_1^2 + 2(K_2^2 Z_2^2 + K_3^2 Z_3^2), \quad \text{if } Z_1 \neq 0, \quad (2.32a)$$

$$\frac{K_2 - 2}{K_2} = K_2^2 Z_2^2 + 2(K_3^2 Z_3^2 + K_1^2 Z_1^2), \quad \text{if } Z_2 \neq 0, \quad (2.32b)$$

$$\frac{K_3 - 2}{K_3} = K_3^2 Z_3^2 + 2(K_1^2 Z_1^2 + K_2^2 Z_2^2), \quad \text{if } Z_3 \neq 0. \quad (2.32c)$$

Let us first consider the isotropic case $K_1 = K_2 = K_3 = K = \beta J$. Naively, one might then look for a solution $Z_1 = Z_2 = Z_3 = Z$ in the low-temperature regime. In this case, the three self-consistency equations (2.32a–2.32c) reduce to the single equation

$$Z^2 = \frac{K - 2}{3K^3} \quad (2.33)$$

which has only a solution if $K \geq 2$, i.e. $T \leq J/2$. The corresponding free energy is

$$\frac{\beta F}{N} = -\frac{3}{2} \ln 2 - \frac{(K - 2)^2}{4K^2}. \quad (2.34)$$

It turns out, however, that even for the isotropic triangular lattice antiferromagnet a one-dimensional Majorana state has lower energy. To see this, let us assume that only Z_1 is non-zero while $Z_2 = Z_3 = 0$. Then we obtain from Eq. (2.32a)

$$Z_1^2 = \frac{K - 2}{K^3} \quad (2.35)$$

and for the corresponding free energy,

$$\frac{\beta F}{N} = -\frac{3}{2} \ln 2 - 3 \frac{(K - 2)^2}{4K^2}. \quad (2.36)$$

The energy gain for $K > 2$ is three times as large as in the isotropic Majorana state. Hence, our Majorana mean-field theory predicts that in the isotropic triangular lattice the discrete three-fold rotational symmetry of the lattice is spontaneously broken for temperatures below $T_c = J/2$. The emergent Majorana fermions can then propagate coherently only in one direction. Note that finite temperature phase transitions with spontaneous breaking of the discrete rotational symmetry of the underlying lattice have also been found in other frustrated continuous spin models [66–68].

Consider now the anisotropic triangular lattice relevant to Cs_2CuCl_4 with couplings $J_1 = J$ and $J_2 = J_3 = J' \approx J/3$. By repeating the above analysis, it is easy to see that also in this case the free energy is minimized by a one-dimensional Majorana state, where the Majorana fermions can only propagate along the direction of the largest exchange coupling associated with the crystallographic b axis (the x axis in our notation) in Cs_2CuCl_4 . With $J = 4.34$ K, we predict that for vanishing magnetic field the transition to the spin-liquid phase in Cs_2CuCl_4 should occur at $T_c = J/2 = 2.17$ K. A simple calculation shows that at this temperature the specific heat C should exhibit a maximum, as shown in Fig. 2.2. Indeed, in the experimental work by Radu *et al.* [14] the temperature of the spin-liquid transition was identified with the temperature where the specific heat exhibits a maximum, which yields $T_c \approx 2.1$ K for vanishing magnetic field, in excellent agreement with our prediction. An alternative estimate of T_c due to Coldea *et al.* [1] identified the transition temperature to the spin-liquid phase with the temperature where the spin susceptibility exhibits a maximum, leading to the estimate $T_c \approx 2.65$ K for vanishing magnetic field, based on measurements by Carlin *et al.* [69], while a more recent study of magnetic susceptibilities by Tokiwa *et al.* [19] finds $T_c \approx 2.8$ K. Another alternative estimate of the transition temperature by Vachon *et al.* [11], which is based on NMR measurements, leads to $T_c \approx 2.5$ K.

Although in Cs_2CuCl_4 the weak interplane exchange and the Dzyaloshinskii-Moriya interaction stabilize a magnetically ordered state for temperatures below $T_N \approx 0.62$ K, let us briefly discuss the mean-field results for the two-dimensional anisotropic triangular lattice antiferromagnet (2.1) in the limit of vanishing temperature. The free energy (2.22) then reduces to the ground state energy

$$E_0 = \lim_{\beta \rightarrow \infty} F = \frac{3}{2} \sum_{\mathbf{k}} \Theta(-\varepsilon_{\mathbf{k}}) \varepsilon_{\mathbf{k}} + U_0, \quad (2.37)$$

and the self-consistency equations (2.23) can be written as

$$Z_{\mu} = \frac{1}{N} \sum_{\mathbf{k}} \Theta(-\varepsilon_{\mathbf{k}}) \sin(\mathbf{k} \cdot \boldsymbol{\delta}_{\mu}), \quad \mu = 1, 2, 3. \quad (2.38)$$

Note that under the summation sign we may replace

$$\Theta(-\varepsilon_{\mathbf{k}}) \rightarrow \frac{1}{2} [\Theta(-\varepsilon_{\mathbf{k}}) - \Theta(\varepsilon_{\mathbf{k}})] = -\frac{1}{2} \text{sgn} \varepsilon_{\mathbf{k}}. \quad (2.39)$$

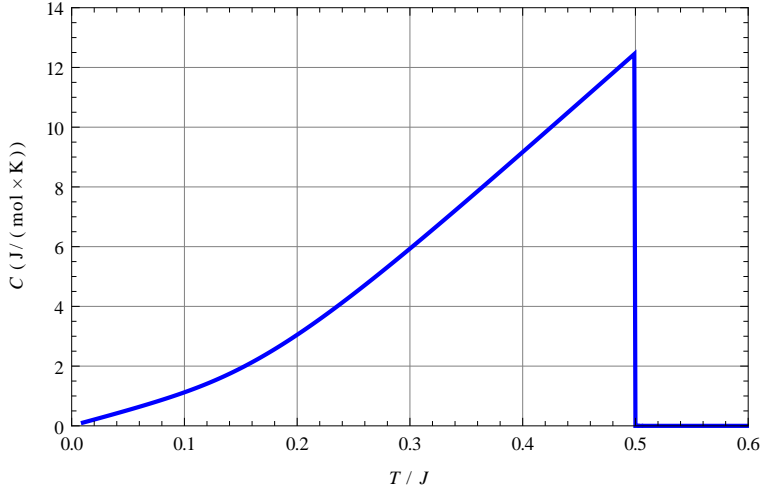


Figure 2.2: Temperature dependence of our mean-field result for the specific heat C for $B = 0$ and $J'/J = 1/3$. Note that for $T < T_c = J/2$ only the variational parameter Z_1 associated with the strongest bond $J_1 = J$ is finite.

Setting for simplicity $J_2 = J_3 = J'$, we may restrict the variational parameters to the surface $Z_2 = Z_3$.³ Graphs of the ground state energy per site as a function of the two variational parameters Z_1 and Z_2 for two different values of J'/J are shown in Fig. 2.3. Note that even for isotropic couplings $J_1 = J_2 = J_3$ the mean-field ground state is one dimensional. In fact, with $Z_1 \neq 0$ and $Z_2 = Z_3 = 0$ it is easy to show analytically that $Z_1 = 1/\pi$ and $E_0^{(1d)}/N = -3J/\pi^2$; on the other hand, if we assume an isotropic mean-field ground state we find $Z_1 = Z_2 = Z_3 = 1/(3\pi)$ and $E_0^{(2d)}/N = -J/\pi^2$. Hence, the energy gain in the one-dimensional mean-field ground state is three times larger than in the isotropic state. For a better comparison of the energies, we show in Fig. 2.4 cuts through the energy surfaces along three different paths in the plane of variational parameters. The important point is that the dimensional reduction scenario found at finite temperatures within the framework of the order parameter expansion remains valid even at $T = 0$. In particular, even in the isotropic case $J = J'$ the mean-field state where the Majorana fermions can only propagate in one direction has the lowest energy. The fact that the isotropic mean-field solution has higher energy has not been noticed in Ref. [55]. The Fermi surface of the Majorana fermions is then one-dimensional (the line $k_x = 0$) and breaks the discrete rotational symmetry of the underlying lattice. For electronic systems, such a symmetry reduction of the Fermi surface is called a Pomeranchuk instability [70], which is an electronic analog of the nematic transition in liquid crystals.

³When setting $Z_2 = Z_3$, we have to be careful in the case of $J' > J$. In that case the energy can be further lowered by setting $Z_1 = 0$, $Z_2 = 0$, and $Z_3 \neq 0$ (or equivalently $Z_3 = 0$ and $Z_2 \neq 0$).

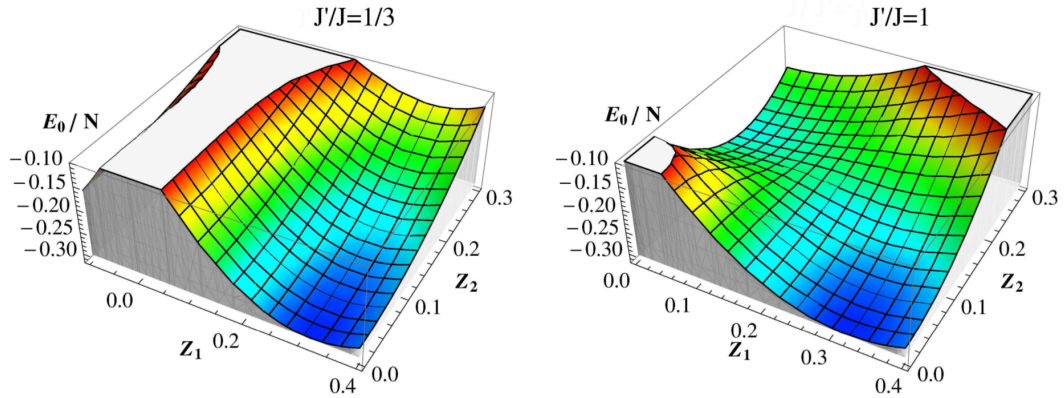


Figure 2.3: Numerical evaluation of the mean-field result (2.37) of the ground state energy per site as a function of $Z = Z_1$ and $Z' = Z_2 = Z_3$ for different values of J'/J as indicated.

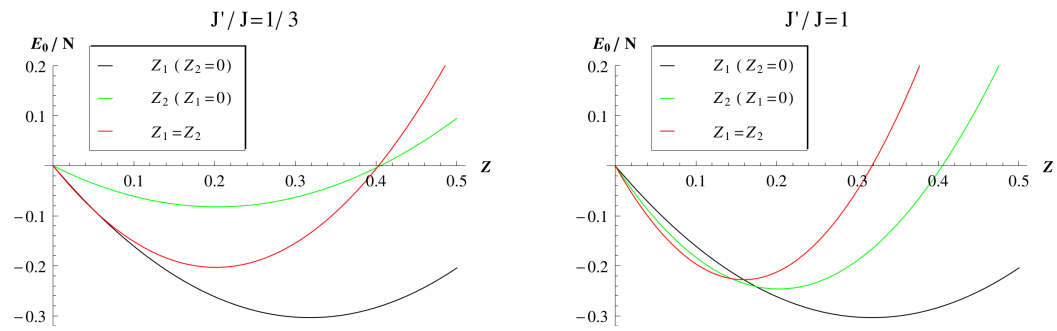


Figure 2.4: Cuts through the energy surfaces shown in Fig. 2.3 along different lines in the space of variational parameters.

2.3 Majorana mean-field theory in a magnetic field

If Cs_2CuCl_4 is exposed to a magnetic field along the crystallographic a axis, the critical temperature for spin-liquid behavior is reduced, as shown by the dashed line in Fig. 1.2. In this section, we shall calculate the magnetic field dependence of the transition temperature $T_c(B)$ using Majorana mean-field theory. Of course, in the vicinity of the quantum critical point at $B_c \approx 8.5$ T spin fluctuations play an important role so that mean-field theory is not reliable. However, for $B \lesssim 0.8B_c$ our Majorana mean-field theory describes the experimental data for $T_c(B)$ quite well.

Using again the representation (2.2) of the spin operators in terms of Majorana fermions, our spin Hamiltonian (2.1) can be written as

$$\mathcal{H} = \frac{1}{4} \sum_{ij} \sum_{\alpha \neq \beta} J_{ij} C_{ij}^{\alpha} C_{ij}^{\beta} + ih \sum_i \eta_i^x \eta_i^y, \quad (2.40)$$

where again $C_{ij}^{\alpha} = \eta_i^{\alpha} \eta_j^{\alpha}$. As a first try, let us follow Ref. [55] and decouple the exchange term in exactly the same way as in zero field, see Eq. (2.6). Using the same notations as in Sec. 2.2, we then obtain the mean-field Hamiltonian

$$\mathcal{H}_{\text{MF}} = i \sum_{ij\alpha} t_{ij} \eta_i^{\alpha} \eta_j^{\alpha} + ih \sum_i \eta_i^x \eta_i^y + U_0. \quad (2.41)$$

In momentum space, this assumes the form

$$\mathcal{H}_{\text{MF}} = \frac{1}{2} \sum_{\mathbf{k}} (\eta_{-\mathbf{k}}^x, \eta_{-\mathbf{k}}^y, \eta_{-\mathbf{k}}^z) \begin{pmatrix} \varepsilon_{\mathbf{k}} & ih & 0 \\ -ih & \varepsilon_{\mathbf{k}} & 0 \\ 0 & 0 & \varepsilon_{\mathbf{k}} \end{pmatrix} \begin{pmatrix} \eta_{\mathbf{k}}^x \\ \eta_{\mathbf{k}}^y \\ \eta_{\mathbf{k}}^z \end{pmatrix} + U_0. \quad (2.42)$$

For a given \mathbf{k} the above 3×3 matrix has the eigenvalues $\varepsilon_{\mathbf{k}} + sh$, where s assumes the values $-1, 0, 1$. The free energy is therefore

$$F = -\frac{1}{2\beta} \sum_{\mathbf{k}, s} \ln [1 + e^{-\beta(\varepsilon_{\mathbf{k}} + sh)}] + U_0. \quad (2.43)$$

The self-consistency equations for the variational parameters Z_{μ} are

$$Z_{\mu} = \frac{1}{3N} \sum_{\mathbf{k}, s} f(\varepsilon_{\mathbf{k}} + sh) \sin(\mathbf{k} \cdot \boldsymbol{\delta}_{\mu}), \quad \mu = 1, 2, 3. \quad (2.44)$$

Expanding the free energy to fourth order in the variational parameters Z_{μ} ,

we obtain

$$\begin{aligned} \frac{\beta F}{N} &= -\frac{1}{2}[\ln 2 + \ln(1 + e^{\beta h}) + \ln(1 + e^{-\beta h})] \\ &+ \frac{3}{2} \sum_{\mu} K_{\mu} [2 - K_{\mu} f_2(\beta h)] Z_{\mu}^2 \\ &+ \frac{3}{4} f_4(\beta h) \left[\sum_{\mu} K_{\mu}^4 Z_{\mu}^4 + 4(K_1 K_2 Z_1 Z_2)^2 \right. \\ &\quad \left. + 4(K_2 K_3 Z_2 Z_3)^2 + 4(K_3 K_1 Z_3 Z_1)^2 \right], \end{aligned} \quad (2.45)$$

with

$$f_2(x) = \frac{1}{3} + \frac{2}{3 \cosh^2(x/2)}, \quad (2.46)$$

$$f_4(x) = \frac{8}{3} \sum_s \frac{e^{sx}(4e^{sx} - 1 - e^{2sx})}{(1 + e^{sx})^4}. \quad (2.47)$$

We have normalized the above functions such that $f_2(0) = f_4(0) = 1$. The magnetic field dependence of the critical temperature is obtained from the condition that the coefficient of the quadratic term in the expansion (2.45) of the free energy vanishes, leading to the self-consistency equation

$$\frac{T_c}{J} = \frac{1}{6} + \frac{1}{3 \cosh^2[h/(2T_c)]}. \quad (2.48)$$

A numerical solution of this equation for the parameters relevant for Cs_2CuCl_4 gives the dashed line in Fig. 2.5. Obviously, the shape of this curve does not agree with the experimentally observed $T_c(B)$ shown in Fig. 1.2, so that at first sight it seems that the magnetic field dependence of the transition temperature to the spin-liquid phase in Cs_2CuCl_4 is not well described by Majorana mean-field theory. However, the mean-field decoupling used to derive Eq. (2.48) is not self-consistent, because in the presence of a magnetic field the expectation values $\langle \eta_i^x \eta_i^y \rangle$ are finite and should be taken into account in our mean-field decoupling. In the presence of a magnetic field, we should therefore replace the decoupling (2.6) by

$$\begin{aligned} \mathbf{S}_i \cdot \mathbf{S}_j &= \frac{1}{2} \sum_{\alpha \neq \beta} \eta_i^{\alpha} \eta_j^{\alpha} \eta_i^{\beta} \eta_j^{\beta} \\ &\rightarrow \frac{1}{2} \sum_{\alpha \neq \beta} \left(C_{ij}^{\alpha} \langle C_{ij}^{\beta} \rangle + \langle C_{ij}^{\alpha} \rangle C_{ij}^{\beta} - \langle C_{ij}^{\alpha} \rangle \langle C_{ij}^{\beta} \rangle \right) \\ &\quad - (\eta_i^x \eta_i^y \langle \eta_j^x \eta_j^y \rangle + \langle \eta_i^x \eta_i^y \rangle \eta_j^x \eta_j^y - \langle \eta_i^x \eta_i^y \rangle \langle \eta_j^x \eta_j^y \rangle). \end{aligned} \quad (2.49)$$

The additional terms renormalize the effective magnetic field acting on the spins, so that we should replace the external field h by

$$b = h - \tilde{J}_0 m, \quad (2.50)$$

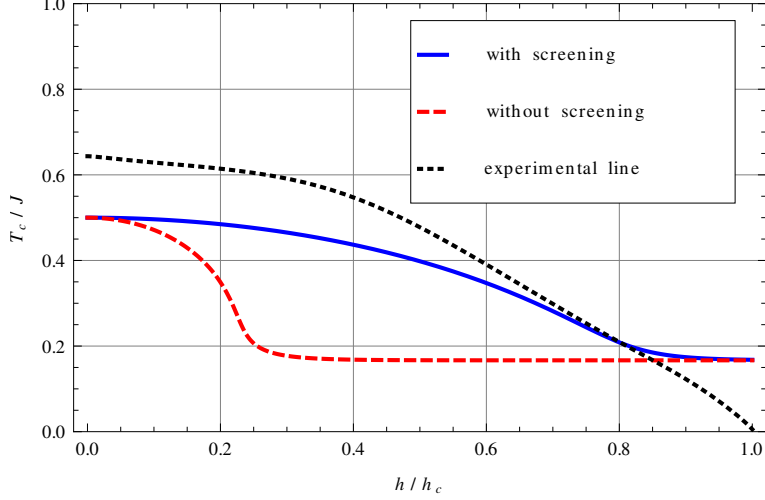


Figure 2.5: Mean-field results for the magnetic field dependence of the critical temperature for spin-liquid behavior in Cs_2CuCl_4 . The dashed line is obtained from Eq. (2.48), which does not take into account the self-consistent screening of the external magnetic field. The solid line takes this effect into account, see Eqs. (2.56) and (2.57). The dotted line indicates the experimental crossover line from Ref. [35], see also Fig. 1.2.

where

$$\tilde{J}_0 = 2 \sum_{\mu} J_{\mu} \quad (2.51)$$

is the Fourier transform of the exchange couplings at vanishing wave-vector. The dimensionless magnetic moment m (per site) satisfies the self-consistency equation

$$m = \frac{1}{2N} \sum_{\mathbf{k}} [f(\varepsilon_{\mathbf{k}} - b) - f(\varepsilon_{\mathbf{k}} + b)]. \quad (2.52)$$

The energy dispersion $\varepsilon_{\mathbf{k}}$ is formally identical to the dispersion (2.14) but with variational parameters Z_{μ} determined by

$$Z_{\mu} = \frac{1}{3N} \sum_{\mathbf{k}, s} f(\varepsilon_{\mathbf{k}} + sb) \sin(\mathbf{k} \cdot \boldsymbol{\delta}_{\mu}), \quad \mu = 1, 2, 3. \quad (2.53)$$

The self-consistency equations (2.52) and (2.53) can be obtained by calculating the extrema⁴ of the free energy

$$F = -\frac{1}{2\beta} \sum_{\mathbf{k}, s} \ln [1 + e^{-\beta(\varepsilon_{\mathbf{k}} + sb)}] + U_0. \quad (2.54)$$

⁴It should be noted that the *variational* mean-field parameters are actually determined by the *saddle points* (not necessarily the minima) of the mean-field free energy generated by mean-field decouplings of the form given in Eqs. (2.6) and (2.49). For a careful discussion of the subtleties related to this type of mean-field ansatz and the interpretation of the resulting free energy in terms of the variational principle, see Ref. [62].

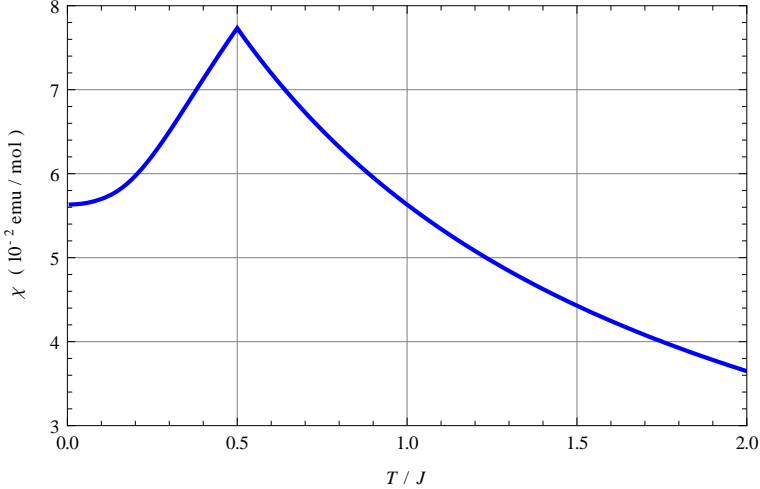


Figure 2.6: Magnetic susceptibility $\chi \approx M/B$ as a function of T/J for $J'/J = 1/3$ and $h/J = 0.01$, corresponding to an external magnetic field $B \approx 0.03$ T.

where the potential U_0 is now

$$U_0 = N \sum_{\mu} J_{\mu} [3Z_{\mu}^2 - m^2]. \quad (2.55)$$

We find that the critical temperature satisfies

$$\frac{T_c}{J} = \frac{1}{6} + \frac{1}{3 \cosh^2[(h - \tilde{J}_0 m_c)/(2T_c)]}, \quad (2.56)$$

where the effective magnetic moment m_c at the critical temperature is determined by

$$m_c = \frac{1}{2} \tanh \left[(h - \tilde{J}_0 m_c)/(2T_c) \right]. \quad (2.57)$$

For a given value of the magnetic field, the coupled equations (2.56) and (2.57) should be solved simultaneously to obtain T_c and m_c as a function of h . Substituting the parameters relevant for Cs_2CuCl_4 ($h_c/J = 2.85$ and $\tilde{J}_0/h_c = 1.18$), the resulting critical temperature is shown as a solid line in Fig. 2.5, which agrees quite well with the experimentally determined crossover temperature up to fields $B \lesssim 0.8B_c$. The magnetic susceptibility $\chi \approx M/B$ (where M is the macroscopic magnetization) exhibits a maximum at the critical temperature $T_c = J/2 = 2.17$ K, as shown in Fig. 2.6. For completeness, we show in Fig. 2.7 the self-consistent magnetic moment m_c and the effective magnetic field $h - \tilde{J}_0 m_c$ at the critical temperature. Note that the antiferromagnetic coupling tends to screen the external magnetic field, so that a stronger external field is needed to generate a given effective field. As a consequence, the reduction of the critical temperature as a function of the external field is weaker than in the naive mean-field decoupling neglecting the screening effect.

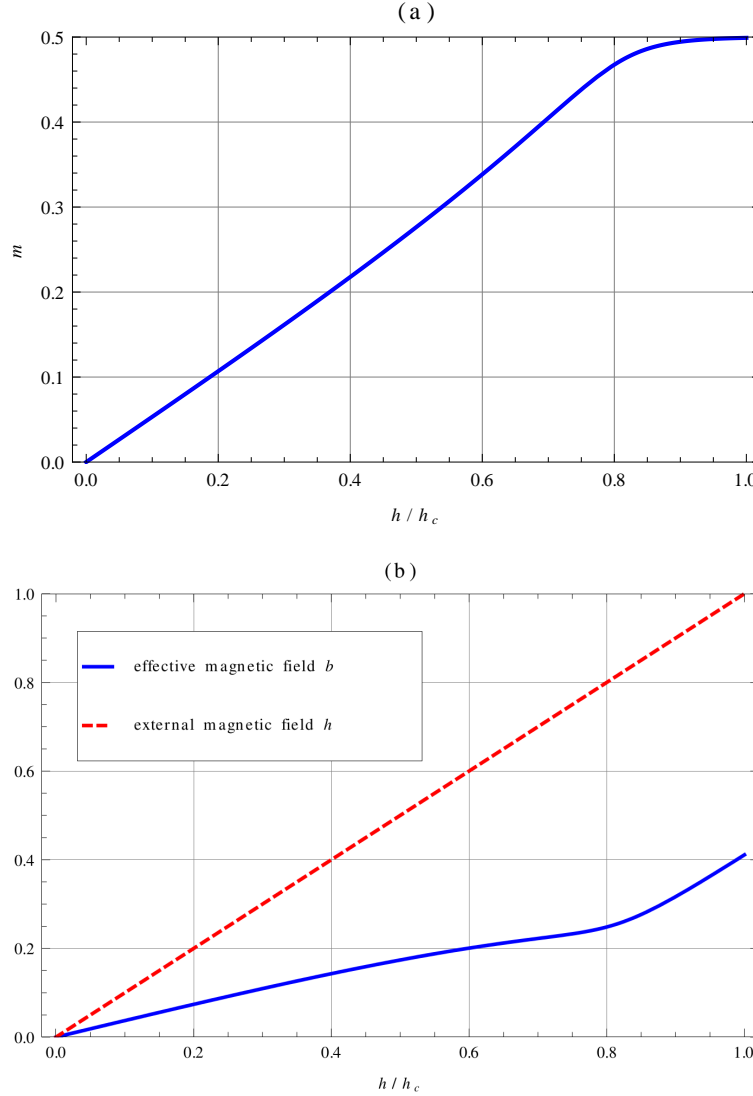


Figure 2.7: (a) Self-consistent dimensionless magnetic moment m_c at the critical temperature of the spin-liquid transition as a function of the external magnetic field, see Eqs. (2.56) and (2.57). (b) Effective magnetic field $b = h - \tilde{J}_0 m_c$ at the critical temperature of the spin-liquid transition. The dashed line is the external magnetic field.

2.4 Summary and conclusions

In summary, we have developed a simple mean-field description of the finite temperature spin-liquid phase in Cs_2CuCl_4 based on the representation of the spin operators in terms of Majorana fermions. We have argued that the experimentally observed crossover temperature for spin-liquid behavior in Cs_2CuCl_4 can be identified with the critical temperature $T_c(B)$ below which the mean-field equations for the dispersion of the Majorana fermions have a finite solution. For small external fields, the emergence of the spin-liquid state gives rise to a maximum in the specific heat and the spin susceptibility as a function of temperature at $T_c = J/2$. We have found that a coherent motion of the Majorana fermions is only possible along the direction of the strongest bond, in agreement with the dimensional reduction scenario discussed by Balents [9]. The emergent one-dimensional Fermi surface of the Majorana fermions is associated with a nematic instability where the discrete rotational symmetry of the lattice is broken.

Given the values of the exchange couplings, our mean-field theory yields an expression for $T_c(B)$ without further adjustable parameters, which agrees quantitatively with the experimentally observed crossover temperature for spin-liquid behavior in Cs_2CuCl_4 up to fields $B \lesssim 0.8B_c$. For larger fields our Majorana mean-field theory is not reliable any more because other types of excitations such as spin fluctuations become important.

Our Majorana mean-field theory is complementary to the approach developed by Starykh and co-authors [6, 65], where Cs_2CuCl_4 is regarded as an array of weakly coupled Heisenberg chains which can be analyzed using bosonization techniques. Given the rather large value of $J'/J \approx 1/3$ in Cs_2CuCl_4 , the validity of this approach is not obvious. In contrast, our Majorana approach treats the system *a priori* as two dimensional; the one-dimensional nature of the Majorana fermions in the spin-liquid phase appears simply as the result of our mean-field calculation. In both methods, the dimensional reduction in the presence of a substantial value of J' is somewhat surprising. The agreement of our Majorana mean-field theory with experiments probing the spin-liquid phase suggests that the Majorana fermions which are formally introduced via the representation (2.2) have a significant overlap with the dominant physical excitations in the finite temperature spin-liquid phase of Cs_2CuCl_4 .

Chapter 3

Ultrasound properties of the spin-liquid phase

3.1 Introduction

In the previous chapter, we have found that the spin excitations in the anisotropic triangular lattice antiferromagnet are quasi-one-dimensional and propagate dominantly along the direction corresponding to the largest exchange coupling, which is the crystallographic b axis in Cs_2CuCl_4 . This dimensional reduction of the elementary excitations has been observed in several independent calculations [P2, 3–8, 10, 12, 20, 65]. In this chapter we shall give further evidence for this dimensional reduction scenario [9] by showing that ultrasound experiments probing the sound propagation along the b axis can be quantitatively explained using a one-dimensional Heisenberg chain which is coupled to lattice vibrations via the usual exchange-striction mechanism [71].

The spin-phonon interaction and the ultrasonic attenuation in two-dimensional spin liquids have recently been discussed by Zhou and Lee [72], and by Serbyn and Lee [73]. In one-dimensional Heisenberg [74] and XY chains [75] the interaction between the spin degrees of freedom and the phonons were studied a long time ago, but these older works mainly focused on the spin-Peierls transition and treated the spin-phonon interaction in an adiabatic approximation. Moreover, only the first derivative of the exchange coupling with respect to the phonon coordinates were considered, which turns out to be insufficient to explain our ultrasound experiments for the c_{22} mode in Cs_2CuCl_4 .

From the exact Bethe ansatz solution of the spin-1/2 antiferromagnetic Heisenberg chain, we know that the ground state is a spin liquid, exhibiting algebraic correlations but no long-range magnetic order. The elementary excitations above this ground state are spinons carrying spin 1/2. A combination of numerical and analytical methods has lead to an excellent understanding of this model [45]; for example, exact numerical results for the magnetization [76], magnetic susceptibility [77], specific heat [78], and the dynamic structure

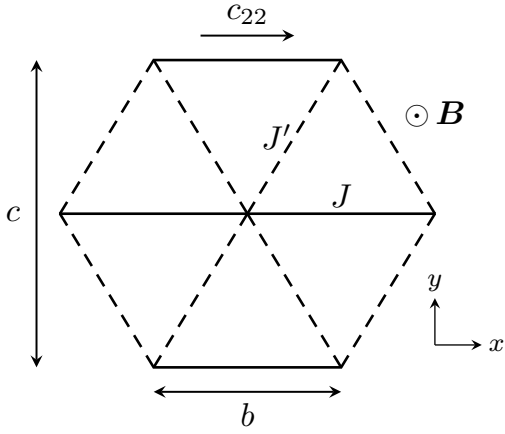


Figure 3.1: Part of the anisotropic triangular lattice formed by the spins in Cs_2CuCl_4 . The largest exchange coupling J connects nearest-neighbor spins along the crystallographic b axis. The corresponding elastic constant is denoted by c_{22} . In this work we consider only the case where the magnetic field \mathbf{B} is along the a axis perpendicular to the plane of the lattice.

factor [79, 80] are available. However, a proper microscopic calculation of ultrasound propagation and attenuation in the Heisenberg chain cannot be found in the literature. Below we shall present a simple solution of this problem using the Jordan-Wigner representation of the spin-algebra in terms of spinless fermions [44]. We shall also present some new data of the elastic constant c_{22} and the corresponding ultrasound damping rate in the spin-liquid phase of Cs_2CuCl_4 which agree very well with our theory.⁵ For details concerning the experiment and the sample preparation we refer to Ref. [27] and Ref. [28], respectively. The ultrasound physics of Cs_2CuCl_4 has previously been studied for magnetic fields along the a axis in the ordered phase using spin-wave theory [27], and for magnetic fields along the b axis in the spin-liquid phase by combining phenomenological expressions for the ultrasound propagation and attenuation with calculations for two-dimensional spin models [26].

The results presented in this chapter have been published in [P3].

3.2 Spin-phonon model

Assuming that the relevant spin excitations can propagate only along the crystallographic b axis in the spin-liquid phase of Cs_2CuCl_4 , we expect that ultrasound experiments probing the c_{22} mode along the b axis can be explained by the following one-dimensional spin-phonon Hamiltonian,

$$\mathcal{H} = \sum_n J_n (\mathbf{S}_n \cdot \mathbf{S}_{n+1} - 1/4) - h \sum_n S_n^z + \mathcal{H}_2^p, \quad (3.1)$$

⁵The experimental measurements have been performed by Pham Thanh Cong [P3].

where \mathbf{S}_n are spin-1/2 operators localized at the positions x_n on a chain with N spins and periodic boundary conditions, and $h = g\mu_B B$ is the Zeeman energy associated with an external magnetic field \mathbf{B} along the crystallographic a axis; see Fig. 3.1. The spin-phonon coupling arises from the fact that for a vibrating lattice the spins are located at $x_n = nb + X_n$, where nb (with $n = 1, \dots, N$) are the points of a one-dimensional lattice with lattice spacing b , and X_n denote the deviations from the lattice points. Since the exchange coupling J_n between a pair of spins \mathbf{S}_n and \mathbf{S}_{n+1} located at x_n and x_{n+1} depends on the actual distance between the spins, J_n is a function of $X_{n+1} - X_n$. Assuming that this difference is small, we may expand to second order,

$$J_n \approx J + J^{(1)}(X_{n+1} - X_n) + \frac{J^{(2)}}{2}(X_{n+1} - X_n)^2, \quad (3.2)$$

where $J^{(1)}$ and $J^{(2)}$ are the first and second derivative of the exchange coupling along the b axis with respect to the phonon coordinates. As usual, we quantize the lattice vibrations by introducing the conjugate momenta P_n and demanding that $[X_n, P_m] = i\delta_{n,m}$. The last term in Eq. (3.1) describes non-interacting phonons with dispersion $\omega_q = c|q|/b$,⁶

$$\mathcal{H}_2^p = \sum_q \left(\frac{P_{-q}P_q}{2M} + \frac{M}{2}\omega_q^2 X_{-q}X_q \right), \quad (3.3)$$

where M is the mass attached to the vibrating sites, and the operators X_q and P_q are defined via the Fourier expansions $X_n = N^{-1/2} \sum_q e^{iqn} X_q$ and $P_n = N^{-1/2} \sum_q e^{iqn} P_q$; the phonon momentum q is given in units of the inverse lattice spacing $1/b$.

3.3 Jordan-Wigner transformation and Hartree-Fock approximation

To explain ultrasound experiments, we will calculate the self-energy correction $\Pi(q, i\bar{\omega})$ to the phonon propagator, which arises from the coupling of the phonons to the spins. Let us therefore represent the spin operators in terms of spinless fermions using the Jordan-Wigner transformation [44, 45] (see Sec. 1.2.2),

$$S_n^+ = (S_n^-)^\dagger = c_n^\dagger (-1)^n e^{i\pi \sum_{j < n} c_j^\dagger c_j}, \quad S_n^z = c_n^\dagger c_n - 1/2, \quad (3.4)$$

where c_n annihilates a fermion at site x_n and the phase factor $(-1)^n$ is introduced for convenience. Our spin-phonon Hamiltonian (3.1) then assumes the

⁶The phonon velocity c in x direction should not be confused with the lattice parameter c in Fig. 3.1. From here on in this chapter, c will denote the phonon velocity.

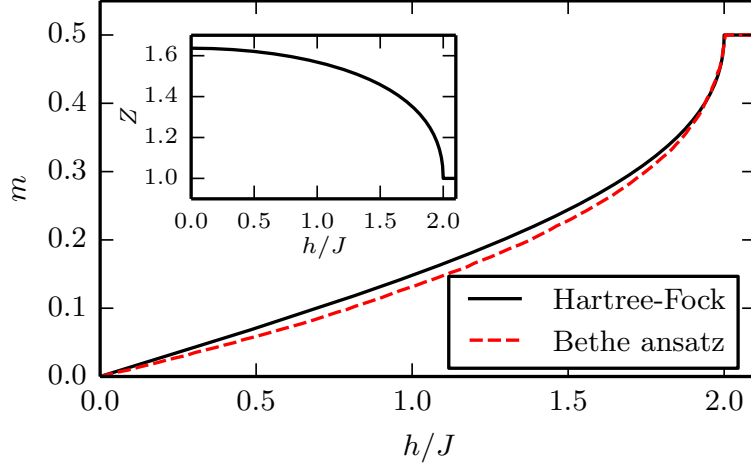


Figure 3.2: Comparison of the Hartree-Fock result for the magnetization curve $m(h)$ of the Heisenberg chain (without phonons) at $T = 0$ with the exact Bethe ansatz [76]. Inset: Renormalization $Z(h)$ of the nearest-neighbor hopping.

form

$$\begin{aligned} \mathcal{H} = & -\frac{1}{2} \sum_n J_n (c_n^\dagger c_{n+1} + c_{n+1}^\dagger c_n + c_n^\dagger c_n + c_{n+1}^\dagger c_{n+1}) \\ & + \sum_n J_n c_n^\dagger c_n c_{n+1}^\dagger c_{n+1} - h \sum_n c_n^\dagger c_n + Nh/2 + \mathcal{H}_2^p. \end{aligned} \quad (3.5)$$

In this work, we shall treat the two-body interaction in the second line of Eq. (3.5) within the self-consistent Hartree-Fock approximation (see Sec. 1.3), which amounts to approximating the two-body term by

$$\begin{aligned} c_n^\dagger c_n c_{n+1}^\dagger c_{n+1} & \approx \rho(c_{n+1}^\dagger c_{n+1} + c_n^\dagger c_n) - \rho^2 \\ & - \tau(c_n^\dagger c_{n+1} + c_{n+1}^\dagger c_n) + \tau^2, \end{aligned} \quad (3.6)$$

where the dimensionless variational parameters ρ and τ satisfy the self-consistency conditions

$$\rho = \langle c_n^\dagger c_n \rangle, \quad \tau = \langle c_n^\dagger c_{n+1} \rangle. \quad (3.7)$$

In the absence of phonons, the solution of these equations was worked out a long time ago by Bulaevskii [81]. Within the Hartree-Fock approximation the fermion dispersion is

$$\xi_k = -ZJ \cos k + 2mJ - h, \quad (3.8)$$

where $Z = 1 + 2\tau$ is the dimensionless renormalization factor of the nearest-neighbor hopping, $m = \rho - 1/2$ is the dimensionless magnetization, and k is the fermion lattice momentum in units of the inverse lattice spacing $1/b$. In Fig. 3.2 we show the numerical result for $Z(h)$ at $T = 0$ and we compare our

mean-field result for $m(h)$ with the exact magnetization curve of the Heisenberg chain obtained via the Bethe ansatz [76].

To obtain the change of the elastic constant and the sound attenuation, we should calculate the self-energy of the phonons due to the coupling to the spins. Substituting the gradient expansion (3.2) for the exchange coupling and the Hartree-Fock decoupling (3.6) into Eq. (3.5), we arrive at the approximate spin-phonon Hamiltonian

$$\mathcal{H} = F_0 + \sum_k \xi_k c_k^\dagger c_k + \mathcal{H}_2^p + \delta\mathcal{H}_2^p + \mathcal{H}_3^{sp} + \mathcal{H}_4^{sp}, \quad (3.9)$$

where $F_0/N = h/2 + J(\tau^2 - \rho^2)$ and

$$\delta\mathcal{H}_2^p = 2J^{(2)}(\tau^2 - \rho^2) \sum_q \sin^2(q/2) X_{-q} X_q, \quad (3.10a)$$

$$\mathcal{H}_3^{sp} = \frac{1}{\sqrt{N}} \sum_{k'kq} \delta_{k',k+q}^* \Gamma_3(k, q) c_{k'}^\dagger c_k X_q, \quad (3.10b)$$

$$\mathcal{H}_4^{sp} = \frac{1}{2N} \sum_{k'kq_1q_2} \delta_{k',k+q_1+q_2}^* \Gamma_4(k, q_1, q_2) c_{k'}^\dagger c_k X_{q_1} X_{q_2}. \quad (3.10c)$$

Here $\delta_{k',k}^* = \sum_m \delta_{k',k+2\pi m}$ enforces momentum conservation modulo a vector of the reciprocal lattice, $c_k = N^{-1/2} \sum_n e^{-ikn} c_n$, and the cubic and quartic interaction vertices are given by

$$\Gamma_3(k, q) = -iZJ^{(1)} [\sin(k+q) - \sin k] + 2imJ^{(1)} \sin q, \quad (3.11a)$$

$$\begin{aligned} \Gamma_4(k, q_1, q_2) = & -ZJ^{(2)} \left[\cos(k+q_1+q_2) - \cos(k+q_2) \right. \\ & \left. + \cos(k) - \cos(k+q_1) \right] \\ & + 2mJ^{(2)} [1 + \cos(q_1+q_2) - \cos(q_1) - \cos(q_2)], \end{aligned} \quad (3.11b)$$

which can be expanded for small phonon momenta,

$$\Gamma_3(k, q) \approx -iqJ^{(1)} (Z \cos k - 2m), \quad (3.12a)$$

$$\Gamma_4(k, q_1, q_2) \approx q_1 q_2 J^{(2)} (Z \cos k - 2m). \quad (3.12b)$$

The coupling to the fermions gives rise to a momentum- and frequency-dependent self-energy correction $\Pi(q, i\bar{\omega})$ to the propagator of the phonon field X_q , which is proportional to $[\bar{\omega}^2 + \omega_q^2 + \Pi(q, i\bar{\omega})]^{-1}$ (see Appendix A).

3.4 Phonon self-energy

To calculate the phonon self-energy $\Pi(q, i\bar{\omega})$, it is convenient to formulate the problem in terms of an imaginary time path integral [37] (see Sec. 1.4). The Euclidean action associated with the Hamiltonian (3.9) is given by

$$S[\bar{c}, c, X] = S_2^s[\bar{c}, c] + S_2^p[X] + S^{sp}[\bar{c}, c, X], \quad (3.13)$$

with a part containing only the fermion fields,

$$S_2^s[\bar{c}, c] = - \int_K (i\omega - \xi_k) \bar{c}_K c_K, \quad (3.14)$$

and a part containing only the phonon fields,

$$S_2^p[X] = \int_Q \frac{M}{2} [\bar{\omega}^2 + \omega_q^2 + \Pi_2(q)] X_{-Q} X_Q. \quad (3.15)$$

The spin-phonon interaction term is

$$\begin{aligned} S^{sp}[\bar{c}, c, X] &= \int_{K', K, Q} \delta(Q + K - K') \Gamma_3(k, q) \bar{c}_{K'} c_K X_Q \\ &+ \frac{1}{2} \int_{Q, Q', K, K'} \delta(K + Q_1 + Q_2 - K') \Gamma_4(k, q_1, q_2) \bar{c}_{K'} c_K X_{Q_1} X_{Q_2}. \end{aligned} \quad (3.16)$$

Here, we describe the phonon dynamics within an Euclidean action where we have integrated over the canonical phonon momenta P_Q in the phase space functional integral representation of the phonons [27, 82]. We have introduced the composite indices $K = (k, i\omega)$ and $Q = (q, i\bar{\omega})$, where we denote fermionic Matsubara frequencies with ω and bosonic Matsubara frequencies with $\bar{\omega}$,

$$\omega = \frac{2\pi(n + \frac{1}{2})}{\beta}, \quad \bar{\omega} = \frac{2\pi n}{\beta}, \quad \text{with } n \in \mathbb{Z}. \quad (3.17)$$

The corresponding sums are

$$\int_K = \frac{1}{\beta N} \sum_{\omega} \sum_k, \quad \int_Q = \frac{1}{\beta N} \sum_{\bar{\omega}} \sum_q, \quad (3.18)$$

and we define

$$\delta(K - K') = \beta N \delta_{\omega, \omega'} \delta_{k, k'}^*. \quad (3.19)$$

The fermion and boson fields in imaginary time have been Fourier transformed to frequency space as

$$X_q(\tau) = \frac{1}{\beta \sqrt{N}} \sum_{\bar{\omega}} e^{-i\bar{\omega}\tau} X_Q, \quad (3.20a)$$

$$c_k(\tau) = \frac{1}{\beta \sqrt{N}} \sum_{\omega} e^{-i\omega\tau} c_K, \quad (3.20b)$$

$$\bar{c}_k(\tau) = \frac{1}{\beta \sqrt{N}} \sum_{\omega} e^{i\omega\tau} \bar{c}_K. \quad (3.20c)$$

Since the action is quadratic in the fermion fields, we can integrate out these fields via the Gaussian integral formula for Grassmann fields [37],

$$\int \mathcal{D}[\bar{c}, c] e^{-\int_{K, K'} A_{K, K'} \bar{c}_K c_{K'}} \propto \text{Det} \hat{A}. \quad (3.21)$$

We separate the matrix \hat{A} into three parts,

$$\hat{A} = -\hat{G}_0^{-1} + \hat{A}^{1p} + \hat{A}^{2p}, \quad (3.22)$$

where $[\hat{G}_0^{-1}]_{K,K'} = \delta(K - K') (i\omega - \xi_k)$ and \hat{A}^{1p} and \hat{A}^{2p} are the terms with one and two phonon fields, respectively. We can now write

$$\text{Det}\hat{A} = e^{\ln \text{Det}\hat{A}} = \text{Det} \left(-\hat{G}_0^{-1} \right) e^{\ln \text{Det}(\hat{1} - \hat{G}_0 [\hat{A}^{1p} + \hat{A}^{2p}])}, \quad (3.23)$$

and expand the logarithm in powers of the phonon fields,⁷

$$\begin{aligned} \ln \text{Det} \left(\hat{1} - \hat{G}_0 [\hat{A}^{1p} + \hat{A}^{2p}] \right) &= \beta N \text{Tr} \ln \left(\hat{1} - \hat{G}_0 [\hat{A}^{1p} + \hat{A}^{2p}] \right) \\ &= -\text{Tr} \left\{ \sum_{n=1}^{\infty} \frac{1}{n} \left[\hat{G}_0 (\hat{A}^{1p} + \hat{A}^{2p}) \right]^n \right\}, \end{aligned} \quad (3.24)$$

with $[\hat{G}_0]_{K,K'} = \delta(K - K') (i\omega - \xi_k)^{-1}$ and $[\hat{1}]_{K,K'} = \delta(K - K')$. The effective action of the phonons up to quadratic order in the phonon fields is then given by

$$S_{\text{eff}}^p[X] = \int_Q \frac{M}{2} [\bar{\omega}^2 + \omega_q^2 + \Pi(Q)] X_{-Q} X_Q, \quad (3.25)$$

where the phonon self-energy has three contributions, $\Pi(q, i\bar{\omega}) = \Pi_2(q) + \Pi_3(q, i\bar{\omega}) + \Pi_4(q)$, with

$$\Pi_2(q) = (J^{(2)}/M) (\tau^2 - \rho^2) 4 \sin^2(q/2), \quad (3.26a)$$

$$\Pi_3(q, i\bar{\omega}) = \frac{1}{MN} \sum_k \frac{f_k - f_{k+q}}{\xi_k - \xi_{k+q} + i\bar{\omega}} |\Gamma_3(k, q)|^2, \quad (3.26b)$$

$$\Pi_4(q) = \frac{1}{MN} \sum_k f_k \Gamma_4(k, q, -q), \quad (3.26c)$$

and $f_k = (e^{\beta\xi_k} + 1)^{-1}$ is the occupation of the fermion state with momentum k in self-consistent Hartree-Fock approximation. The expansion to quadratic order in the phonon fields corresponds to an expansion to second order in the derivatives of the exchange coupling. From the analytic continuation of the self-energy $\Pi(q, i\bar{\omega})$ to real frequencies, we obtain the renormalized phonon energy and the phonon damping [27] (see Appendix A for a derivation),

$$\tilde{\omega}_q = \omega_q + \frac{\text{Re}\Pi(q, \omega_q + i0)}{2\omega_q}, \quad \gamma_q = -\frac{\text{Im}\Pi(q, \omega_q + i0)}{2\omega_q}. \quad (3.27)$$

⁷Since we define the matrix product with the rescaled sum given in Eq. (3.18), this also requires a rescaling of the matrix operators: $\text{Tr}\hat{A} = \text{tr}[\hat{A}/(\beta N)]$, $\text{Det}\hat{A} = \det[\hat{A}/(\beta N)]$, $\text{Ln}\hat{A} = \ln[\hat{A}/(\beta N)]$. Here, the lowercase operators denote the standard matrix operators.

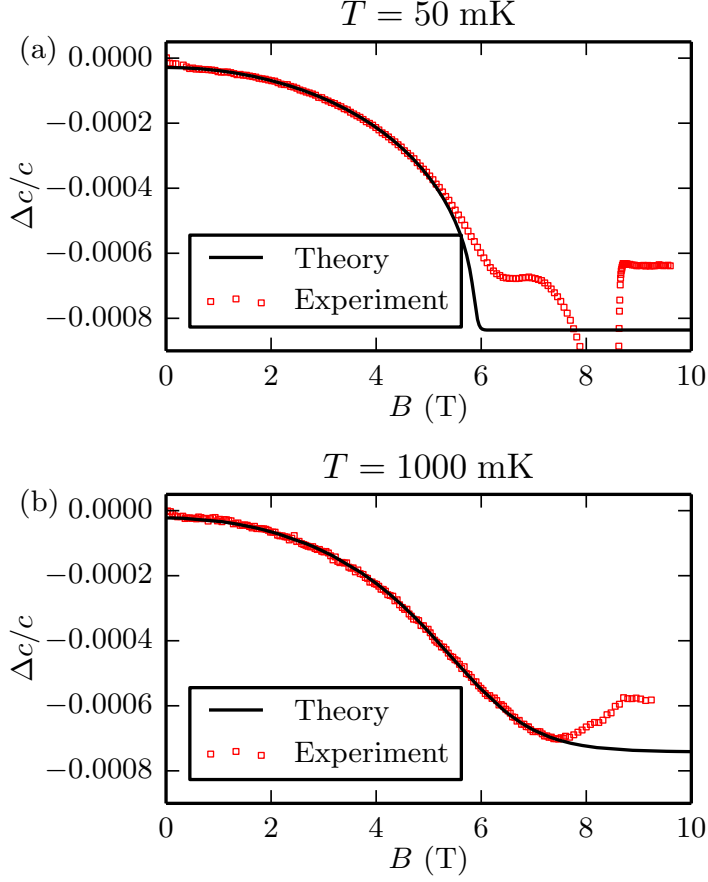


Figure 3.3: Comparison of theory and experiment for the relative change of the sound velocity of the c_{22} mode: (a) in the ordered phase ($T = 50$ mK) with coupling constants $g_1 = 0$ and $g_2 = -1.2 \times 10^{-3}$, (b) in the spin-liquid phase ($T = 1$ K) with coupling constants $g_1 = 0$ and $g_2 = -1.1 \times 10^{-3}$. In the fitting procedure we have allowed a constant offset for $\Delta c/c$ which is necessary due to a small anomaly in the experimental data close to zero magnetic field.

The renormalized phonon velocity can be obtained from $\tilde{c}/c = \lim_{q \rightarrow 0} \tilde{\omega}_q/\omega_q$, which yields for the shift $\Delta c = \tilde{c} - c$,

$$\Delta c/c = g_1 c^{(1)} + g_2 c^{(2)}, \quad (3.28a)$$

$$c^{(1)} = \mathcal{P} \int_{-\pi}^{\pi} \frac{dk}{2\pi} J f'(\xi_k) \frac{v_k}{v_k - c} (2m - Z \cos k)^2, \quad (3.28b)$$

$$c^{(2)} = m^2 - Z^2/4, \quad (3.28c)$$

where \mathcal{P} denotes the Cauchy principal value, $f'(\xi_k) = -\beta f_k(1 - f_k)$ is the derivative of the Fermi function, $v_k = Z J b \sin k$ is the group velocity of the fermionic excitations, and we have introduced the dimensionless coupling constants $g_1 = (J^{(1)} b)^2 / (2 M c^2 J)$ and $g_2 = J^{(2)} b^2 / (2 M c^2)$. In principle it should

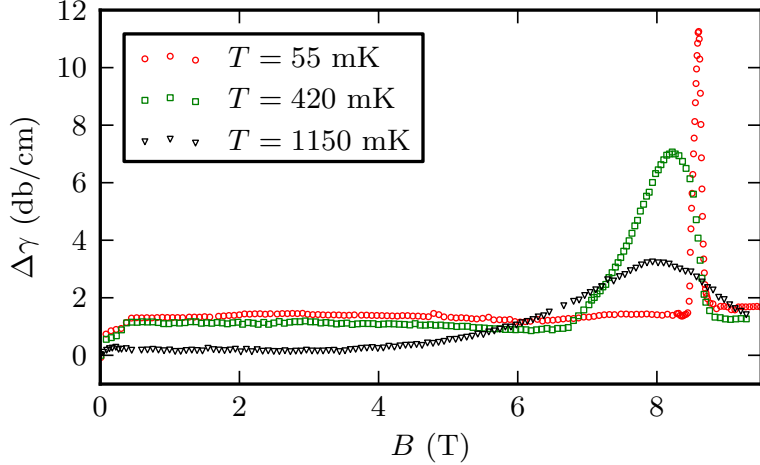


Figure 3.4: Experimental results for the relative change $\Delta\gamma$ of the sound attenuation of the c_{22} mode as a function of the magnetic field for three different temperatures.

be possible to calculate these coupling using *ab initio* methods, but here we simply determine g_1 and g_2 by fitting our theoretical prediction (3.28) to our experimental data. In Fig. 3.3 we show a comparison between theory and experiment as a function of the magnetic field. We find that the relative change of the sound velocity $\Delta c/c$ is best fitted by $g_1 \approx 0$ and $g_2 \approx -1.1 \times 10^{-3}$, which gives $J^{(2)}b^2 \approx -238J$. Only for our experimental data at the highest temperature $T = 1.15$ K, we get a finite value $g_1 = 0.85 \times 10^{-3}$, which gives $J^{(1)}b \approx \pm 14J$. Because of the large value of $c/(Jb) \approx 6.8$, the term $c^{(1)}$ is more than one order of magnitude smaller than $c^{(2)}$ for Cs_2CuCl_4 . While in the ordered phase ($T = 50$ mK, upper panel) our theoretical prediction (3.28) agrees only for magnetic fields up to 5 T with our experimental data, in the spin-liquid phase ($T = 1$ K, lower panel) we obtain excellent agreement between theory and experiment for magnetic fields up to 7 T. A natural explanation for the deviations at larger fields is that in this regime the fluctuations are controlled by the dilute Bose gas quantum critical point at $B_c \approx 8.5$ T [14], which of course cannot be described by our one-dimensional model.

Finally, let us discuss the ultrasound attenuation of the c_{22} mode in Cs_2CuCl_4 . Our experimental data for three different temperatures as a function of the magnetic field are shown in Fig. 3.4. In the regime $B \lesssim 7$ T where the fluctuations controlled by the quantum critical point are negligible and our theoretical prediction for the renormalization of the phonon velocity agrees with experiment, the sound attenuation is very small and practically constant. This can easily be explained within our one-dimensional model. Using Eqs. (3.26b) and (3.27) we obtain for the damping

$$\gamma_q = \frac{\pi}{2M\omega_q} \int_{-\pi}^{\pi} \frac{dk}{2\pi} (f_k - f_{k+q}) |\Gamma_3(k, q)|^2 \delta(\xi_k - \xi_{k+q} + \omega_q). \quad (3.29)$$

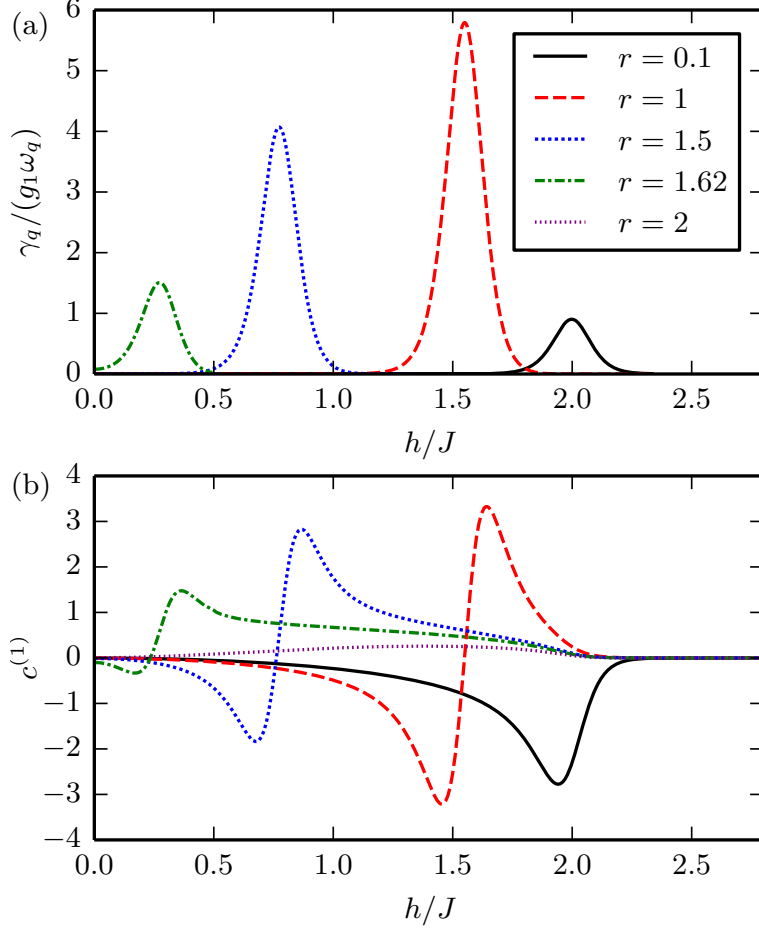


Figure 3.5: (a) Damping γ_q for different values of $r = c/(Jb)$ as a function of the magnetic field at temperature $T/J = 0.05$. (b) Corresponding contribution $c^{(1)}$ to $\Delta c/c$ defined in Eq. (3.28).

This expression is only finite if the absolute value of the maximal group velocity $v_* = ZJb$ of the fermions exceeds the phonon velocity c . Because in Cs_2CuCl_4 this condition is never satisfied ($c/(Jb) \approx 6.8$), the attenuation of the c_{22} mode vanishes in our approximation. Higher orders in perturbation theory will give a finite result, but it will involve more than two derivatives of the exchange coupling which are expected to be small.

On the other hand, the condition $v_* > c$ can possibly be realized in some other quasi-one dimensional quantum antiferromagnet. Let us therefore evaluate Eq. (3.29) in the regime $v_* > c$. In the long-wavelength limit $q \rightarrow 0$, we obtain

$$\frac{\gamma_q}{\omega_q} \sim \frac{g_1 c J \Theta(v_*^2 - c^2)}{2v_* \sqrt{1 - c^2/v_*^2}} [-f'(\xi_+) V_+^2 - f'(\xi_-) V_-^2], \quad (3.30)$$

where $\xi_{\pm} = JV_{\pm} - h$, and $V_{\pm} = 2m \pm Z\sqrt{1 - c^2/v_*^2}$. A numerical evaluation of this expression is shown in the upper panel of Fig. 3.5.

The damping exhibits strong peaks as function of the magnetic field, corresponding to the resonance conditions $\xi_{\pm} = 0$ imposed by the broadened delta functions $-f'(\xi_{\pm})$ in Eq. (3.29). In the lower panel of Fig. 3.5 we show that close to the resonance the corresponding shift $c^{(1)}$ in the phonon velocities can exhibit a sign change depending on the value of $r = c/(Jb)$.

3.5 Summary and conclusions

We have developed a simple microscopic theory which explains ultrasound experiments probing the propagation and the attenuation of the c_{22} mode in the spin-liquid phase of Cs_2CuCl_4 . Our basic assumption is that in the spin-liquid phase the elementary excitations are one-dimensional fermions. Therefore, we have mapped the spin-1/2 operators to spinless fermions via the Jordan-Wigner transformation, where we have treated the interactions between fermions within a self-consistent Hartree-Fock approximation. The coupling between spins and phonons is due to the exchange-striction mechanism where we have expanded the spin-phonon coupling to second order in the phonon fields. We have then calculated the sound velocity and damping of the c_{22} mode using a perturbative expansion to second order in the derivatives of the exchange coupling. The excellent agreement between theory and experiments shown in Fig. 3.3 gives further support to the dimensional reduction scenario advanced by Balents [9]. It would be interesting to test our theoretical predictions for the ultrasound attenuation shown in Fig. 3.5 using suitable antiferromagnetic spin chains with sufficiently small phonon velocities.

Chapter 4

Hard-core boson approach in high magnetic fields

4.1 Introduction

In this chapter, we consider the case of a large magnetic field $B > B_c$ along the a axis, where the magnon excitations are gapped and the ground state is the fully magnetized ferromagnet. Our goal is to describe the thermal excitations above the ground state and to compare with experimental results for the specific heat [14, 15]. We base our theoretical approach on a mapping of the spin-1/2 operators to hard-core bosons [46, 47]. For magnetic fields $B > B_c$ and low temperatures, we then have a dilute gas of gapped hard-core bosons where the ladder approximation captures the leading order low-temperature contributions to the self-energy. Although the ladder approximation has been extensively applied to the Bose-condensed phase of dilute gases of hard-core bosons (see Ref. [17] and references therein), some subtleties related to the hard-core limit in the gapped phase have only recently been discussed by Fauseweh, Stolze, and Uhrig (FSU) [48, 83]. Benchmarking the ladder approximation for an exactly solvable one-dimensional model of hard-core bosons, FSU found that the ladder approximation indeed reproduces the correct low-temperature behavior and that a self-consistent ladder approximation even extends the applicability to arbitrarily high temperatures [48]. In this work, we apply the self-consistent ladder approximation to the relevant two-dimensional model for Cs_2CuCl_4 . For a realistic description of this material, we have to include additional interactions apart from the infinite on-site interaction describing the hard-core constraint. To further explore the range of validity of the self-consistent ladder approximation, we have also applied this method to the exactly solvable one-dimensional XY model; extending the analysis of FSU [48], we have examined the breakdown of the self-consistent ladder approximation in the vicinity of the quantum critical point of this model.

The rest of this chapter is organized as follows. In the next section, we

describe the mapping of the relevant spin model for Cs_2CuCl_4 to an effective hard-core boson model. Then, in Sec. 4.3, we describe our theoretical approach based on the self-consistent ladder approximation for the hard-core interaction and a self-consistent Hartree-Fock decoupling for the remaining non-hard-core interactions. In Sec. 4.4, we investigate the breakdown of the ladder approximation near the quantum critical point for the exactly solvable one-dimensional XY model and in Sec. 4.5 we present our numerical results for Cs_2CuCl_4 , which we compare with experimental data for the specific heat. Finally, in Sec. 4.6 we summarize our main results. We give additional technical details of our calculations in Appendix B.

The results presented in this chapter have been published in [P4].

4.2 Hard-core boson model for Cs_2CuCl_4

We start from the for Cs_2CuCl_4 relevant two-dimensional antiferromagnetic spin-1/2 Heisenberg model in an external magnetic field along the crystallographic a axis [13] (see Sec. 1.1.1 for details),

$$\mathcal{H} = \frac{1}{2} \sum_{ij} [J_{ij} \mathbf{S}_i \cdot \mathbf{S}_j + \mathbf{D}_{ij} \cdot (\mathbf{S}_i \times \mathbf{S}_j)] - h \sum_i S_i^z. \quad (4.1)$$

Here, we will use the hard-core boson representation of the spin-1/2 operators [46, 47] introduced in Sec. 1.2.3,

$$S_i^+ = b_i, \quad S_i^- = b_i^\dagger, \quad S_i^z = 1/2 - b_i^\dagger b_i, \quad (4.2)$$

where the hard-core boson operators satisfy the commutation relation

$$[b_i, b_j^\dagger] = \delta_{ij} (1 - 2b_i^\dagger b_i), \quad (4.3)$$

and the occupation number per site is restricted to $\hat{n}_i = 0$ or 1. The hard-core boson constraint and the commutation relation (4.3) can be realized by treating the hard-core bosons as canonical bosons with an infinite on-site repulsion,

$$\mathcal{H}_U = \frac{U}{2} \sum_i b_i^\dagger b_i^\dagger b_i b_i, \text{ with } U \rightarrow \infty. \quad (4.4)$$

Note that the magnon excitations of the underlying spin system correspond to hard-core boson excitations.

Using Eq. (4.2) to express the spin operators in our Hamiltonian (4.1) in terms of hard-core bosons, we obtain the following hard-core boson Hamiltonian,

$$\mathcal{H} = \sum_{\mathbf{k}} \xi_{\mathbf{k}} b_{\mathbf{k}}^\dagger b_{\mathbf{k}} + \frac{1}{2N} \sum_{\mathbf{k}, \mathbf{k}', \mathbf{q}} (J_{\mathbf{q}} + U) b_{\mathbf{k}+\mathbf{q}}^\dagger b_{\mathbf{k}'-\mathbf{q}}^\dagger b_{\mathbf{k}'} b_{\mathbf{k}} + E_0, \quad (4.5)$$

where we have Fourier transformed the hard-core boson creation and annihilation operators,

$$b_{\mathbf{k}} = \frac{1}{\sqrt{N}} \sum_i b_i e^{-i\mathbf{k}\cdot\mathbf{R}_i}, \quad b_{\mathbf{k}}^\dagger = \frac{1}{\sqrt{N}} \sum_i b_i^\dagger e^{i\mathbf{k}\cdot\mathbf{R}_i}. \quad (4.6)$$

In the following, we will neglect the unimportant constant energy term

$$E_0 = N \left(\frac{J_0}{8} - \frac{h}{2} \right). \quad (4.7)$$

The excitation energy $\xi_{\mathbf{k}}$ in the quadratic part of the Hamiltonian can be written as

$$\xi_{\mathbf{k}} = \varepsilon_{\mathbf{k}} - \mu, \quad (4.8)$$

where we have introduced the chemical potential

$$\mu = h_c - h, \quad (4.9)$$

and the energy dispersion

$$\varepsilon_{\mathbf{k}} = \frac{1}{2} (J_{\mathbf{k}}^D - J_{\mathbf{Q}}^D). \quad (4.10)$$

Here

$$J_{\mathbf{k}}^D = J_{\mathbf{k}} - iD_{\mathbf{k}}, \quad (4.11)$$

where the Fourier transforms of the exchange and Dzyaloshinskii-Moriya interactions are

$$\begin{aligned} J_{\mathbf{k}} &= \sum_{\mathbf{R}} J(\mathbf{R}) e^{-i\mathbf{k}\cdot\mathbf{R}} \\ &= 2J \cos(k_x b) + 4J' \cos(k_x b/2) \cos(k_y c/2), \end{aligned} \quad (4.12)$$

$$\begin{aligned} D_{\mathbf{k}} &= \sum_{\mathbf{R}} D(\mathbf{R}) e^{-i\mathbf{k}\cdot\mathbf{R}} \\ &= -4iD \sin(k_x b/2) \cos(k_y c/2). \end{aligned} \quad (4.13)$$

In Eq. (4.10), $J_{\mathbf{Q}}^D \approx -2.325 J$ is the absolute minimum of $J_{\mathbf{k}}^D$ at $\mathbf{Q} \approx (3.474/b, 0)$. Finally, the saturation field is given by

$$B_c = \frac{h_c}{g\mu_B} = \frac{1}{2g\mu_B} (J_0^D - J_{\mathbf{Q}}^D) \approx 8.4 \text{ T}. \quad (4.14)$$

A contour plot of $\varepsilon_{\mathbf{k}}$ is shown in Fig. 4.1. In the following, we will use the direct experimental value of the saturation field $B_c = 8.44(1)$ T instead of $B_c \approx 8.4$ T because the experimental value is more accurate than a calculation via the Hamiltonian (4.5). The reason is that the interaction constants in Eq. (4.5) have some experimental uncertainty and we have also neglected the interlayer coupling J'' ; including J'' in the calculation would result in $B_c \approx 8.5$ T [14],

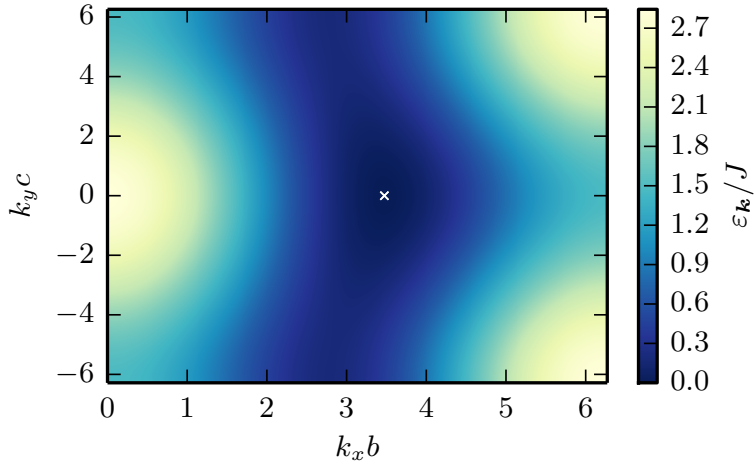


Figure 4.1: Contour plot of the energy dispersion $\varepsilon_{\mathbf{k}}$ defined in Eq. (4.10). The white cross marks the minimum of $\varepsilon_{\mathbf{k}}$ at $\mathbf{Q} \approx (3.474/b, 0)$.

[16]. The value of the saturation field B_c is important because, for a given magnetic field, it determines the energy gap

$$\Delta = -\mu = h - h_c. \quad (4.15)$$

We note that a small change of B_c by 0.04 T changes the gap by about 0.014 J , which is only significant close to the quantum critical point.

4.3 Implementing the self-consistent ladder approximation

In this section, we explain our theoretical approach to the hard-core boson Hamiltonian (4.5). The central problem is how to deal with the interaction part of the Hamiltonian,

$$\mathcal{H}_{\text{int}} = \frac{1}{2N} \sum_{\mathbf{k}, \mathbf{k}', \mathbf{q}} (J_{\mathbf{q}} + U) b_{\mathbf{k}+\mathbf{q}}^\dagger b_{\mathbf{k}'-\mathbf{q}}^\dagger b_{\mathbf{k}'} b_{\mathbf{k}}, \quad (4.16)$$

containing the exchange interaction $J_{\mathbf{q}}$ and the infinite hard-core interaction $U \rightarrow \infty$. We will deal with both interactions using different methods: for the $J_{\mathbf{q}}$ part we use a self-consistent Hartree-Fock decoupling, while for the hard-core interaction U we use the self-consistent ladder approximation [48]. This is necessary because the $J_{\mathbf{q}}$ interaction cannot be easily included in the self-consistent ladder approximation, as this would not allow a direct solution for the effective interaction Γ from the Bethe-Salpeter equation which would significantly complicate matters, especially regarding the limit $U \rightarrow \infty$.

4.3.1 Hartree-Fock decoupling

We approximate the $J_{\mathbf{q}}$ interaction term in Eq. (4.16) using a self-consistent Hartree-Fock decoupling. Therefore, we write this term in real space,

$$\frac{1}{2N} \sum_{\mathbf{k}, \mathbf{k}', \mathbf{q}} J_{\mathbf{q}} b_{\mathbf{k}+\mathbf{q}}^\dagger b_{\mathbf{k}'-\mathbf{q}}^\dagger b_{\mathbf{k}'} b_{\mathbf{k}} = \frac{1}{2} \sum_{i,j} J_{ij} b_i^\dagger b_i b_j^\dagger b_j, \quad (4.17)$$

and then we apply the usual Hartree-Fock decoupling (see Sec. 1.3),

$$\begin{aligned} b_i^\dagger b_i b_j^\dagger b_j &\approx n_i b_j^\dagger b_j + n_j b_i^\dagger b_i - n_i n_j \\ &+ \tau_{ji} b_i^\dagger b_j + \tau_{ij} b_j^\dagger b_i - \tau_{ij} \tau_{ji}, \end{aligned} \quad (4.18)$$

giving

$$\frac{1}{2} \sum_{i,j} J_{ij} b_i^\dagger b_i b_j^\dagger b_j \approx \sum_{i,j} J_{ij} \left(n_j b_i^\dagger b_i + \tau_{ji} b_j^\dagger b_i \right) + E_{\text{MF}}, \quad (4.19)$$

where the Hartree-Fock parameters are given by

$$n_i = \langle b_i^\dagger b_i \rangle, \quad \tau_{ij} = \langle b_i^\dagger b_j \rangle, \quad (4.20)$$

and the constant energy term is

$$E_{\text{MF}} = -\frac{1}{2} \sum_{i,j} J_{ij} (n_i n_j + \tau_{ij} \tau_{ji}). \quad (4.21)$$

Due to translational invariance, we have

$$n_i = n, \quad \tau_{ij} = \tau(\mathbf{R}_i - \mathbf{R}_j). \quad (4.22)$$

Because there is no inversion symmetry, $\tau(\mathbf{R})$ is a complex number satisfying $\tau^*(\mathbf{R}) = \tau(-\mathbf{R})$. Since the exchange coupling $J(\mathbf{R})$ is only non-zero for $\mathbf{R} = \pm \boldsymbol{\delta}_i$, there are three complex Hartree-Fock parameters related to $\tau(\mathbf{R})$,

$$\tau_1 = \tau(\boldsymbol{\delta}_1), \quad \tau_2 = \tau(\boldsymbol{\delta}_2), \quad \tau_3 = \tau(\boldsymbol{\delta}_3). \quad (4.23)$$

However, the Hamiltonian (4.5) is invariant under the transformation $k_y \rightarrow -k_y$ and therefore $\tau_2 = \tau_3$. Transforming Eq. (4.19) back to momentum space, we get

$$\frac{1}{2N} \sum_{\mathbf{k}, \mathbf{k}', \mathbf{q}} J_{\mathbf{q}} b_{\mathbf{k}+\mathbf{q}}^\dagger b_{\mathbf{k}'-\mathbf{q}}^\dagger b_{\mathbf{k}'} b_{\mathbf{k}} \approx \sum_{\mathbf{k}} (J_{\mathbf{k}}^\tau + n J_0) b_{\mathbf{k}}^\dagger b_{\mathbf{k}} + E_{\text{MF}}, \quad (4.24)$$

where

$$J_{\mathbf{k}}^\tau = 2J \text{Re} (\tau_1 e^{i\mathbf{k} \cdot \boldsymbol{\delta}_1}) + 2J' \text{Re} (\tau_2 e^{i\mathbf{k} \cdot \boldsymbol{\delta}_2} + \tau_3 e^{i\mathbf{k} \cdot \boldsymbol{\delta}_3}), \quad (4.25)$$

$$E_{\text{MF}} = -N \left[\frac{J_0}{2} n^2 + J |\tau_1|^2 + J' (|\tau_2|^2 + |\tau_3|^2) \right]. \quad (4.26)$$

The Hartree-Fock approximation gives a constant energy shift E_{MF} , which depends on the magnetic field and the temperature; moreover, the Hartree-Fock approximation leads to a renormalization of single-particle excitation energies $\xi_{\mathbf{k}} \rightarrow \tilde{\xi}_{\mathbf{k}}$, where the renormalized excitation energies are

$$\tilde{\xi}_{\mathbf{k}} = \varepsilon_{\mathbf{k}} - \mu + J_{\mathbf{k}}^{\tau} + nJ_0. \quad (4.27)$$

The self-consistency equations for the Hartree-Fock parameters are given by

$$\tau_i = \tau(\delta_i) = \frac{1}{N} \sum_{\mathbf{k}} n_{\mathbf{k}} e^{-i\mathbf{k}\cdot\delta_i}, \quad (4.28a)$$

$$n = \frac{1}{N} \sum_{\mathbf{k}} n_{\mathbf{k}}, \quad (4.28b)$$

where the occupation number of a state with momentum \mathbf{k} is given by

$$n_{\mathbf{k}} = \langle b_{\mathbf{k}}^\dagger b_{\mathbf{k}} \rangle. \quad (4.29)$$

If we neglect the hard-core interaction, we simply obtain the Bose-Einstein distribution,

$$n_{\mathbf{k}}^{\text{HF}} = \frac{1}{e^{\beta \tilde{\xi}_{\mathbf{k}}} - 1}, \quad (4.30)$$

where $\beta = 1/T$ is the inverse temperature and the renormalized excitation energy $\tilde{\xi}_{\mathbf{k}}$ can be obtained in a straightforward way by solving the self-consistency equations for the Hartree-Fock parameters for $U = 0$. Neglecting the hard-core interaction is possible only for small temperatures $T \ll J$ when the bosons are so dilute that the hard-core interaction does not contribute significantly.

4.3.2 Self-consistent ladder approximation

After the Hartree-Fock decoupling of the $J_{\mathbf{q}}$ interaction, we obtain a Hamiltonian where the only remaining interaction is the infinite on-site repulsion,

$$\mathcal{H} = \sum_{\mathbf{k}} \tilde{\xi}_{\mathbf{k}} b_{\mathbf{k}}^\dagger b_{\mathbf{k}} + \frac{U}{2N} \sum_{\mathbf{k}, \mathbf{k}', \mathbf{q}} b_{\mathbf{k}+\mathbf{q}}^\dagger b_{\mathbf{k}'-\mathbf{q}}^\dagger b_{\mathbf{k}'} b_{\mathbf{k}} + E_{\text{MF}}. \quad (4.31)$$

We will deal with this hard-core interaction using the self-consistent ladder approximation developed in Ref. [48].

Imaginary time path integral formalism

To derive the self-consistent ladder approximation, it is convenient to formulate the problem in terms of an imaginary time path integral [37], as discussed in Sec. 1.4. The Euclidean action associated with the Hamiltonian (4.31) is

$$S[\bar{b}, b] = - \int_K G_0^{-1}(K) \bar{b}_K b_K + \frac{U}{2} \int_{K, K', Q} \bar{b}_{K+Q} \bar{b}_{K'-Q} b_{K'} b_K. \quad (4.32)$$

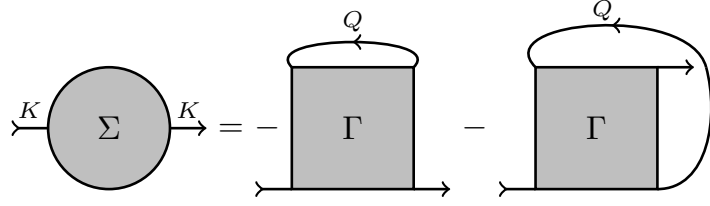


Figure 4.2: Diagrammatic representation of the self-energy in terms of the effective interaction as given in Eq. (4.40).

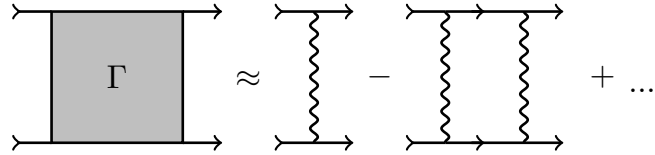


Figure 4.3: Ladder approximation for the effective interaction Γ including all particle-particle ladder diagrams.

The Green function $G(K)$ and the corresponding self-energy $\Sigma(K)$ are defined via the functional average

$$\langle b_K \bar{b}_K \rangle = -\beta N G(K) = -\beta N \frac{1}{G_0^{-1}(K) - \Sigma(K)}, \quad (4.33)$$

where the bare Green function $G_0(K)$ is given by

$$G_0(K) = \frac{1}{i\omega_k - \tilde{\xi}_k}. \quad (4.34)$$

From this path integral formalism a perturbative diagrammatic expansion of the one-particle irreducible self-energy $\Sigma(K)$ can be obtained in terms of the bare Green function $G_0(K)$ and the interaction U , as explained in Sec. 1.4.3.

Self-consistent ladder approximation

Since we are dealing with a strictly non-perturbative problem ($U \rightarrow \infty$), it is necessary to sum over a suitable infinite set of diagrams containing infinite powers of U . Here we approximate the self-energy by summing over all particle-particle ladder diagrams, where we express the self-energy in terms of the effective interaction Γ , as shown in Fig. 4.2. The effective interaction then includes the infinite series of particle-particle ladder diagrams indicated in Fig. 4.3. Formally, this approximation is justified for $\beta\Delta \gg 1$ because the neglected diagrams are of order $\exp(-\beta\Delta)$ smaller than the ladder diagrams.

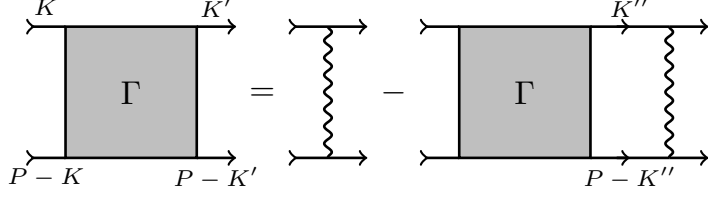


Figure 4.4: Diagrammatic representation of the Bethe-Salpeter equation (4.37) for the effective interaction Γ .

The neglected diagrams for the self-energy include at least two lines going backwards in imaginary time while the ladder diagrams only include a single line of this type; each such line gives a suppression of $\exp(-\beta\Delta)$. This can be seen by considering the bare Green function in imaginary time,

$$G_0(\mathbf{k}, \tau) = \begin{cases} -[1 + n_B(\tilde{\xi}_\mathbf{k})] e^{-\tilde{\xi}_\mathbf{k}\tau}, & \tau > 0 \\ -n_B(\tilde{\xi}_\mathbf{k}) e^{-\tilde{\xi}_\mathbf{k}\tau}, & \tau < 0 \end{cases}, \quad (4.35)$$

where $n_B(x)$ denotes the Bose function,

$$n_B(x) = \frac{1}{e^{\beta x} - 1}. \quad (4.36)$$

We see that $n_B(\tilde{\xi}_\mathbf{k}) \propto \exp(-\beta\Delta)$ for $\beta\Delta \gg 1$ and therefore $G_0(\mathbf{k}, \tau) \propto \exp(-\beta\Delta)$ for $\tau < 0$.

We can go beyond the ladder approximation and include higher order terms by using the full Green function $G(K)$ in the diagrammatic expansion instead of the bare Green function $G_0(K)$ and then finding a self-consistent solution. In this self-consistent ladder approximation, the effective interaction fulfills the Bethe-Salpeter equation shown in Fig. 4.4,

$$\Gamma(K', K; P) = U - U \int_{K''} \Gamma(K'', K; P) G(K'') G(P - K''). \quad (4.37)$$

Because the hard-core interaction U is a constant independent of the momentum transfer, the Bethe-Salpeter equation has the simple solution

$$\Gamma(K', K; P) = \Gamma(P) = \frac{U}{1 + U\Pi(P)}, \quad (4.38)$$

where we have defined the particle-particle bubble

$$\Pi(P) = \int_Q G(Q) G(P - Q). \quad (4.39)$$

The self-energy in the self-consistent ladder approximation is given by

$$\Sigma(K) = -2 \int_Q G(Q)\Gamma(Q+K)e^{i\omega_q 0^+}, \quad (4.40)$$

which is shown diagrammatically in Fig. 4.2. The convergence factor $e^{i\omega_q 0^+}$ implements the correct time ordering at the interaction vertex in the first order term in U where a propagator line starts and ends at the same vertex [37] (see Sec. 1.4.5). The Green function has the spectral representation

$$G(K) = \int_{-\infty}^{\infty} dx \frac{A(\mathbf{k}, x)}{i\omega_k - x}, \quad (4.41)$$

where the spectral function is given by

$$\begin{aligned} A(\mathbf{k}, \omega) &= -\frac{1}{\pi} \text{Im}G(\mathbf{k}, \omega + i0^+) \\ &= -\frac{1}{\pi} \frac{\text{Im}\Sigma^R(\mathbf{k}, \omega)}{\left[\omega - \tilde{\xi}_{\mathbf{k}} - \text{Re}\Sigma^R(\mathbf{k}, \omega)\right]^2 + [\text{Im}\Sigma^R(\mathbf{k}, \omega)]^2}, \end{aligned} \quad (4.42)$$

and the retarded self-energy is obtained by analytic continuation to real frequencies,

$$\Sigma^R(\mathbf{k}, \omega) = \Sigma(\mathbf{k}, \omega + i0^+). \quad (4.43)$$

We note that the spectral function of hard-core bosons fulfills the following sum rule [48],

$$\int_{-\infty}^{\infty} d\omega A(\mathbf{k}, \omega) = \langle [b_{\mathbf{k}}, b_{\mathbf{k}}^\dagger] \rangle = 1 - 2n, \quad (4.44)$$

with⁸

$$n = \frac{1}{N} \sum_{\mathbf{k}} n_{\mathbf{k}} = \frac{1}{N} \sum_{\mathbf{k}} \int_{-\infty}^{\infty} dx A(\mathbf{k}, x) n_B(x). \quad (4.45)$$

Our goal is to calculate the self-consistent solution for the spectral function $A(\mathbf{k}, \omega)$. But before we can do this, we have to take the limit $U \rightarrow \infty$ analytically.

Taking the limit $U \rightarrow \infty$

We can write the effective interaction $\Gamma(P)$ as

$$\Gamma(P) = \frac{1}{\Pi(P)} + \delta\Gamma(P), \quad (4.46)$$

⁸We write here the occupation number $n_{\mathbf{k}}$ in terms of the spectral function via the relation $n_{\mathbf{k}} = \langle b_{\mathbf{k}}^\dagger b_{\mathbf{k}} \rangle = \langle \bar{b}_{\mathbf{k}}(\tau) b_{\mathbf{k}}(\tau - 0^+) \rangle = -\frac{1}{\beta} \sum_{\omega_k} e^{i\omega_k 0^+} G(K) = \int_{-\infty}^{\infty} dx A(\mathbf{k}, x) n_B(x)$, where the shift by 0^+ implements the correct ordering of the operators.

where the second term

$$\delta\Gamma(P) = -\frac{1}{\Pi(P)} \frac{1}{1+U\Pi(P)} \quad (4.47)$$

does also contribute to the $U \rightarrow \infty$ limit because the denominator of $\delta\Gamma(P)$ can vanish at high frequencies $\omega_p \sim \mathcal{O}(U)$ leading to an additional delta function contribution which has to be taken into account. This subtlety of the $U \rightarrow \infty$ limit has been noticed only quite recently by FSU [48]. We now follow FSU to derive the correct hard-core limit for our model. First of all, we note that $\Pi(\mathbf{p}, \omega) \propto 1/\omega$ for $\omega \rightarrow \infty$. This allows us to introduce the spectral representation

$$\Pi(\mathbf{p}, \omega) = \int_{-\infty}^{\infty} dx \frac{\rho(\mathbf{p}, x)}{\omega - x}, \quad (4.48)$$

where

$$\begin{aligned} \rho(\mathbf{p}, \omega) &= -\frac{1}{\pi} \text{Im} \Pi(\mathbf{p}, \omega + i0^+) \\ &= -\frac{1}{N} \sum_{\mathbf{q}} \int_{-\infty}^{\infty} dx A(\mathbf{q}, x) A(\mathbf{p} - \mathbf{q}, \omega - x) [n_B(x) - n_B(-x)]. \end{aligned} \quad (4.49)$$

Now, we use the fact that for $\omega \rightarrow \infty$

$$\Gamma(\mathbf{p}, \omega) - U = \frac{-U^2 \Pi(\mathbf{p}, \omega)}{1 + U \Pi(\mathbf{p}, \omega)} \propto \frac{1}{\omega}, \quad (4.50)$$

because $\Pi(\mathbf{p}, \omega) \propto 1/\omega$ for $\omega \rightarrow \infty$. This implies that $\Gamma(\mathbf{p}, \omega) - U$ has the spectral representation

$$\Gamma(\mathbf{p}, \omega) - U = \int_{-\infty}^{\infty} dx \frac{\bar{\rho}(\mathbf{p}, x)}{\omega - x}, \quad (4.51)$$

where

$$\begin{aligned} \bar{\rho}(\mathbf{p}, \omega) &= -\frac{1}{\pi} \text{Im} [\Gamma(\mathbf{p}, \omega + i0^+)] \\ &= f(\mathbf{p}, \omega) - \frac{1}{\pi} \text{Im} [\delta\Gamma(\mathbf{p}, \omega + i0^+)], \end{aligned} \quad (4.52)$$

with

$$f(\mathbf{p}, \omega) = \frac{-\rho(\mathbf{p}, \omega)}{\left[\mathcal{P} \int_{-\infty}^{\infty} dx \frac{\rho(\mathbf{p}, x)}{\omega - x} \right]^2 + [\pi \rho(\mathbf{p}, \omega)]^2}. \quad (4.53)$$

Here, \mathcal{P} denotes the Cauchy principal value which arises from the identity $1/(\omega + i0^+) = \mathcal{P}(1/\omega) - i\pi\delta(\omega)$. For the contribution of $\delta\Gamma$ to $\bar{\rho}(\mathbf{p}, \omega)$ we recall that the denominator of $\delta\Gamma(\mathbf{p}, \omega)$ can vanish when $\omega \sim \mathcal{O}(U)$ and only in that

case there can be a contribution from $\delta\Gamma$. Therefore, we expand $\Pi(\mathbf{p}, \omega)$ for large frequencies $\omega \sim \mathcal{O}(U)$ (we take U to be very large but finite),

$$\Pi(\mathbf{p}, \omega) \approx \frac{\rho_0(\mathbf{p})}{\omega} + \frac{\rho_1(\mathbf{p})}{\omega^2} + \mathcal{O}\left(\frac{1}{\omega^3}\right), \quad (4.54)$$

where

$$\rho_0(\mathbf{p}) = \int_{-\infty}^{\infty} dx \rho(\mathbf{p}, x), \quad (4.55a)$$

$$\rho_1(\mathbf{p}) = \int_{-\infty}^{\infty} dx x \rho(\mathbf{p}, x). \quad (4.55b)$$

We find

$$\delta\Gamma(P) \approx -\frac{1}{\frac{\rho_0(\mathbf{p})}{\omega} + \frac{\rho_1(\mathbf{p})}{\omega^2} + \mathcal{O}\left(\frac{1}{\omega^3}\right)} \frac{1}{1 + U \frac{\rho_0(\mathbf{p})}{\omega} + U \frac{\rho_1(\mathbf{p})}{\omega^2} + \mathcal{O}\left(\frac{U}{\omega^3}\right)}, \quad (4.56)$$

where the terms $\mathcal{O}(1/\omega^3)$ and $\mathcal{O}(U/\omega^3)$ vanish at the pole $\omega \sim \mathcal{O}(U)$ in the limit $U \rightarrow \infty$, justifying the expansion to order $1/\omega^2$. Therefore, we have

$$\delta\Gamma(P) \approx -\frac{1}{\frac{\rho_0(\mathbf{p})}{\omega} + \frac{\rho_1(\mathbf{p})}{\omega^2}} \frac{\omega^2}{[\omega - \omega_1(\mathbf{p})][\omega - \omega_2(\mathbf{p})]}, \quad (4.57)$$

where the poles are given by

$$\begin{aligned} \omega_1(\mathbf{p}) &= -\frac{U\rho_0(\mathbf{p})}{2} - \sqrt{\frac{U^2\rho_0^2(\mathbf{p})^2}{4} - U\rho_1(\mathbf{p})} \\ &\sim -U\rho_0(\mathbf{p}), \quad U \rightarrow \infty, \end{aligned} \quad (4.58a)$$

$$\begin{aligned} \omega_2(\mathbf{p}) &= -\frac{U\rho_0(\mathbf{p})}{2} + \sqrt{\frac{U^2\rho_0^2(\mathbf{p})^2}{4} - U\rho_1(\mathbf{p})} \\ &\sim -\frac{\rho_1(\mathbf{p})}{\rho_0(\mathbf{p})}, \quad U \rightarrow \infty. \end{aligned} \quad (4.58b)$$

Only the pole at $\omega_1 \sim \mathcal{O}(U)$ is relevant for the analytic continuation in Eq. (4.52) because the other pole at $\omega_2 \sim \mathcal{O}(U^0)$ is spurious, since we have expanded for large frequencies $\omega \sim \mathcal{O}(U)$. In total, we get

$$\bar{\rho}(\mathbf{p}, \omega) = f(\mathbf{p}, \omega) - \frac{1}{\frac{\rho_0(\mathbf{p})}{\omega} + \frac{\rho_1(\mathbf{p})}{\omega^2}} \frac{\omega^2}{\omega - \omega_2(\mathbf{p})} \delta(\omega - \omega_1(\mathbf{p})). \quad (4.59)$$

We can now use the spectral representation (4.51) in Eq. (4.40) and take the limit $U \rightarrow \infty$ to get the following expression for the self-energy,

$$\begin{aligned} \Sigma(K) &= -\frac{2}{N} \sum_{\mathbf{q}} \int_{-\infty}^{\infty} dx \int_{-\infty}^{\infty} dx' A(\mathbf{q}, x') f(\mathbf{q} + \mathbf{k}, x) \frac{n_B(x) - n_B(x')}{i\omega_k + x' - x} \\ &\quad + \frac{2}{N} \sum_{\mathbf{q}} \int_{-\infty}^{\infty} dx A(\mathbf{q}, x) n_B(x) \left[\frac{x + i\omega_k}{\rho_0(\mathbf{q} + \mathbf{k})} - \frac{\rho_1(\mathbf{q} + \mathbf{k})}{\rho_0^2(\mathbf{q} + \mathbf{k})} \right]. \end{aligned} \quad (4.60)$$

By analytic continuation to real frequencies, we obtain the real and imaginary part of the retarded self-energy,

$$\begin{aligned} \text{Re}\Sigma^R(\mathbf{k}, \omega) &= \frac{2}{N} \sum_{\mathbf{q}} \int_{-\infty}^{\infty} dx A(\mathbf{q}, x) n_B(x) \left[\frac{x + \omega}{\rho_0(\mathbf{q} + \mathbf{k})} - \frac{\rho_1(\mathbf{q} + \mathbf{k})}{\rho_0^2(\mathbf{q} + \mathbf{k})} \right] \\ &\quad + \mathcal{P} \int_{-\infty}^{\infty} dx \frac{\rho_{\Sigma}(\mathbf{k}, x)}{\omega - x}, \end{aligned} \quad (4.61a)$$

$$\text{Im}\Sigma^R(\mathbf{k}, \omega) = -\pi \rho_{\Sigma}(\mathbf{k}, \omega), \quad (4.61b)$$

where

$$\rho_{\Sigma}(\mathbf{k}, \omega) = \frac{2}{N} \sum_{\mathbf{q}} \int_{-\infty}^{\infty} dx A(\mathbf{q}, x) f(\mathbf{q} + \mathbf{k}, x + \omega) [n_B(x) - n_B(x + \omega)]. \quad (4.61c)$$

To summarize, we have obtained the self-energy in the limit $U \rightarrow \infty$ which we can calculate starting from an initial spectral function. Via Eq. (4.42) we can then calculate the next iteration of the spectral function allowing us to find a self-consistent solution for the spectral function. After each iteration the Hartree-Fock parameters n , τ_1 , τ_2 , and τ_3 have to be updated via the self-consistency equations (4.28a) and (4.28b) using

$$n_{\mathbf{k}} = \langle b_{\mathbf{k}}^\dagger b_{\mathbf{k}} \rangle = \int_{-\infty}^{\infty} dx A(\mathbf{k}, x) n_B(x). \quad (4.62)$$

4.4 Numerical results for the one-dimensional XY model

Before applying the above approach to the hard-core boson model for Cs_2CuCl_4 , it is instructive to test its validity for the exactly solvable one-dimensional spin-1/2 XY model in a magnetic field. Although a similar model has been already studied in detail in Ref. [48], the breakdown of the self-consistent ladder approximation in the vicinity of the quantum critical point has not been investigated.

The XY model in one dimension is given by

$$\mathcal{H}_{1D} = J \sum_i (S_i^x S_{i+1}^x + S_i^y S_{i+1}^y) - h \sum_i S_i^z, \quad (4.63)$$

which can again be mapped to hard-core bosons (neglecting constant terms),

$$\mathcal{H}_{1D} = \sum_k \xi_k b_k^\dagger b_k + \frac{U}{2N} \sum_{k,k',q} b_{k+q}^\dagger b_{k'-q}^\dagger b_{k'} b_k, \quad (4.64)$$

with excitation energy

$$\xi_k = J [\cos(k_x b) + 1] - \mu, \quad (4.65)$$

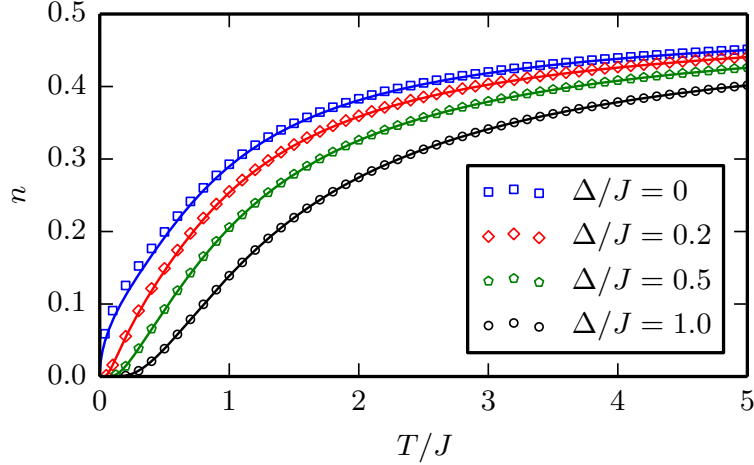


Figure 4.5: Comparison of the results for the boson density n obtained from the self-consistent ladder approximation (symbols) with the exact result (solid lines) at different energy gaps Δ for the one-dimensional XY model.

where $\mu = h_c - h = -\Delta$ and $h_c = J$. An exact solution can be found by mapping the hard-core bosons to fermions via the Jordan-Wigner transformation,

$$b_j = e^{-i\pi \sum_{l < j} c_l^\dagger c_l} c_j, \quad b_j^\dagger = c_j^\dagger e^{i\pi \sum_{l < j} c_l^\dagger c_l}, \quad (4.66)$$

resulting in the quadratic Hamiltonian

$$\mathcal{H}_{1D} = \sum_k \xi_k c_k^\dagger c_k, \quad (4.67)$$

where the operators c_k^\dagger and c_k are fermionic creation and annihilation operators. The hard-core boson density is therefore exactly given by

$$n = \frac{1}{N} \sum_k \frac{1}{e^{\beta \xi_k} + 1}, \quad (4.68)$$

which can be compared to the approximate solution from the self-consistent ladder approximation for the hard-core boson model. We note that for low temperatures at $\mu = 0$, the exact density (4.68) has the following asymptotic behavior,

$$n \sim \frac{\sqrt{2T/J}}{\pi} \int_0^\infty dx \frac{1}{e^{x^2} + 1} \approx 0.241 \sqrt{T/J}, \quad (4.69)$$

in agreement with the expected behavior of one-dimensional bosons at the quantum critical point [84].

In Fig. 4.5 we compare the approximate result for the boson density n obtained within the self-consistent ladder approximation with the exact solution. The relative error $\delta n/n$ of the approximate result is shown in Fig. 4.6 where we define

$$\delta n/n = \frac{n_{\text{ladder}} - n_{\text{exact}}}{n_{\text{exact}}}. \quad (4.70)$$

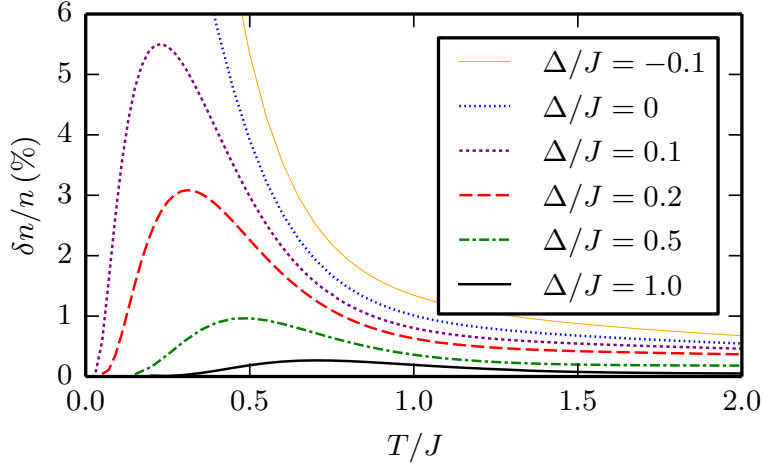


Figure 4.6: Relative error $\delta n/n$ of the boson density (see Eq. (4.70)) in the self-consistent ladder approximation for the one-dimensional XY model as a function of temperature at different energy gaps Δ .

Here, n_{ladder} is the result from the self-consistent ladder approximation and n_{exact} is the exact result. For a finite energy gap, we see that the error vanishes for low and high temperatures with a maximum error at $T \approx \Delta$, while the error becomes smaller for larger energy gaps. For $\Delta = 0$, the error keeps increasing for smaller temperatures, getting closer to the quantum critical point at $T = 0$, but decreases for higher temperatures. We conclude that the self-consistent ladder approximation gives good results over the whole temperature range for finite energy gaps $\Delta \gtrsim 0.1 J$.

4.5 Numerical results for Cs_2CuCl_4

In this section, we apply our hard-core boson approach described in Sec. 4.3 to the relevant model for Cs_2CuCl_4 given in Sec. 4.2. From the numerical solution of the self-consistent ladder approximation, we calculate the spectral function of the hard-core bosons at finite temperatures for different magnetic fields in the regime $B > B_c$ where the energy gap $\Delta > 0$ is finite. Given the spectral function, we can calculate the magnetization, the internal energy, and the transverse part of the spin dynamic structure factor. From the magnetization and internal energy, we obtain the magnetic susceptibility and the specific heat by numerical differentiation. Finally, we compare our results with experimental data for the specific heat [14, 15]. Technical details of the numerical solution of the self-consistent ladder approximation can be found in Appendix B.

4.5.1 Spectral function

Due to the finite energy gap $\Delta > 0$, at zero temperature the spectral function is exactly given by the non-interacting spectral function,

$$A(\mathbf{k}, \omega) = A_0(\mathbf{k}, \omega) = \delta(\omega - \xi_{\mathbf{k}}). \quad (4.71)$$

At finite temperatures, interactions will lead to a renormalization of the excitation energy $\xi_{\mathbf{k}}$ and a broadening of the delta peaks. Since we are treating the J_q interaction term on a Hartree-Fock level, this alone would only renormalize the excitation energy by $\xi_{\mathbf{k}} \rightarrow \tilde{\xi}_{\mathbf{k}}$ resulting in

$$A(\mathbf{k}, \omega) = \delta(\omega - \tilde{\xi}_{\mathbf{k}}). \quad (4.72)$$

Taking in addition the hard-core interaction via the self-consistent ladder approximation into account will lead to a broadening of the spectral function with rising temperature, as shown in Fig. 4.7. Besides the broadening, we notice that the bandwidth shrinks with rising temperature and the minimum of the spectral function gets shifted to higher energies increasing the effective energy gap from its bare value Δ at $T = 0$. In Fig. 4.8 we contrast the behavior of the spectral function at $\mathbf{k} = 0$ and at the minimum of the dispersion $\mathbf{k} = \mathbf{Q}$. While at $\mathbf{k} = 0$ the position of the peak only moves to slightly higher energies, at the minimum of the dispersion the peak gets considerably shifted to higher energies. Due to the finite frequency resolution in our numerical calculation (see Appendix A), we cannot reach arbitrarily low temperatures and are restricted to temperatures $T \gtrsim 0.2\Delta$ where the spectral function is not too narrow to be resolved. However, in the temperature range $T \lesssim 0.2\Delta$, the hard-core interaction can be neglected and we can then just use the self-consistent Hartree-Fock decoupling without hard-core interaction, as we will show further below.

The spectral function can be related to the in-plane components of the spin dynamic structure factor. The spin dynamic structure factor is defined by

$$S^{\alpha\beta}(\mathbf{k}, \omega) = \int_{-\infty}^{\infty} \frac{dt}{2\pi} e^{i\omega t} \left\langle S_{-\mathbf{k}}^{\alpha}(t) S_{\mathbf{k}}^{\beta}(0) \right\rangle, \quad (4.73)$$

where $\alpha, \beta = x, y, z$ and the Fourier transforms of the spin operators are defined via

$$S_{\mathbf{k}}^{\alpha} = \frac{1}{\sqrt{N}} \sum_i e^{-i\mathbf{k}\cdot\mathbf{R}_i} S_i^{\alpha}. \quad (4.74)$$

The in-plane components of the spin dynamic structure factor are given by

$$S^{xx}(\mathbf{k}, \omega) = S^{yy}(\mathbf{k}, \omega) = \frac{1}{4} \frac{1}{1 - e^{-\beta\omega}} [A(\mathbf{k}, \omega) + A(-\mathbf{k}, \omega)], \quad (4.75a)$$

$$S^{xy}(\mathbf{k}, \omega) = -S^{yx}(\mathbf{k}, \omega) = \frac{1}{4} \frac{1}{1 - e^{-\beta\omega}} [A(\mathbf{k}, \omega) - A(-\mathbf{k}, \omega)], \quad (4.75b)$$

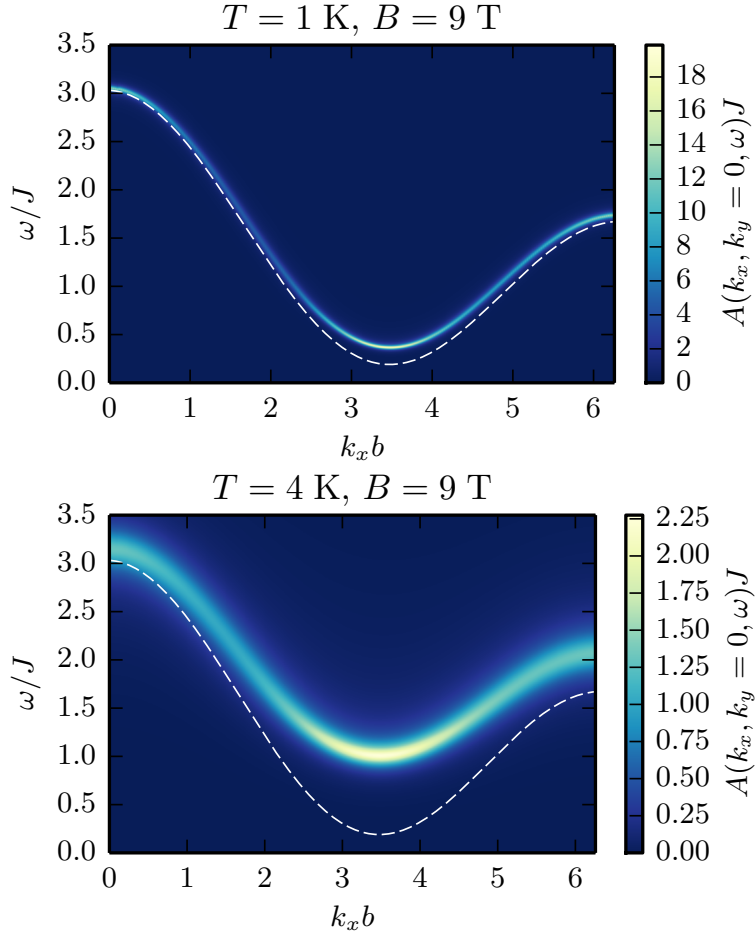


Figure 4.7: Contour plots of the spectral function $A(\mathbf{k}, \omega)$ of the hard-core bosons at $k_y = 0$ for temperatures of 1 K and 4 K in a magnetic field $B = 9 \text{ T}$ corresponding to an energy gap $\Delta = 0.19J$. The white dashed line is the bare excitation energy $\xi_{\mathbf{k}}$ given by Eq. (4.8).

where $S^{xy}(\mathbf{k}, \omega)$ and $S^{yx}(\mathbf{k}, \omega)$ do not vanish due to the broken inversion symmetry. The $U(1)$ symmetry due to the spin-rotational invariance with respect to the z axis requires that

$$S^{xz}(\mathbf{k}, \omega) = S^{zx}(\mathbf{k}, \omega) = S^{yz}(\mathbf{k}, \omega) = S^{zy}(\mathbf{k}, \omega) = 0. \quad (4.76)$$

The S^{zz} component of the spin dynamic structure factor cannot be simply expressed in terms of the spectral function because it is a two-particle Green function in terms of the hard-core boson operators,

$$S^{zz}(\mathbf{k}, \omega) = \frac{1}{N} \sum_{\mathbf{q}, \mathbf{q}'} \int_{-\infty}^{\infty} \frac{dt}{2\pi} e^{i\omega t} \left\langle b_{\mathbf{q}}^\dagger(t) b_{\mathbf{q}-\mathbf{k}}(t) b_{\mathbf{q}'}^\dagger(0) b_{\mathbf{q}'+\mathbf{k}}(0) \right\rangle. \quad (4.77)$$

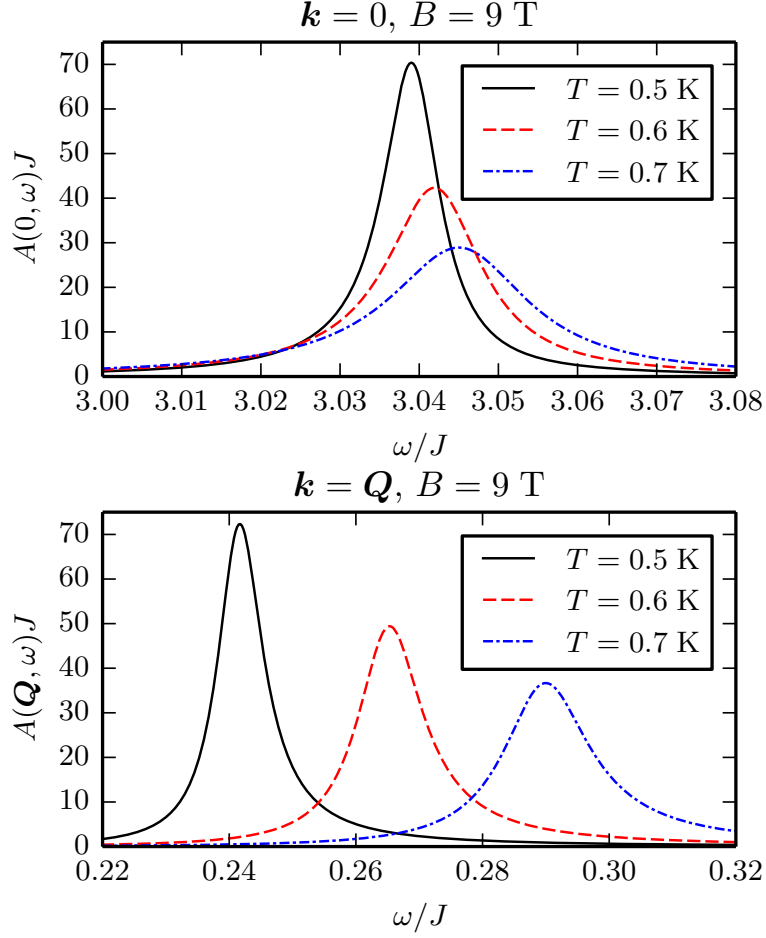


Figure 4.8: Spectral function $A(\mathbf{k}, \omega)$ at $\mathbf{k} = 0$ and at $\mathbf{k} = \mathbf{Q}$ (at the minimum of the dispersion) in a magnetic field $B = 9$ T corresponding to an energy gap $\Delta \approx 0.19J$.

4.5.2 Magnetic moment and magnetic susceptibility

The magnetic moment per site is given by

$$m = \langle S_i^z \rangle = \frac{1}{2} - n, \quad (4.78)$$

where n is the boson density per site which can be expressed in terms of the spectral function,

$$n = \frac{1}{N} \sum_{\mathbf{k}} n_{\mathbf{k}}, \quad (4.79)$$

with

$$n_{\mathbf{k}} = \langle b_{\mathbf{k}}^\dagger b_{\mathbf{k}} \rangle = \int_{-\infty}^{\infty} dx A(\mathbf{k}, x) n_B(x). \quad (4.80)$$

We define the magnetic susceptibility χ via

$$\chi = \frac{dm}{dB}. \quad (4.81)$$

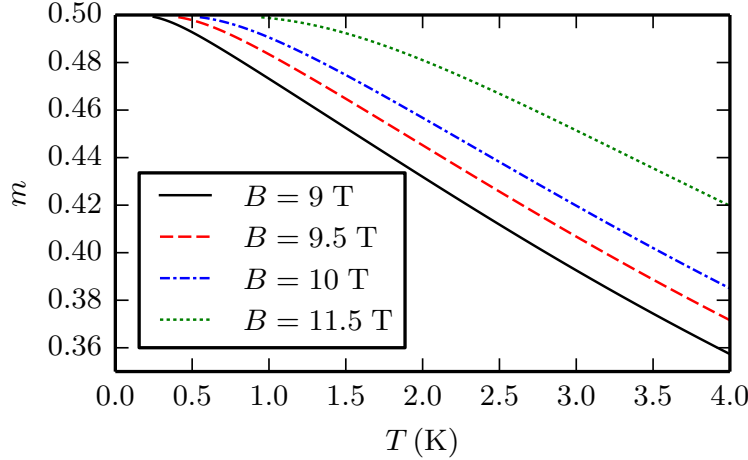


Figure 4.9: Numerical results for the magnetic moment m at different magnetic fields between 9 T and 11.5 T.

In the limit $T \rightarrow 0$ the boson density vanishes and the asymptotic low-temperature behavior of the susceptibility is therefore the one of free bosons because all interaction are frozen out,

$$\chi \propto T^{\frac{d-2}{2}} e^{-\Delta/T}, \quad (4.82)$$

where d is the dimensionality ($d = 2$ in our case) and Δ the energy gap.

The numerical results for magnetic moment and magnetic susceptibility for different magnetic fields above the saturation field are shown in Fig. 4.9 and Fig. 4.10, respectively. In Fig. 4.11, we compare our numerical results from the self-consistent ladder approximation with the low-temperature Hartree-Fock approximation without hard-core interaction and with a simple spin mean-field theory, which we describe in Appendix C. We see that for low temperatures $T \ll J$ the Hartree-Fock and the ladder approximation give essentially the same results. This allows us to use the Hartree-Fock approximation in the low-temperature regime where the self-consistent ladder approximation is difficult to implement due to the limited frequency resolution. At higher temperatures the hard-core interaction becomes important and the high-temperature behavior is approximately captured by the spin mean-field theory.

4.5.3 Internal energy and specific heat

The internal energy is given by

$$E = \langle \mathcal{H} \rangle = \sum_{\mathbf{k}} \tilde{\xi}_{\mathbf{k}} n_{\mathbf{k}} + E_{\text{MF}}, \quad (4.83)$$

where the infinite on-site interaction does not contribute because its expectation value is zero if the hard-core constraint is fulfilled. The specific heat

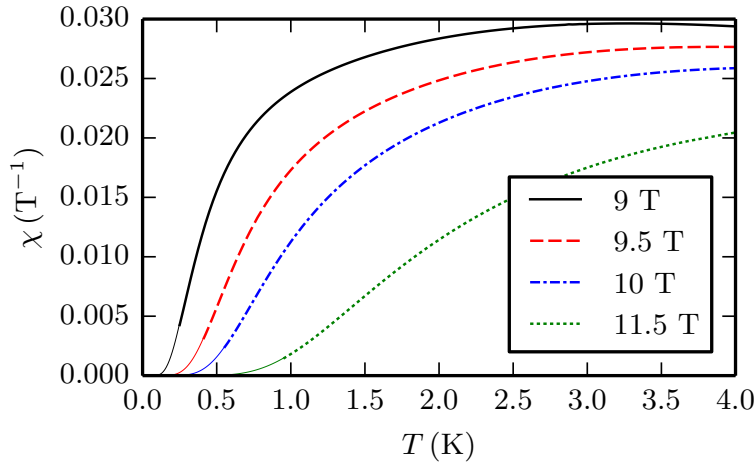


Figure 4.10: Numerical results for the magnetic susceptibility χ at different magnetic fields between 9 T and 11.5 T. The thin solid lines are low-temperature results from the Hartree-Fock approximation without hard-core interaction, which allows us to get results in the low-temperature regime where the self-consistent ladder approximation cannot be used due to the limited frequency resolution.

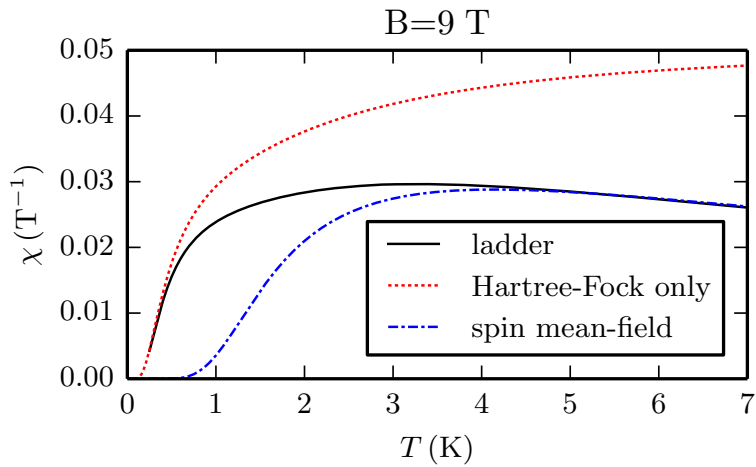


Figure 4.11: Comparison of the results for the magnetic susceptibility χ from the self-consistent ladder approximation, Hartree-Fock approximation without hard-core interaction, and spin mean-field theory for a magnetic field $B = 9 \text{ T}$ corresponding to an energy gap $\Delta \approx 0.19J$.

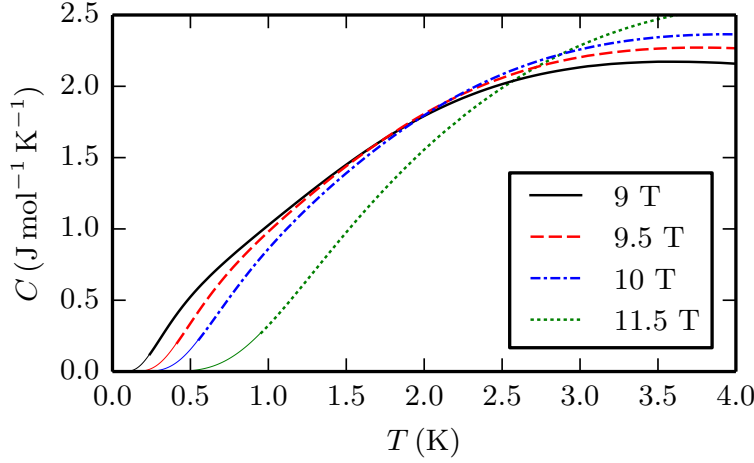


Figure 4.12: Numerical results for the specific heat C at different magnetic fields between 9 T and 11.5 T. The thin solid lines are low-temperature results from the Hartree-Fock approximation without hard-core interaction, which allows us to get results in the low-temperature regime where the self-consistent ladder approximation cannot be used due to the limited frequency resolution.

at constant volume is obtained by taking the temperature derivative of the internal energy,

$$C = \frac{dE}{dT}. \quad (4.84)$$

We note that E_{MF} depends on temperature and has to be taken into account for calculating the specific heat. The asymptotic low-temperature behavior of the specific heat is given by

$$C \propto T^{\frac{d-4}{2}} e^{-\Delta/T}. \quad (4.85)$$

The numerical results for the specific heat at different magnetic fields above the saturation field are shown in Fig. 4.12. In Fig. 4.13, we again compare our numerical results from the self-consistent ladder approximation with the low-temperature Hartree-Fock approximation without hard-core interaction and with a simple spin mean-field theory described in Appendix C. The magnetic contribution to the specific heat of Cs_2CuCl_4 has been measured experimentally [14, 15]. The more recent data published in Ref. [15] differ slightly from Ref. [14] for $B = 11.5$ T and are in better agreement with the expected size of the energy gap at that field strength. Therefore, in Fig. 4.14 we compare our results with the experimental data from Ref. [15], where we find that our theory captures the experimentally observed behavior both qualitatively and quantitatively. At low temperatures, the slope in the logarithmic plot of CT versus $1/T$ in Fig. 4.14 is given by $-\Delta$, which follows directly from Eq. (4.85).

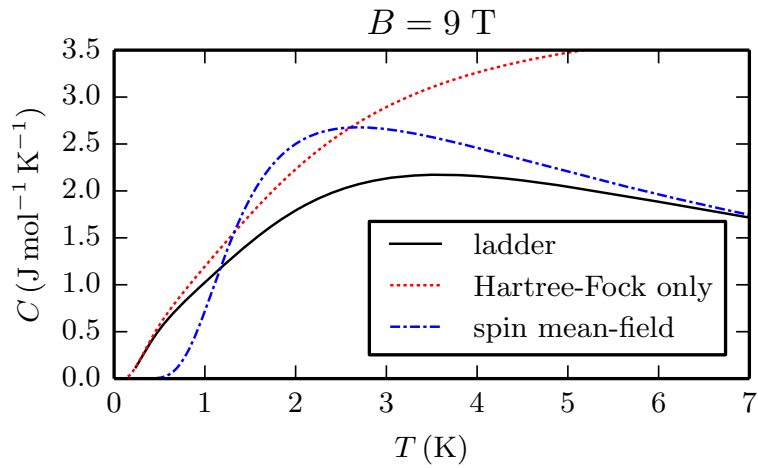


Figure 4.13: Comparison of the results for the specific heat C from the self-consistent ladder approximation, Hartree-Fock approximation without hard-core interaction, and spin mean-field theory for a magnetic field $B = 9$ T corresponding to an energy gap $\Delta \approx 0.19J$.

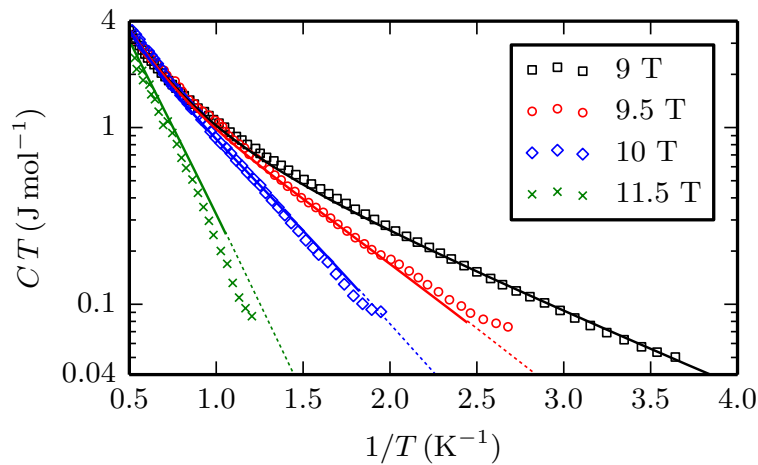


Figure 4.14: Comparison of our numerical results for the specific heat (solid lines) with experimental data from Ref. [15] (symbols) for different magnetic fields between 9 T and 11.5 T. The dashed lines are low-temperature results from the Hartree-Fock approximation without hard-core interaction, which allows us to get results in the low-temperature regime where the self-consistent ladder approximation cannot be used due to the limited frequency resolution.

4.6 Summary and conclusions

We have mapped the spin-1/2 Heisenberg model describing Cs_2CuCl_4 to a model of hard-core bosons where the hard-core constraint has been taken into account by an infinite on-site repulsion. Since we have only considered magnetic fields $B > B_c$ (along the a axis perpendicular to the lattice plane), we had to deal with gapped hard-core bosons. Due to the energy gap, the hard-core interaction can be taken into account using the self-consistent ladder approximation [48] and the remaining interactions can be treated within the self-consistent Hartree-Fock approximation. Before applying this method to Cs_2CuCl_4 , we have investigated for the exactly solvable one-dimensional XY model how the ladder approximation breaks down in the vicinity of the critical field B_c , finding that the ladder approximation for finite energy gaps Δ works well both at low and high temperatures and the deviations, maximal at $T \approx \Delta$, decrease with rising energy gap Δ . We have then calculated the spectral function of the hard-core bosons for Cs_2CuCl_4 from which we have obtained the magnetic susceptibility and the specific heat. The calculated specific heat is in good agreement with the available experimental data. We conclude that the self-consistent ladder approximation in combination with a self-consistent Hartree-Fock decoupling of the non-hard-core interactions gives an accurate description of the physical properties of gapped hard-core bosons in two dimensions at finite temperatures. An extension to three dimensions is straightforward and would only increase the numerical effort due to an increasing number of lattice sites. While in our work we started from a spin-1/2 model which we mapped to hard-core bosons, our theoretical approach is applicable whenever the elementary excitations can be described by gapped hard-core bosons; for example, in spin-dimer systems and systems of ultracold bosonic atoms (see Ref. [48] for more details and references for these examples).

Appendix A

Phonon energy and damping from the phonon self-energy

In this appendix, we show how we can obtain the renormalized phonon energy and the phonon damping from the analytic continuation of the self-energy $\Pi(q, i\bar{\omega})$ to real frequencies [27]. The phonon Green function $F(q, i\bar{\omega})$ and the corresponding self-energy $\Pi(q, i\bar{\omega})$ are defined by

$$F(q, i\bar{\omega}) = \frac{M}{\beta N} \langle X_Q X_{-Q} \rangle = \frac{1}{\bar{\omega}^2 + \omega_q^2 + \Pi(q, i\bar{\omega})}, \quad (\text{A.1})$$

where $Q = (q, i\bar{\omega})$ with bosonic Matsubara frequencies $\bar{\omega}$ and the phonon fields are defined as in Sec 3.4. The corresponding retarded Green function can then be obtained by analytical continuation to real frequencies [37],

$$F^R(q, \omega) = F(q, i\bar{\omega} \rightarrow \omega + i0^+) = \frac{1}{-\omega^2 + \omega_q^2 + \Pi^R(q, \omega)}, \quad (\text{A.2})$$

with the retarded self-energy $\Pi^R(q, \omega) = \Pi(q, \omega + i0^+)$. The renormalized phonon energy is determined by the complex poles of the retarded Green function [38]. This can be seen by Fourier transforming from frequency to time,

$$F^R(q, t) = \int_{-\infty}^{\infty} \frac{d\omega}{2\pi} e^{-i\omega t} F^R(q, \omega). \quad (\text{A.3})$$

This integral can be solved by the residue theorem considering the positions of the complex poles of $F^R(q, \omega)$ [38]. If the self-energy is small compared to ω_q^2 , the complex poles are at (see Fig. A.1)

$$\begin{aligned} \omega_{\pm} &\approx \pm \sqrt{\omega_q^2 + \Pi^R(q, \pm\omega_q)} \\ &\approx \pm\omega_q \pm \frac{\Pi^R(q, \pm\omega_q)}{2\omega_q}. \end{aligned} \quad (\text{A.4})$$

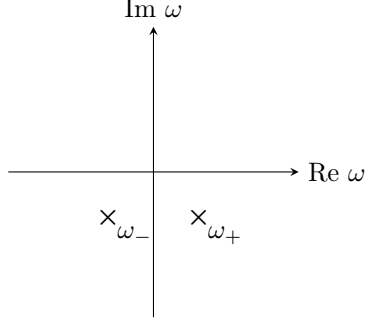


Figure A.1: Complex poles ω_{\pm} (indicated by crosses) of the retarded Green function $F^R(q, \omega)$ as given by Eq. (A.4).

The retarded Green function is then given by

$$\begin{aligned} F^R(q, t) &= -i\theta(t) \sum_{p=\pm} e^{-i\omega_p t} \text{Res} [F^R(q, \omega)]_{\omega=\omega_p} \\ &= \frac{i\theta(t)}{2} \left(\frac{1}{\omega_+} e^{-i\omega_+ t} + \frac{1}{\omega_-} e^{-i\omega_- t} \right) \\ &= \theta(t) \text{Im} \left(\frac{1}{\tilde{\omega}_q + i\gamma_q} e^{i\tilde{\omega}_q t} \right) e^{-\gamma_q t}, \end{aligned} \quad (\text{A.5})$$

where we have defined

$$\tilde{\omega}_q = \omega_q + \frac{\text{Re} \Pi^R(q, \omega_q)}{2\omega_q}, \quad \gamma_q = -\frac{\text{Im} \Pi^R(q, \omega_q)}{2\omega_q}, \quad (\text{A.6})$$

and used

$$\text{Re } \omega_+ = -\text{Re } \omega_-, \quad \text{Im } \omega_+ = \text{Im } \omega_-, \quad (\text{A.7})$$

which follows from the following analytical property of the retarded phonon self-energy (with inversion symmetry assumed),

$$\Pi^R(q, -\omega) = [\Pi^R(q, \omega)]^*. \quad (\text{A.8})$$

From Eq. (A.5) it is now obvious that $\tilde{\omega}_q$ can be identified as the renormalized phonon energy and γ_q as the phonon damping.

Appendix B

Numerical details

In this appendix, we give more details on the numerical solution of the self-consistency equations for the spectral function $A(\mathbf{k}, \omega)$ of the hard-core bosons given in Chapter 4 and we show how we discretize the Brillouin zone for these calculations.

B.1 Calculation of the spectral function

To find a self-consistent solution for the spectral function $A(\mathbf{k}, \omega)$, we have to start from an initial spectral function $A_{\text{init}}(\mathbf{k}, \omega)$. If we would just have the standard non-self-consistent ladder approximation, we would replace $A(\mathbf{k}, \omega)$ by the non-interacting spectral function $A_0(\mathbf{k}, \omega)$ and then directly calculate the spectral function $A(\mathbf{k}, \omega)$. It is therefore sensible to use the non-interacting spectral function as the initial spectral function, which is given by

$$A_0(\mathbf{k}, \omega) = -\frac{1}{\pi} \text{Im}G_0(\mathbf{k}, \omega + i0^+) = \delta(\omega - \xi_{\mathbf{k}}). \quad (\text{B.1})$$

We note here that at $T = 0$ the spectral function is not affected by interactions, $A(\mathbf{k}, \omega) = A_0(\mathbf{k}, \omega)$, because the ground state is the vacuum without any bosons due to the energy gap. For the numerical calculation, we replace the delta function by a box function of finite width η (e.g., $\eta = 0.1 J$) centered at $\omega = \xi_{\mathbf{k}}$. This is fine as long as $\xi_{\mathbf{k}} > 0$ which is the case for magnetic fields $B > B_c$. For $\xi_{\mathbf{k}} \leq 0$, we have to take the sign of the spectral function into account [37],

$$\text{sgn}[A(\mathbf{k}, \omega)] = \text{sgn } \omega. \quad (\text{B.2})$$

Therefore, a positive delta peak is not permitted for negative frequencies and the non-interacting spectral function cannot be used for values of \mathbf{k} with $\xi_{\mathbf{k}} \leq 0$. In our calculations, we instead place a step function at a small positive frequency when $\xi_{\mathbf{k}} \leq 0$. This allows us to find a self-consistent solution even for $B \leq B_c$.

Having chosen an initial spectral function, the next step is to calculate $\rho(\mathbf{p}, \omega)$ via Eq. (4.49), which is a multi-dimensional convolution that can be

calculated with the fast Fourier transform method, e.g., using the FFTW library [85]. Then $f(\mathbf{p}, \omega)$ can be obtained from Eq. (4.53), where the principal value integral can also be evaluated as a convolution [86]. Next, the calculation of $\rho_\Sigma(\mathbf{k}, \omega)$ via Eq. (4.61c) and $\text{Re}\Sigma^R(\mathbf{k}, \omega)$ via Eq. (4.61a) also involves convolutions. While the values of \mathbf{k} are naturally discretized for a finite lattice, as discussed in Appendix B.2, the real frequencies ω have to be artificially discretized, leading to a limited frequency resolution, and a frequency cutoff has to be introduced (e.g., $|\omega| < 20 J$). When using the fast Fourier transform method to evaluate the convolutions, this treats the functions as periodic both in momentum and frequency space, leading to a wrap-around effect in the frequency dependence of the calculated functions. This wrap-around error can be dealt with by setting the spectral function $A(\mathbf{k}, \omega)$ to zero for frequencies larger than a certain cutoff (e.g., for $|\omega| > 10 J$). In our calculations, we typically used lattice sizes up to 4096 sites and up to 131 072 frequency points.

To achieve convergence, a simple mixing update procedure has to be used, where the updated spectral function and Hartree-Fock parameters are set to be a mixture of the previous iteration and the new values from the self-consistency equations. In our case, a mixing of 50% worked well. We note that in the case without the self-consistent Hartree-Fock decoupling (e.g., for an XY model), mixing is not necessary to achieve convergence. The converged numerical result should (up to a small numerical error) fulfill the sum rule [48]

$$\int_{-\infty}^{\infty} d\omega A(\mathbf{k}, \omega) = 1 - 2n. \quad (\text{B.3})$$

B.2 Brillouin zone discretization

The use of fast Fourier transform methods is based on the periodicity of the transformed functions. Therefore, the Brillouin zone should not be arbitrarily discretized because that would in most cases destroy the periodicity. Still, there is an infinite number of possible parameterizations of the Brillouin zone. In our work, we have used two parameterizations which we will present here. The first parameterization starts from the lattice basis

$$\mathbf{a}_1 = b\hat{\mathbf{x}}, \quad \mathbf{a}_2 = -\frac{b}{2}\hat{\mathbf{x}} + \frac{c}{2}\hat{\mathbf{y}}, \quad (\text{B.4})$$

with the corresponding reciprocal basis

$$\mathbf{b}_1 = \frac{2\pi}{b}\hat{\mathbf{x}} + \frac{2\pi}{c}\hat{\mathbf{y}}, \quad \mathbf{b}_2 = \frac{4\pi}{c}\hat{\mathbf{y}}. \quad (\text{B.5})$$

The lattice momentum vectors can then be expanded in terms of the reciprocal basis,

$$\mathbf{k} = k_1\mathbf{b}_1 + k_2\mathbf{b}_2, \quad (\text{B.6})$$

where the periodic boundary conditions dictate that

$$k_1 = \frac{l_1}{N_1}, \quad l_1 \in \{0, \dots, N_1 - 1\}, \quad (\text{B.7a})$$

$$k_2 = \frac{l_2}{N_2}, \quad l_2 \in \{0, \dots, N_2 - 1\}. \quad (\text{B.7b})$$

The total number of lattice sites is $N = N_1 N_2$. To obtain a uniform mesh [87], we have to choose

$$N_2 = 2N_1. \quad (\text{B.8})$$

The second (primed) parameterization starts from the lattice basis

$$\mathbf{a}'_1 = \frac{b}{2}\hat{\mathbf{x}} - \frac{c}{2}\hat{\mathbf{y}}, \quad \mathbf{a}'_2 = \frac{b}{2}\hat{\mathbf{x}} + \frac{c}{2}\hat{\mathbf{y}}, \quad (\text{B.9})$$

with the corresponding reciprocal basis

$$\mathbf{b}'_1 = \frac{2\pi}{b}\hat{\mathbf{x}} - \frac{2\pi}{c}\hat{\mathbf{y}}, \quad \mathbf{b}'_2 = \frac{2\pi}{b}\hat{\mathbf{x}} + \frac{2\pi}{c}\hat{\mathbf{y}}. \quad (\text{B.10})$$

The lattice momentum vectors can again be expanded in terms of the reciprocal basis,

$$\mathbf{k} = k'_1 \mathbf{b}'_1 + k'_2 \mathbf{b}'_2, \quad (\text{B.11})$$

where the periodic boundary conditions dictate that

$$k'_1 = \frac{l'_1}{N'_1}, \quad l'_1 \in \{0, \dots, N'_1 - 1\}, \quad (\text{B.12a})$$

$$k'_2 = \frac{l'_2}{N'_2}, \quad l'_2 \in \{0, \dots, N'_2 - 1\}. \quad (\text{B.12b})$$

The total number of lattice sites is $N = N'_1 N'_2$. To obtain a uniform mesh [87], we have to choose

$$N'_2 = N'_1. \quad (\text{B.13})$$

Appendix C

Spin mean-field approximation

We expect that at high temperatures $T \gg J$, the spins decouple and it is sufficient to describe the spin-spin interactions on a mean-field level where the effects of the interactions are approximated by an effective magnetic field. To derive this mean-field description, we start from the Hamiltonian (1.1),

$$\mathcal{H} = \frac{1}{2} \sum_{ij} [J_{ij} \mathbf{S}_i \cdot \mathbf{S}_j + \mathbf{D}_{ij} \cdot (\mathbf{S}_i \times \mathbf{S}_j)] - h \sum_i S_i^z. \quad (\text{C.1})$$

First, we note that only the z -component of the expectation values of the spin operators does not vanish,

$$\langle \mathbf{S}_i \rangle = m \hat{\mathbf{z}}, \quad m = \langle S_i^z \rangle. \quad (\text{C.2})$$

Expanding up to linear order in fluctuations from this expectation value, we find

$$\mathcal{H} \approx -N J_0 \frac{m^2}{2} - h_{\text{eff}} \sum_i S_i^z, \quad (\text{C.3})$$

where the effective magnetic field is given by

$$h_{\text{eff}} = h - J_0 m, \quad (\text{C.4})$$

with

$$J_0 = 2J + 4J'. \quad (\text{C.5})$$

The magnetic moment m is obtained by solving the self-consistency equation

$$m = \frac{1}{2} \tanh \left(\frac{\beta}{2} h_{\text{eff}} \right), \quad (\text{C.6})$$

and the energy in this mean-field approximation is a simple function of magnetic field and magnetic moment,

$$E = N \left(\frac{1}{2} J_0 m^2 - mh \right). \quad (\text{C.7})$$

Results from this approximation are used in Chapter 4, where we compare the self-consistent ladder approximation with this spin mean-field approximation to evaluate the high-temperature behavior.

Appendix D

Deutsche Zusammenfassung

In dieser Arbeit beschäftigen wir uns mit einer theoretischen Beschreibung von Cs_2CuCl_4 und wir beginnen deshalb in Kapitel 1 mit einer Diskussion der für uns relevanten Eigenschaften dieses Materials. Cs_2CuCl_4 ist ein antiferromagnetischer Isolator mit einer orthorhombischen Kristallstruktur. Die Cu^{2+} Ionen haben einen Spin von $1/2$ und formen in den bc -Ebenen ein Dreiecksgitter (siehe Abb. D.1). Die Elektronen, die den Spin- $1/2$ tragen, sind aufgrund der starken Coulomb-Wechselwirkung auf den Cu^{2+} Gitterplätzen lokalisiert. Das bedeutet, dass Cs_2CuCl_4 ein Mott-Isolator ist, wobei die Spins über Austauschkopplungen miteinander wechselwirken. Innerhalb der letzten beiden Jahrzehnte sind verschiedene interessante physikalischen Eigenschaften von Cs_2CuCl_4 ausführlich untersucht worden, wie z.B. Spinflüssigkeitsverhalten mit Spinon-Anregungen [P2, 1–12], Bose-Einstein-Kondensation von Magnonen am quantenkritischen Punkt [13–17] und das komplexe Phasendiagramm bei Magnetfeldern innerhalb der bc -Ebene [2, 18–23].

Das magnetische Verhalten von Cs_2CuCl_4 kann mit Hilfe des folgenden zweidimensionalen Spin- $1/2$ -Heisenberg-Modells beschrieben werden (mit Magnetfeld entlang der kristallographischen a -Achse) [13],

$$\mathcal{H} = \frac{1}{2} \sum_{ij} [J_{ij} \mathbf{S}_i \cdot \mathbf{S}_j + \mathbf{D}_{ij} \cdot (\mathbf{S}_i \times \mathbf{S}_j)] - h \sum_i S_i^z, \quad (\text{D.1})$$

wobei die Summen über N Gitterplätze laufen und $h = g\mu_B B$ die Zeeman-Energie ist mit dem effektiven g -Faktor $g = 2.19(1)$. Die Spin- $1/2$ -Operatoren $\mathbf{S}_i = \mathbf{S}(\mathbf{R}_i)$ befinden sich auf den Gitterplätzen \mathbf{R}_i eines anisotropen Dreiecks-gitters mit Gitterkonstanten b und c (siehe Abb. D.1). Die Austauschkopplungen $J_{ij} = J(\mathbf{R}_i - \mathbf{R}_j)$ verbinden benachbarte Spins entlang der kristallographischen b -Achse ($J_{ij} = J$) und entlang der Diagonalen ($J_{ij} = J'$). Aufgrund der gebrochenen Inversionssymmetrie in Cs_2CuCl_4 gibt es auch Dzyaloshinskii-Moriya-Wechselwirkungen $\mathbf{D}_{ij} = D_{ij}\hat{\mathbf{z}}$, die benachbarte Spins entlang der Diagonalen verbinden ($D_{ij} = \pm D$), wie in Abb. D.1 gezeigt. Die genaue Form des Hamiltonians (D.1) und die Werte der Wechselwirkungskonstanten sind mit inelastischen Neutronenstreuungsexperimenten in Magnetfeldern

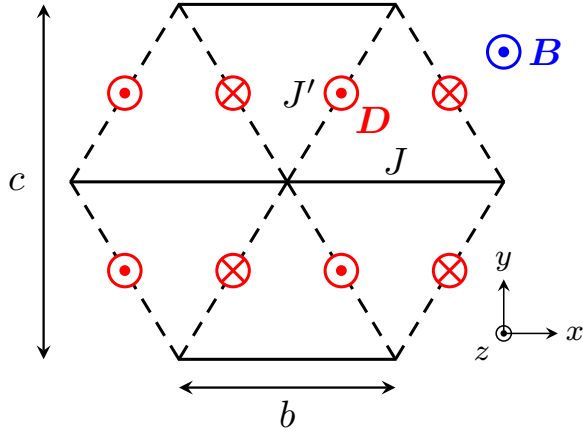


Abbildung D.1: Ausschnitt des anisotropen Dreiecksgitters, das von den Spins in Cs_2CuCl_4 gebildet wird. Die stärkste Austauschkopplung J verbindet die Spins nächster Nachbarn entlang der kristallographischen b -Achse, während die schwächere Austauschkopplung J' Spins entlang der Diagonalen verbindet. Es gibt zudem noch schwache Dzyaloshinskii-Moriya-Wechselwirkungen $\mathbf{D} = \pm D\hat{\mathbf{z}}$, die benachbarte Spins entlang der Diagonalen verbinden. Die Richtung von \mathbf{D} ist angegeben durch \odot für $+\hat{\mathbf{z}}$ und \otimes für $-\hat{\mathbf{z}}$. Wir betrachten nur den Fall eines Magnetfeldes \mathbf{B} entlang der a -Achse, die senkrecht zur Gitterebene steht.

oberhalb des Sättigungsfeldes $B_c = 8.44(1)$ T gemessen worden. Die etablierten Werte sind [13]: $J = 0.374(5)$ meV = 4.34(6) K, $J'/J = 0.34(3)$ und $D/J = 0.053(5)$. Es gibt auch eine schwache Kopplung von Spins benachbarter Ebenen, $J''/J = 0.045(5)$, die wir aber vernachlässigen, da diese Kopplung nur für sehr niedrige Temperaturen $T \lesssim 0.1$ K und in der antiferromagnetisch geordneten Phase in Magnetfeldern $B < B_c$ relevant ist und wir diese Bereiche in dieser Arbeit nicht untersuchen werden.

Das Phasendiagramm für Cs_2CuCl_4 als Funktion der Temperatur T und eines externen Magnetfeldes $B\hat{\mathbf{z}}$ senkrecht zur bc -Ebene ist in Abb. D.2 schematisch dargestellt [1]. Genau genommen gibt es nur zwei Phasen: eine paramagnetische Phase mit Spinrotationsinvarianz bezüglich der z -Achse und eine antiferromagnetisch geordnete Phase (bezeichnet als *3D AFM LRO*), in der diese Spinrotationsinvarianz spontan gebrochen ist. Die beiden anderen in Abb. D.2 dargestellten Phasen sind Teil der paramagnetischen Phase, die wir in drei Bereiche unterteilen: eine Spinflüssigkeitsphase mit starken kurzreichweiten Spinkorrelationen, eine ferromagnetische Phase mit fast komplett polarisierten Spins und ein paramagnetischer Bereich. Die gestrichelten Linien in Abb. D.2, die diese Phasen unterteilen, sind daher keine Phasenübergänge, sondern geben den Übergang von einem Bereich in den anderen an (ein sogenannter Crossover).

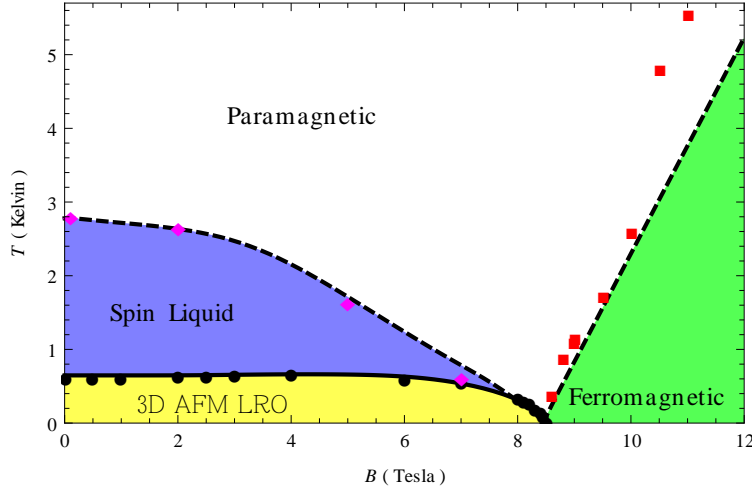


Abbildung D.2: Schematisches Phasendiagramm von Cs_2CuCl_4 (Nachzeichnung von Fig. 1 in Ref. [1]) als Funktion der Temperatur T und des externen Magnetfeldes $B\hat{z}$ entlang der kristallographischen a -Achse. Die experimentellen Datenpunkte für den Übergang von der paramagnetischen zur ferromagnetischen Phase (Quadrate) und für den Phasenübergang von der geordneten zur Spinflüssigkeitsphase (schwarze Kreise) stammen aus Ref. [14], wohingegen die Datenpunkte für den Übergang von der Spinflüssigkeitsphase zur paramagnetischen Phase (Rauten) aus Ref. [35] stammen.

Die Spin-1/2-Operatoren in Gl. (D.1) erfüllen die Kommutationsrelationen

$$[S_i^+, S_j^-] = 2\delta_{ij}S_i^z, \quad [S_i^\pm, S_j^z] = \mp\delta_{ij}S_i^\pm, \quad (\text{D.2})$$

wobei $S_i^\pm = S_i^x \pm iS_i^y$ und $S_i^2 = 3/4$. Diese Kommutationsrelationen sind komplizierter als die einfachen (Anti-)Kommutationsrelationen von Fermionen und Bosonen,

$$[b_i, b_j^\dagger] = \delta_{ij}, \quad [b_i^\dagger, b_j^\dagger] = [b_i, b_j] = 0, \quad (\text{D.3a})$$

$$\{c_i, c_j^\dagger\} = \delta_{ij}, \quad \{c_i^\dagger, c_j^\dagger\} = \{c_i, c_j\} = 0, \quad (\text{D.3b})$$

wobei b_i^\dagger und b_i bosonische und c_i^\dagger und c_i fermionische Erzeugungs- und Vernichtungsoperatoren sind und $\{c_i, c_j^\dagger\} = c_i c_j^\dagger + c_j^\dagger c_i$ der Antikommutator ist. Der Vorteil von bosonischen und fermionischen Operatoren ist, dass das Wicksche Theorem für diese Operatoren existiert und damit die Methoden der Greenschen Funktionen und Feynmandiagrammen verwendet werden können [37, 38]. Deshalb ist es in vielen Fällen sinnvoll die Spinoperatoren durch bosonische oder fermionische Operatoren darzustellen [39]. In Kapitel 1 dieser Arbeit werden deshalb einige mögliche Repräsentationen der Spinoperatoren diskutiert. Zudem erläutern wir die Hartree-Fock-Näherungen und diagrammatischen Methoden, die wir zur Behandlung der Wechselwirkungen verwenden.

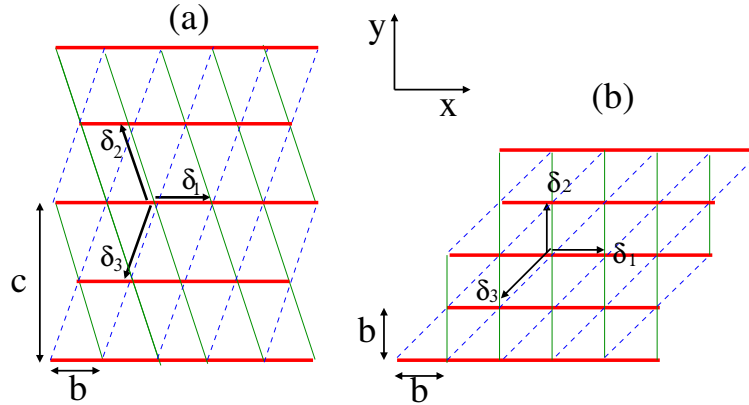


Abbildung D.3: (a) Anisotropes Dreiecksgitter mit Austauschkopplungen J_1 (fette Linien), J_2 (dünne Linien) und J_3 (dünne gestrichelte Linien) zwischen nächsten Nachbarn; die zugehörigen Verbindungsvektoren sind $\delta_1 = b\hat{x}$, $\delta_2 = -\frac{b}{2}\hat{x} + \frac{c}{2}\hat{y}$ und $\delta_3 = -\frac{b}{2}\hat{x} - \frac{c}{2}\hat{y}$. Für Cs_2CuCl_4 , setzen wir $J_1 = J = 4.34$ K und $J_2 = J_3 = J' = 1.49$ K; die Gitterstruktur ist orthorhombisch mit Gitterkonstanten $b = 7.48$ Å und $c = 12.26$ Å innerhalb einer Gitterebene; die kristallographische a -Achse steht senkrecht zu den Gitterebenen. (b) Topologisch äquivalentes Quadratgitter mit diagonalen Verbindungen.

In Kapitel 2 verwenden wir die Majorana-Fermion-Darstellung der Spin-1/2-Operatoren, um die Spinflüssigkeitsphase zu untersuchen. Dabei finden wir, dass die elementaren Anregungen quasi-eindimensional sind, was uns in Kapitel 3 ermöglicht die Ultraschalleigenschaften in der Spinflüssigkeitsphase mit Hilfe eines eindimensionalen Modells zu untersuchen, wobei wir die Spinoperatoren mit der Jordan-Wigner-Transformation durch spinlose Fermionen darstellen. In Kapitel 4 betrachten wir dann schließlich die thermodynamischen Eigenschaften von Cs_2CuCl_4 in Magnetfeldern oberhalb des Saturierungsfeldes von $B_c \approx 8.5$ T und verwenden dazu die Hardcore-Boson-Darstellung für die Spinoperatoren. Die Methoden die wir in dieser Arbeit entwickeln sind dabei nicht auf Cs_2CuCl_4 beschränkt, sondern können auch auf andere Materialien angewendet werden, die durch ein Spin-1/2-Heisenberg-Modell auf einem Dreiecksgitter beschrieben werden können. Ein wichtiges Beispiel ist die Materialklasse $\text{Cs}_2\text{Cu}(\text{Cl}_{4-x}\text{Br}_x)$, bei der Chlor teilweise durch Brom substituiert wird, wodurch die Stärke der Austauschkopplungen und das Verhältnis J'/J variiert werden können [28–31].

D.1 Majorana-Spinflüssigkeit und dimensionale Reduktion

In Kapitel 2 untersuchen wir die Spinflüssigkeitsphase von Cs_2CuCl_4 in dem Regime, in dem das externe Magnetfeld nicht zu dicht beim kritischen Feld $B_c \approx 8.5$ T liegt. Da in diesem Teil des Phasendiagramms die Temperatur groß

ist im Vergleich zur Kopplung J'' zwischen den Ebenen und zur Dzyaloshinskii-Moriya-Wechselwirkung D , können wir diese Wechselwirkungen vernachlässigen. Es ist deshalb vernünftig die Spinflüssigkeitsphase von Cs_2CuCl_4 mit einem zweidimensionalen Heisenberg-Modell auf einem Dreiecksgitter zu beschreiben,

$$\mathcal{H} = \frac{1}{2} \sum_{ij} J_{ij} \mathbf{S}_i \cdot \mathbf{S}_j - h \sum_i S_i^z, \quad (\text{D.4})$$

wobei die Spin-1/2-Operatoren $\mathbf{S}_i = \mathbf{S}_{\mathbf{R}_i}$ auf den Gitterplätzen \mathbf{R}_i eines Dreiecksgitters liegen und die Austauschkopplungen $J_{ij} = J(\mathbf{R}_i - \mathbf{R}_j)$ nur dann ungleich Null sind, wenn $\mathbf{R}_i - \mathbf{R}_j$ benachbarte Gitterpunkte verbinden. Wir nehmen zuerst verschiedene Austauschkopplungen $J_\mu = J(\pm \delta_\mu)$ für jede der drei in Abb. D.3 gezeigten Richtungen $\boldsymbol{\delta}_1$, $\boldsymbol{\delta}_2$ und $\boldsymbol{\delta}_3$ an, wobei $\mu = 1, 2, 3$ die jeweilige Richtung kennzeichnet. Später setzen wir dann $J_1 = J = 4.34$ K und $J_2 = J_3 = J' = 1.49$ K, um Cs_2CuCl_4 zu beschreiben.

Da für Cs_2CuCl_4 das Verhältnis $J'/J \approx 1/3$ nicht sehr klein ist, erscheint es zuerst vernünftig, eine zweidimensionale Spinflüssigkeitsphase zu erwarten. Jedoch ist eine Theorie, in der die elementaren Anregungen der Spinflüssigkeit die eindimensionalen fermionischen Spinonen der Heisenberg-Kette sind, sehr erfolgreich gewesen [6, 7, 65]. Dies suggeriert, dass es in der Spinflüssigkeitsphase von Cs_2CuCl_4 elementare Anregungen gibt, die nur entlang der Richtung $\boldsymbol{\delta}_1$ der stärksten Austauschkopplung propagieren können. In einem einfachen Bild entsteht diese dimensionale Reduktion in Cs_2CuCl_4 durch eine frustrationsinduzierte Reduktion der effektiven Kopplung J' der schwächeren Bindungen [9].

In einem Kernspinresonanz-Experiment [11] mit Cs_2CuCl_4 wurden Hinweise darauf gefunden, dass in der Spinflüssigkeitsphase die elementaren Anregungen Fermionen ohne Anregungslücke sind. Um diese Phase zu beschreiben, sollte man daher die Spinoperatoren des zugrunde liegenden Heisenberg-Modells durch fermionische Freiheitsgrade ausdrücken. Hier verwenden wir deshalb eine Darstellung der Spinoperatoren durch Majorana-Fermionen, indem wir für jeden Gitterplatz \mathbf{R}_i drei Majorana-Fermionen η_i^x , η_i^y , und η_i^z einführen, die die folgende Antikommurationsrelationen erfüllen,

$$\left\{ \eta_i^\alpha, \eta_j^\beta \right\} = \delta_{ij} \delta^{\alpha\beta}. \quad (\text{D.5})$$

Die Spinalgebra kann dann durch die folgende Darstellung der Spinoperatoren reproduziert werden [49],

$$S_i^x = -i\eta_i^y \eta_i^z, \quad S_i^y = -i\eta_i^z \eta_i^x, \quad S_i^z = -i\eta_i^x \eta_i^y. \quad (\text{D.6})$$

Diese Majorana-Darstellung ist zuvor von mehreren Autoren verwendet worden, um Quantenspinsysteme zu untersuchen [50–56]. Zudem kann ein Pfadintegral auf Basis von kohärenten Zuständen für Majorana-Fermionen konstruiert werden [56], so dass die bekannten feldtheoretischen Methoden verwendet

werden können, um das zugrunde liegende Spinmodell zu untersuchen. Ein Vorteil der Majorana-Darstellung ist, dass keine unphysikalischen Zustände eingeführt werden müssen. Aber für ein System einer geraden Zahl N von Spins hat der Majorana-Hilbertraum $2^{3N/2}$ Zustände und besteht aus $2^{N/2}$ identischen Kopien des 2^N -dimensionalen Spin-Hilbertraums [55]. Für unsere Meanfield-Rechnung ignorieren wir einfach diese Redundanz.

Zuerst betrachten wir den Fall ohne externes Magnetfeld, so dass unser Hamiltonian eine Spinrotationsinvarianz hat. Für den Spinflüssigkeitszustand verlangen wir, dass unsere Meanfield-Entkopplung weder die Spinrotations- noch die Gittertranslationsinvarianz bricht. Für einen Antiferromagneten auf einem isotropen Dreiecksgitter wurde eine solche Majorana-Meanfield-Theorie vor kurzem von Biswas *et al.* [55] entwickelt. Dieser Arbeit folgend führen wir die Majorana-Bindungsoperatoren ein,

$$C_{ij}^\alpha = \eta_i^\alpha \eta_j^\alpha, \quad (\text{D.7})$$

um den Heisenberg-Hamiltonian (D.4) ohne Magnetfeld zu schreiben als

$$\mathcal{H} = \frac{1}{4} \sum_{ij} \sum_{\alpha \neq \beta} J_{ij} C_{ij}^\alpha C_{ij}^\beta. \quad (\text{D.8})$$

Wir führen nun eine einfache Meanfield-Entkopplung durch,

$$C_{ij}^\alpha C_{ij}^\beta \rightarrow C_{ij}^\alpha \langle C_{ij}^\beta \rangle + \langle C_{ij}^\alpha \rangle C_{ij}^\beta - \langle C_{ij}^\alpha \rangle \langle C_{ij}^\beta \rangle, \quad (\text{D.9})$$

und aufgrund der geforderten Spinrotationsinvarianz folgt, dass die Erwartungswerte

$$\langle C_{ij}^\alpha \rangle = \langle \eta_i^\alpha \eta_j^\alpha \rangle \equiv i Z_{ij} \quad (\text{D.10})$$

unabhängig sind vom Index α . Wir erhalten damit den Meanfield-Hamiltonian

$$\mathcal{H}_{\text{MF}} = i \sum_{ij\alpha} t_{ij} \eta_i^\alpha \eta_j^\alpha + U_0, \quad (\text{D.11})$$

mit Hüpfenergien

$$t_{ij} = J_{ij} Z_{ij} = -t_{ji}. \quad (\text{D.12})$$

Aufgrund der geforderten Translationsinvarianz folgt zudem

$$Z_{\mathbf{R}_i, \mathbf{R}_i \pm \boldsymbol{\delta}_\mu} = \pm Z_\mu. \quad (\text{D.13})$$

Via der Fourier-Transformation

$$\eta_{\mathbf{R}_i}^\alpha = \frac{1}{\sqrt{N}} \sum_{\mathbf{k}} e^{i \mathbf{k} \cdot \mathbf{R}_i} \eta_{\mathbf{k}}^\alpha \quad (\text{D.14})$$

kann unser Meanfield-Hamiltonian (D.11) geschrieben werden als

$$\mathcal{H}_{\text{MF}} = \frac{1}{2} \sum_{\mathbf{k}, \alpha} \varepsilon_{\mathbf{k}} \eta_{-\mathbf{k}}^\alpha \eta_{\mathbf{k}}^\alpha + U_0, \quad (\text{D.15})$$

mit Meanfield-Energiedispersion

$$\varepsilon_{\mathbf{k}} = -4 \sum_{\mu=1}^3 J_{\mu} Z_{\mu} \sin(\mathbf{k} \cdot \boldsymbol{\delta}_{\mu}), \quad (\text{D.16})$$

und Wechselwirkungsenergie

$$U_0 = 3N \sum_{\mu=1}^3 J_{\mu} Z_{\mu}^2. \quad (\text{D.17})$$

Bei endlicher Temperatur ist die freie Energie dann

$$F = -\frac{3}{2\beta} \sum_{\mathbf{k}} \ln(1 + e^{-\beta\varepsilon_{\mathbf{k}}}) + U_0, \quad (\text{D.18})$$

was zu den folgenden Selbstkonsistenzgleichungen führt,

$$Z_{\mu} = \frac{1}{N} \sum_{\mathbf{k}} f(\varepsilon_{\mathbf{k}}) \sin(\mathbf{k} \cdot \boldsymbol{\delta}_{\mu}), \quad \mu = 1, 2, 3. \quad (\text{D.19})$$

Hier bezeichnet $f(\varepsilon_{\mathbf{k}}) = 1/(e^{\beta\varepsilon_{\mathbf{k}}} + 1)$ die Fermi-Funktion. Durch Lösen dieser Selbstkonsistenzgleichungen finden wir, dass oberhalb einer kritischen Temperatur $T_c = J/2$ alle $Z_{\mu} = 0$ sind. Unterhalb der kritischen Temperatur $T_c = J/2$ wird ein eindimensionaler Zustand realisiert, in dem der Erwartungswert Z_{μ} entlang der Richtung der stärksten Austauschkopplung endlich wird und für die restlichen Erwartungswerte weiterhin $Z_{\nu \neq \mu} = 0$ gilt. Damit können die Majorana-Fermionen nur in eine Richtung propagieren.

Für Cs_2CuCl_4 mit $J_1 = J$ und $J_2 = J_3 = J' \approx J/3$ bedeutet das, dass die Majorana-Fermionen nur entlang der kristallographischen b -Achse (die x -Achse in unserer Notation) propagieren können. Mit $J = 4.34$ K, erhalten wir, dass ohne externes Magnetfeld der Übergang zur Spinflüssigkeitsphase in Cs_2CuCl_4 bei $T_c = J/2 = 2.17$ K stattfinden sollte. Mit einer einfachen Rechnung lässt sich zeigen, dass bei dieser Temperatur die spezifische Wärme C ein Maximum haben sollte, wie in Abb. D.4 gezeigt. In der experimentellen Arbeit von Radu *et al.* [14] wird in der Tat die Übergangstemperatur zur Spinflüssigkeitsphase mit der Temperatur identifiziert, bei der die spezifische Wärme ein Maximum hat, was zu $T_c \approx 2.1$ K führt und sehr gut mit unserer theoretischen Vorhersage übereinstimmt. Eine alternative Abschätzung von T_c durch Coldea *et al.* [1] identifiziert die Übergangstemperatur zur Spinflüssigkeitsphase mit der Temperatur, bei der die Spinsuszeptibilität ein Maximum aufweist, was zu der Abschätzung $T_c \approx 2.65$ K [69] bzw. $T_c \approx 2.8$ K [19] führt. Eine weitere alternative Abschätzung der Übergangstemperatur durch Vacchon *et al.* [11] beruht auf Kernspinresonanz-Messungen und führt zu $T_c \approx 2.5$ K.

Wenn sich Cs_2CuCl_4 in einem Magnetfeld entlang der kristallographischen a -Achse befindet, dann wird die kritische Temperatur für Spinflüssigkeitsverhalten reduziert, wie in Abb. D.2 zu sehen ist. Aufgrund des Magnetfeldes

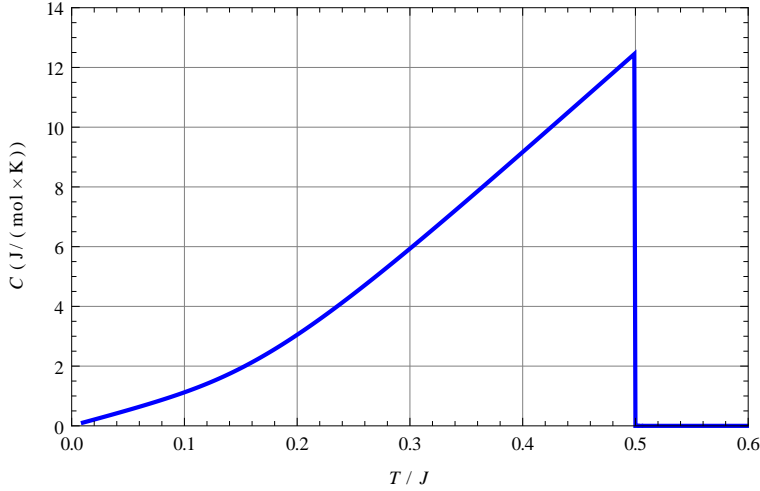


Abbildung D.4: Temperaturabhängigkeit unseres Meanfield-Ergebnisses für die spezifische Wärme C für $B = 0$ und $J'/J = 1/3$. Für $T < T_c = J/2$ ist allein der zur Austauschkopplung $J_1 = J$ gehörende variationelle Parameter Z_1 endlich.

liegt eine endliche Magnetisierung vor und daher müssen zusätzlich die endlichen Erwartungswerte $\langle \eta_i^x \eta_i^y \rangle$ bei der Meanfield-Entkopplung berücksichtigt werden,

$$\begin{aligned}
 \mathbf{S}_i \cdot \mathbf{S}_j &= \frac{1}{2} \sum_{\alpha \neq \beta} \eta_i^\alpha \eta_j^\alpha \eta_i^\beta \eta_j^\beta \\
 &\rightarrow \frac{1}{2} \sum_{\alpha \neq \beta} \left(C_{ij}^\alpha \langle C_{ij}^\beta \rangle + \langle C_{ij}^\alpha \rangle C_{ij}^\beta - \langle C_{ij}^\alpha \rangle \langle C_{ij}^\beta \rangle \right) \\
 &\quad - (\eta_i^x \eta_i^y \langle \eta_j^x \eta_j^y \rangle + \langle \eta_i^x \eta_i^y \rangle \eta_j^x \eta_j^y - \langle \eta_i^x \eta_i^y \rangle \langle \eta_j^x \eta_j^y \rangle). \quad (D.20)
 \end{aligned}$$

Die zusätzlichen Terme renormieren das effektive Magnetfeld, das auf die Spins wirkt, so dass das externe Feld h ersetzt wird durch

$$b = h - \tilde{J}_0 m, \quad (D.21)$$

mit dem magnetischen Moment $m = -i \langle \eta_i^x \eta_i^y \rangle$ und $\tilde{J}_0 = 2 \sum_\mu J_\mu$. Mit diesem Meanfield-Ansatz finden wir, dass die kritische Temperatur gegeben ist durch die Selbstkonsistenzgleichung

$$\frac{T_c}{J} = \frac{1}{6} + \frac{1}{3 \cosh^2[(h - \tilde{J}_0 m_c)/(2T_c)]}, \quad (D.22)$$

wobei das magnetische Moment m_c bestimmt wird durch

$$m_c = \frac{1}{2} \tanh \left[(h - \tilde{J}_0 m_c)/(2T_c) \right]. \quad (D.23)$$

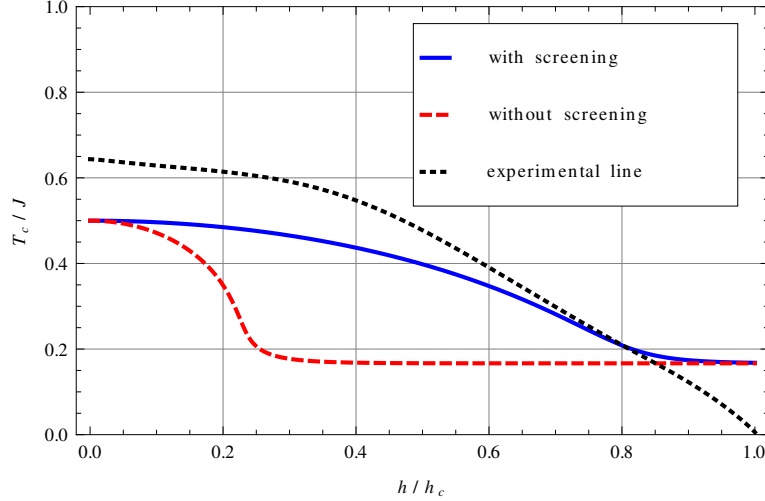


Abbildung D.5: Meanfield-Ergebnis für die Magnetfeldabhängigkeit der kritischen Temperatur für Spinflüssigkeitsverhalten in Cs_2CuCl_4 . Die gestrichelte Linie berücksichtigt nicht die selbstkonsistente Abschirmung des externen Magnetfeldes. Die durchgezogene Linie berücksichtigt diesen Effekt; siehe Gl. (D.21). Die gepunktete Linie gibt die experimentell bestimmte Übergangslinie aus Ref. [35] an; siehe auch Abb. D.2.

Für ein gegebenes Magnetfeld können die gekoppelten Gleichungen (D.22) und (D.23) simultan gelöst werden, woraus wir T_c und m_c als Funktion von h erhalten. Mit den für Cs_2CuCl_4 relevanten Parametern ($h_c/J = 2.85$ und $\tilde{J}_0/h_c = 1.18$) erhalten wir die kritische Temperatur, die in Abb. D.5 als durchgezogene Linie gezeigt wird und die das experimentelle Verhalten der kritischen Temperatur bis zu Feldern $B \lesssim 0.8B_c$ gut beschreibt. In Abb. D.6 sehen wir, dass die magnetische Suszeptibilität $\chi \approx M/B$ (wobei M die makroskopische Magnetisierung ist) ein Maximum bei der kritischen Temperatur $T_c = J/2 = 2.17$ K aufweist.

Wir fassen zusammen, dass wir eine einfache Meanfield-Beschreibung der Spinflüssigkeitsphase in Cs_2CuCl_4 entwickelt haben, die auf der Darstellung der Spinoperatoren durch Majorana-Fermionen basiert. Wir haben die experimentell beobachtete Übergangstemperatur für die Spinflüssigkeitsphase in Cs_2CuCl_4 identifiziert mit der kritischen Temperatur $T_c(B)$, unterhalb der die Meanfield-Gleichungen für die Dispersion der Majorana-Fermionen eine endliche Lösung haben. Unser Ergebnis für $T_c(B)$ stimmt bis zu Feldern $B \lesssim 0.8B_c$ quantitativ mit der experimentell beobachteten Übergangstemperatur der Spinflüssigkeitsphase in Cs_2CuCl_4 überein. Ferner haben wir festgestellt, dass die Majorana-Fermionen nur entlang der Richtung der stärksten Austauschkopplung propagieren können.

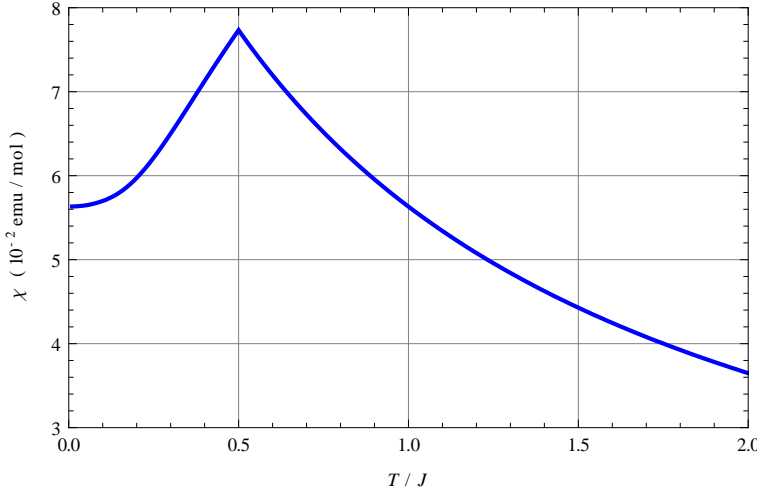


Abbildung D.6: Magnetische Suszeptibilität $\chi \approx M/B$ als Funktion von T/J für $J'/J = 1/3$ und $h/J = 0.01$, was einem externen Magnetfeld $B \approx 0.03$ T entspricht.

D.2 Ultraschallphysik in der Spinflüssigkeitsphase

In Kapitel 3 untersuchen wir die Schallgeschwindigkeit und Schalldämpfung in der Spinflüssigkeitsphase von Cs_2CuCl_4 und vergleichen unsere Ergebnisse für die c_{22} -Mode (siehe Abb. D.7) mit experimentellen Daten aus Ultraschallexperimenten [P3]; wir betrachten nur den Fall eines Magnetfeldes \mathbf{B} entlang der a -Achse, die senkrecht zur Gitterebene steht. In Kapitel 2 haben wir gesehen, dass die elementaren Spinanregungen quasi-eindimensional sind und bevorzugt entlang der Richtung der größten Austauschkopplung propagieren; in unserem Fall ist diese Richtung die kristallographische b -Achse. Diese dimensionale Reduktion wurde in mehreren unabhängigen theoretischen Untersuchungen beobachtet [P2, 3–8, 10, 12, 20, 65]. Diese Arbeit gibt weitere Unterstützung für dieses Szenario der dimensionalen Reduktion [9], da wir zeigen, dass Ultraschallexperimente, die die Schallausbreitung entlang der b -Achse untersuchen, quantitativ mit Hilfe eines an Phononen gekoppelten eindimensionalen Heisenberg-Modells erklärt werden können. Die Kopplung an die Gitterschwingungen erfolgt dadurch, dass die Austauschkopplungen von der aktuellen Gitterdeformation abhängen (das ist der sogenannte “exchange-striction mechanism”) [71].

Von der exakten Bethe-Ansatz-Lösung der eindimensionalen Spin-1/2 Heisenberg-Kette wissen wir, dass der Grundzustand eine Spinflüssigkeit mit algebraischen Korrelationen ohne langreichweitige Ordnung ist. Die elementaren Anregungen sind Spinonen, die einen fraktionalen Spin ($S = 1/2$) haben (Magnonen haben hingegen $S = 1$). Aus einer Kombination von numerischen und analytischen Methoden ist ein tiefes Verständnis dieses Modells hervorge-

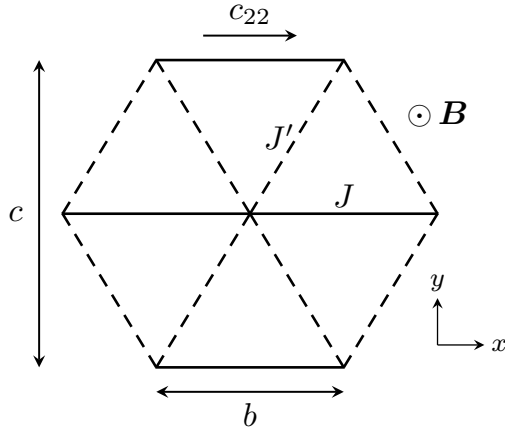


Abbildung D.7: Ausschnitt des anisotropen Dreiecksgitters, das von den Spins in Cs_2CuCl_4 gebildet wird. Die stärkste Austauschkopplung J verbindet die Spins nächster Nachbarn entlang der kristallographischen b -Achse. Die zugehörige elastische Konstante trägt die Bezeichnung c_{22} . Wir betrachten nur den Fall eines Magnetfeldes \mathbf{B} entlang der a -Achse, die senkrecht zur Gitterebene steht.

gangen [45]. Eine mikroskopische Berechnung der Schallgeschwindigkeit und Schalldämpfung fehlte aber bisher. Wir präsentieren eine einfache Lösung dieses Problems, die auf der Jordan-Wigner-Darstellung der Spinoperatoren durch spinlose Fermionen beruht [44]. Die Ultraschallphysik von Cs_2CuCl_4 ist zuvor schon untersucht worden für Magnetfelder entlang der a -Achse in der geordneten Phase im Rahmen einer Spinwellentheorie [27] und für Magnetfelder entlang der b -Achse in der Spinflüssigkeitsphase, wobei phänomenologische Gleichungen für Schallgeschwindigkeit und Schalldämpfung mit Berechnungen für zweidimensionale Spinmodelle kombiniert worden sind [26].

Wenn wir nun annehmen, dass die Spinanregungen in der Spinflüssigkeitsphase von Cs_2CuCl_4 nur entlang der b -Achse propagieren können, dann erwarten wir, dass wir Ultraschallexperimente für die c_{22} -Mode entlang der b -Achse mit Hilfe des folgenden eindimensionalen Spin-Phonon-Hamiltonians beschreiben können,

$$\mathcal{H} = \sum_n J_n (\mathbf{S}_n \cdot \mathbf{S}_{n+1} - 1/4) - h \sum_n S_n^z + \mathcal{H}_2^p, \quad (\text{D.24})$$

wo \mathbf{S}_n die entlang einer Kette mit N Spins an den Position x_n lokalisierten Spin-1/2-Operator sind und periodische Randbedingungen erfüllen. Die Spin-Phonon-Kopplung kommt nun dadurch zu Stande, dass bei vorliegenden Gitterschwingungen die Spins die Positionen $x_n = nb + X_n$ haben, wobei nb (mit $n = 1, \dots, N$) die Punkte eines eindimensionalen Gitters mit Gitterkonstante b sind und X_n die Auslenkungen von den Gitterpunkten bezeichnet. Da die Austauschkopplungen J_n zwischen zwei Spins \mathbf{S}_n und \mathbf{S}_{n+1} auf den Positionen x_n und x_{n+1} vom Abstand zwischen den Spins abhängt, muss J_n eine Funktion

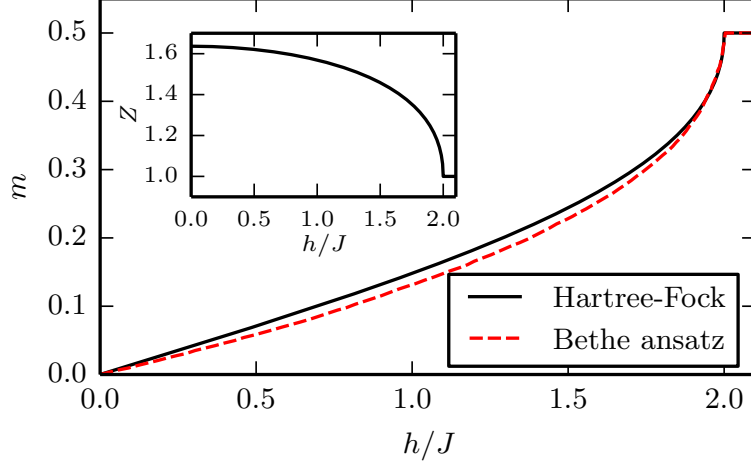


Abbildung D.8: Vergleich der Hartree-Fock-Näherung für die Magnetisierungscurve $m(h)$ der Heisenberg-Kette (ohne Phononen) bei $T = 0$ mit dem exakten Bethe-Ansatz [76]. Einsatzbild: Renormierung $Z(h)$ des Hüpfterms zwischen nächsten Nachbarn.

von $X_{n+1} - X_n$ sein. Wir entwickeln für kleine Auslenkungen bis zur zweiten Ordnung,

$$J_n \approx J + J^{(1)}(X_{n+1} - X_n) + \frac{J^{(2)}}{2}(X_{n+1} - X_n)^2, \quad (\text{D.25})$$

wobei $J^{(1)}$ und $J^{(2)}$ die erste und zweite Ableitung der Austauschkopplung bezüglich der Phononkoordinaten sind. Wir quantisieren die Gitterschwingungen, indem wir verlangen, dass $[X_n, P_m] = i\delta_{n,m}$, wobei wir $\hbar = 1$ setzen und P_n der zu X_n konjugierte Impuls ist. Der letzte Term in Gleichung (D.24) beschreibt nicht-wechselwirkende Phononen mit Dispersion $\omega_q = c|q|/b$,⁹

$$\mathcal{H}_2^p = \sum_q \left(\frac{P_{-q}P_q}{2M} + \frac{M}{2}\omega_q^2 X_{-q}X_q \right), \quad (\text{D.26})$$

wobei M die zu den Spins zugeordnete Masse (also die Masse einer Cs_2CuCl_4 -Einheit) ist und die Operatoren X_q und P_q definiert sind durch die Fourier-Entwicklungen $X_n = N^{-1/2} \sum_q e^{iqn} X_q$ und $P_n = N^{-1/2} \sum_q e^{iqn} P_q$; dabei ist der Phononimpuls q in Einheiten der inversen Gitterkonstante $1/b$ gegeben.

Um die Ultraschallexperimente zu beschreiben, berechnen wir die Selbstenergiekorrektur $\Pi(q, i\bar{\omega})$ des Phononpropagators, die von der Spin-Phonon-Kopplung herrührt. Dazu stellen wir die Spin-Operatoren mit Hilfe der Jordan-Wigner-Transformation durch spinlose Fermionen dar [44],

$$S_n^+ = (S_n^-)^\dagger = c_n^\dagger (-1)^n e^{i\pi \sum_{j < n} c_j^\dagger c_j}, \quad S_n^z = c_n^\dagger c_n - 1/2, \quad (\text{D.27})$$

⁹Die Schallgeschwindigkeit c in x -Richtung sollte nicht mit der Gitterkonstanten c in Abb. D.7 verwechselt werden. Im Kontext der Ultraschallphysik bezeichnen wir mit c die Schallgeschwindigkeit.

wobei c_n ein Fermion am Ort x_n vernichtet. Unser Spin-Phonon-Hamiltonian (D.24) wird dann zu

$$\begin{aligned}\mathcal{H} &= -\frac{1}{2} \sum_n J_n (c_n^\dagger c_{n+1} + c_{n+1}^\dagger c_n + c_n^\dagger c_n + c_{n+1}^\dagger c_{n+1}) \\ &+ \sum_n J_n c_n^\dagger c_n c_{n+1}^\dagger c_{n+1} - h \sum_n c_n^\dagger c_n + Nh/2 + \mathcal{H}_2^p.\end{aligned}\quad (\text{D.28})$$

Die Zweiteilchenwechselwirkung in der zweiten Zeile von Gleichung (D.28) behandeln wir mit der selbstkonsistenten Hartree-Fock-Näherung, in der wir den Zweiteilchenterm nähern durch

$$\begin{aligned}c_n^\dagger c_n c_{n+1}^\dagger c_{n+1} &\approx \rho(c_{n+1}^\dagger c_{n+1} + c_n^\dagger c_n) - \rho^2 \\ &- \tau(c_n^\dagger c_{n+1} + c_{n+1}^\dagger c_n) + \tau^2,\end{aligned}\quad (\text{D.29})$$

wobei die dimensionslosen variationellen Parameter ρ und τ die folgenden Selbstkonsistenzgleichungen erfüllen,

$$\rho = \langle c_n^\dagger c_n \rangle, \quad \tau = \langle c_n^\dagger c_{n+1} \rangle. \quad (\text{D.30})$$

Die Lösung dieser Gleichungen ohne Phononen wurde von Bulaevskii schon vor einiger Zeit ausgearbeitet [81]. Innerhalb dieser Hartree-Fock-Näherung ist die Dispersion der Fermionen $\xi_k = -ZJ \cos k + 2mJ - h$. Dabei ist $Z = 1 + 2\tau$ der dimensionslosen Renormierungsfaktor der Hüpfprozesse nächster Nachbarn, $m = \rho - 1/2$ ist die dimensionslose Magnetisierung und k ist der Gitterimpuls der Fermionen in Einheiten der inversen Gitterkonstanten $1/b$. In Abb. D.8 zeigen wir die numerischen Ergebnisse für $Z(h)$ bei $T = 0$ und wir vergleichen unser Hartree-Fock-Ergebnis für $m(h)$ mit dem exakten Bethe-Ansatz-Ergebnis für die Magnetisierungskurve der Heisenberg-Kette [76].

Setzen wir nun die Gradientenentwicklung (D.25) für die Austauschkopplung und die Hartree-Fock-Näherung (D.29) in Gl. (D.28) ein, erhalten wir die folgende Näherung für den Spin-Phonon-Hamiltonian,

$$\mathcal{H} = F_0 + \sum_k \xi_k c_k^\dagger c_k + \mathcal{H}_2^p + \delta\mathcal{H}_2^p + \mathcal{H}_3^{sp} + \mathcal{H}_4^{sp}, \quad (\text{D.31})$$

mit $F_0/N = h/2 + J(\tau^2 - \rho^2)$ und

$$\delta\mathcal{H}_2^p = 2J^{(2)}(\tau^2 - \rho^2) \sum_q \sin^2(q/2) X_{-q} X_q, \quad (\text{D.32a})$$

$$\mathcal{H}_3^{sp} = \frac{1}{\sqrt{N}} \sum_{k'kq} \delta_{k',k+q}^* \Gamma_3(k, q) c_{k'}^\dagger c_k X_q, \quad (\text{D.32b})$$

$$\mathcal{H}_4^{sp} = \frac{1}{2N} \sum_{k'kq_1q_2} \delta_{k',k+q_1+q_2}^* \Gamma_4(k, q_1, q_2) c_{k'}^\dagger c_k X_{q_1} X_{q_2}. \quad (\text{D.32c})$$

Der Term $\delta_{k',k}^* = \sum_m \delta_{k',k+2\pi m}$ stellt die Impulserhaltung modulo eines reziproken Gittervektors sicher, wir definieren $c_k = N^{-1/2} \sum_n e^{-ikn} c_n$, und die kubischen und quartischen Wechselwirkungsvertices sind für kleine Phononimpulse gegeben durch

$$\Gamma_3(k, q) \approx -iqJ^{(1)}(Z \cos k - 2m), \quad (\text{D.33a})$$

$$\Gamma_4(k, q_1, q_2) \approx q_1 q_2 J^{(2)}(Z \cos k - 2m). \quad (\text{D.33b})$$

Der Propagator des Phononfeldes X_q , der proportional zu $[\bar{\omega}^2 + \omega_q^2 + \Pi(q, i\bar{\omega})]^{-1}$ ist, erhält aufgrund der Kopplung an die Fermionen eine impuls- und frequenzabhängige Selbstenergiekorrektur $\Pi(q, i\bar{\omega})$, wobei $\bar{\omega}$ eine bosonische Matsubara-Frequenz ist. In zweiter Ordnung in Gradienten der Austauschkopplung hat die Phononselbstenergie drei Beiträge, $\Pi(q, i\bar{\omega}) = \Pi_2(q) + \Pi_3(q, i\bar{\omega}) + \Pi_4(q)$, mit

$$\Pi_2(q) = (J^{(2)}/M) (\tau^2 - \rho^2) 4 \sin^2(q/2), \quad (\text{D.34a})$$

$$\Pi_3(q, i\bar{\omega}) = \frac{1}{MN} \sum_k \frac{f_k - f_{k+q}}{\xi_k - \xi_{k+q} + i\bar{\omega}} |\Gamma_3(k, q)|^2, \quad (\text{D.34b})$$

$$\Pi_4(q) = \frac{1}{MN} \sum_k f_k \Gamma_4(k, q, -q), \quad (\text{D.34c})$$

wobei $f_k = (e^{\beta\xi_k} + 1)^{-1}$ die Besetzung des Fermionenzustands mit Impuls k in selbkonsistenter Hartree-Fock-Näherung ist. Aus der analytischen Fortsetzung der Selbstenergie $\Pi(q, i\bar{\omega})$ zu reellen Frequenzen erhalten wir die renormierte Phonondispersion und die Schalldämpfung [27],

$$\tilde{\omega}_q = \omega_q + \frac{\text{Re}\Pi(q, \omega_q + i0)}{2\omega_q}, \quad \gamma_q = -\frac{\text{Im}\Pi(q, \omega_q + i0)}{2\omega_q}. \quad (\text{D.35})$$

Die renormierte Schallgeschwindigkeit kann dann via $\tilde{c}/c = \lim_{q \rightarrow 0} \tilde{\omega}_q/\omega_q$ berechnet werden. Daraus folgt für der Renormierung $\Delta c = \tilde{c} - c$,

$$\Delta c/c = g_1 c^{(1)} + g_2 c^{(2)}, \quad (\text{D.36a})$$

$$c^{(1)} = \mathcal{P} \int_{-\pi}^{\pi} \frac{dk}{2\pi} J f'(\xi_k) \frac{v_k}{v_k - c} (2m - Z \cos k)^2, \quad (\text{D.36b})$$

$$c^{(2)} = m^2 - Z^2/4, \quad (\text{D.36c})$$

wobei \mathcal{P} das Cauchy-Hauptwertintegral bezeichnet, $f'(\xi_k) = -\beta f_k(1 - f_k)$ die Ableitung der Fermifunktion ist und $v_k = Z J b \sin k$ die Gruppengeschwindigkeit der fermionischen Anregungen ist. Wir haben hier die dimensionslosen Kopplungskonstanten $g_1 = (J^{(1)} b)^2 / (2 M c^2 J)$ und $g_2 = J^{(2)} b^2 / (2 M c^2)$ eingeführt. Prinzipiell sollte es möglich sein diese Kopplungskonstanten mit *ab initio* Methoden zu berechnen, aber wir bestimmen hier einfach g_1 und g_2 , indem wir unsere theoretischen Ergebnisse (D.36) an die experimentellen Daten fitten.

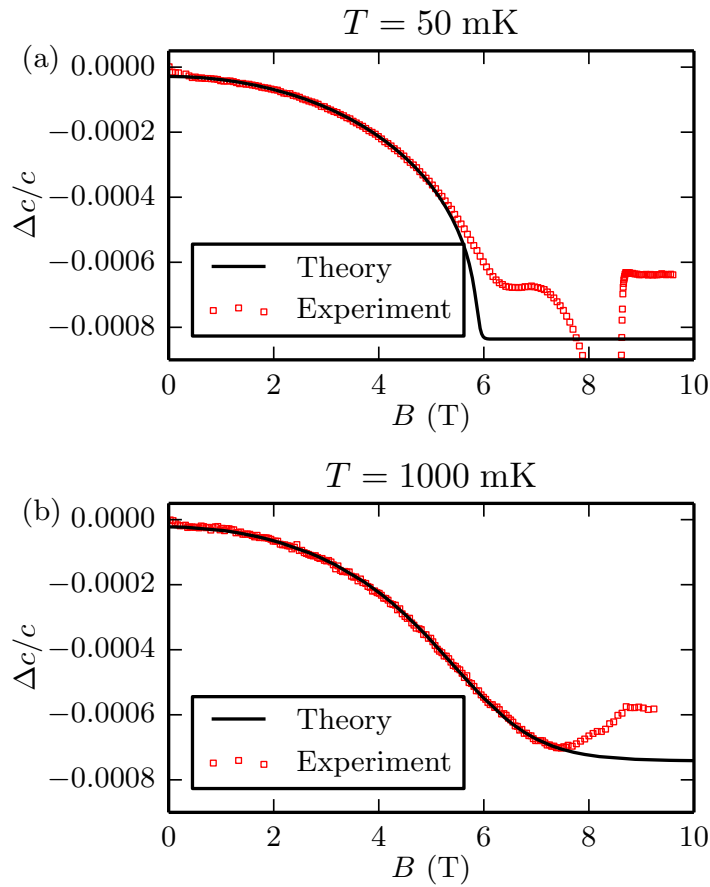


Abbildung D.9: Vergleich von theoretischen und experimentellen Werten für die relative Änderung der Schallgeschwindigkeit der c_{22} -Mode: (a) in der geordneten Phase ($T = 50 \text{ mK}$) mit Kopplungskonstanten $g_1 = 0$ und $g_2 = -1.2 \times 10^{-3}$, (b) in der Spinflüssigkeitsphase ($T = 1 \text{ K}$) mit Kopplungskonstanten $g_1 = 0$ und $g_2 = -1.1 \times 10^{-3}$.

In Abbildung D.9 vergleichen wir theoretische und experimentelle Ergebnisse (gemessen von Pham Thanh Cong [P3]) als Funktion des Magnetfeldes. Beim Fitten an die experimentellen Daten für die relative Änderung der Schallgeschwindigkeit $\Delta c/c$ finden wir $g_1 \approx 0$ und $g_2 \approx -1.1 \times 10^{-3}$. Der Term $c^{(1)}$ ist mehr als eine Größenordnung kleiner als $c^{(2)}$, da $c/(Jb) \approx 6.8$ relativ groß ist. Während in der geordneten Phase ($T = 50 \text{ mK}$, obere Abbildung) unsere theoretischen Ergebnisse (D.36) für Magnetfelder von bis zu 5 T mit den experimentellen Daten gut übereinstimmen, erhalten wir in der Spinflüssigkeitsphase ($T = 1 \text{ K}$, untere Abbildung) eine sehr gute Übereinstimmung zwischen Theorie und Experiment bis zu Magnetfeldern von 7 T. Die Abweichungen bei größeren Feldern lassen sich dadurch erklären, dass in diesem Regime die Fluktuationen durch den quantenkritischen Punkt des verdünnten Bose-Gases bei $B_c = 8.5 \text{ T}$ bestimmt werden [14], die durch unser eindimensionales

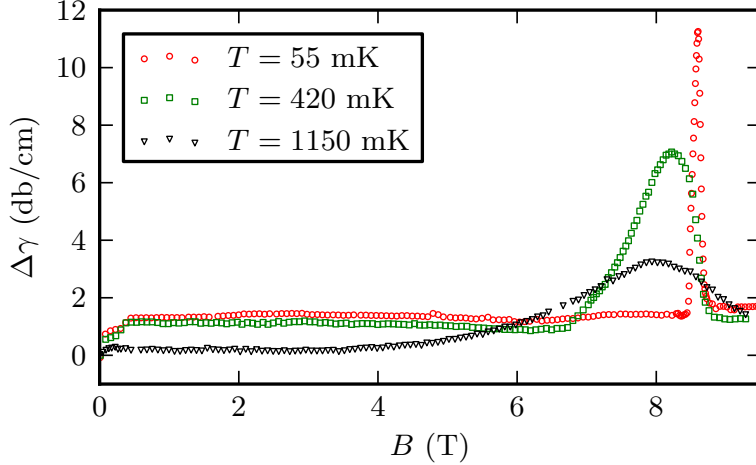


Abbildung D.10: Experimentelle Daten für die relative Änderung $\Delta\gamma$ der Schalldämpfung der c_{22} -Mode als Funktion des magnetischen Feldes für drei verschiedene Temperaturwerte.

Modell nicht beschrieben werden können. Abschließend betrachten wir noch die Ultraschalldämpfung der c_{22} -Mode in Cs_2CuCl_4 . Die experimentellen Daten für drei verschiedene Temperaturen als Funktion des Magnetfeldes sind in Abb. D.10 dargestellt. Im Regime $B \lesssim 7$ T, wo die Fluktuationen des quantenkritischen Punktes vernachlässigbar und unsere theoretischen Ergebnisse für die Renormierung der Schallgeschwindigkeit mit den experimentellen Daten übereinstimmen, ist die Dämpfung sehr klein und nahezu konstant. Dies kann mit Hilfe unseres eindimensionalen Modells erklärt werden: Aus Gleichungen (D.34b) und (D.35) erhalten wir für die Dämpfung

$$\gamma_q = \frac{\pi}{2M\omega_q} \int_{-\pi}^{\pi} \frac{dk}{2\pi} (f_k - f_{k+q}) |\Gamma_3(k, q)|^2 \delta(\xi_k - \xi_{k+q} + \omega_q). \quad (\text{D.37})$$

Dieser Ausdruck ist nur dann ungleich Null, wenn die maximale Gruppengeschwindigkeit $v_* = ZJb$ der Fermionen größer als die Schallgeschwindigkeit c ist. Für Cs_2CuCl_4 ist das nie der Fall ($c/(Jb) \approx 6.8$) und damit liegt im Rahmen unserer Näherung keine Dämpfung für die c_{22} -Mode vor. Daraus folgt, dass in dem Bereich, in dem unsere Theorie eine gute Näherung darstellt, die relative Änderung der Dämpfung nicht vom Magnetfeld abhängen sollte.

Zusammenfassend lässt sich festhalten, dass wir eine einfache mikroskopische Theorie entwickelt haben, die die Ultraschallexperimente für die c_{22} -Mode in der Spinflüssigkeitsphase von Cs_2CuCl_4 erklären kann. Unsere dabei zugrunde liegende Annahme ist, dass in der Spinflüssigkeitsphase die elementaren Anregungen eindimensionale Fermionen sind. Die gute Übereinstimmung zwischen Theorie und Experiment in Abb. D.9 bestätigt die dimensionale Reduktion in der Spinflüssigkeitsphase von Cs_2CuCl_4 .

D.3 Hardcore-Boson-Ansatz in starken Magnetfeldern

In Kapitel 4 betrachten wir den Fall eines starken Magnetfeldes $B > B_c$ entlang der a -Achse. Die Magnonanregungen haben dann eine Energiefülle und der Grundzustand ist ein vollständig magnetisierter Ferromagnet. Unser Ziel ist es die thermischen Anregungen zu beschreiben und unsere Ergebnisse mit experimentellen Daten für die spezifische Wärme [14, 15] zu vergleichen. Dabei basiert unser theoretischer Ansatz auf der Darstellung der Spin-1/2-Operatoren durch Hardcore-Bosonen [46, 47]. Für Magnetfelder $B > B_c$ liegt bei niedrigen Temperaturen ein verdünntes Gas von Hardcore-Bosonen vor, wodurch die führenden Niedrigtemperaturkorrekturen zur Selbstenergie im Rahmen der (selbstkonsistenten) Leiternäherung berechnet werden können [48, 83]. Um den Gültigkeitsbereich der selbstkonsistenten Leiternäherung zu ermitteln, wenden wir diese auf das exakt lösbar eindimensionale XY-Modell an und gehen über die Untersuchung in Ref. [48] hinaus, indem wir den Zusammenbruch der selbstkonsistenten Leiternäherung in der Nähe des quantenkritischen Punktes dieses Modells untersuchen.

Unser Ausgangspunkt ist das für Cs_2CuCl_4 relevante Spin-1/2-Heisenberg-Modell (D.1),

$$\mathcal{H} = \frac{1}{2} \sum_{ij} [J_{ij} \mathbf{S}_i \cdot \mathbf{S}_j + \mathbf{D}_{ij} \cdot (\mathbf{S}_i \times \mathbf{S}_j)] - h \sum_i S_i^z. \quad (\text{D.38})$$

Wir stellen die Spinoperatoren durch Hardcore-Bosonen dar [46, 47],

$$S_i^+ = b_i, \quad S_i^- = b_i^\dagger, \quad S_i^z = 1/2 - b_i^\dagger b_i, \quad (\text{D.39})$$

wobei die Besetzungszahl an einem Gitterplatz $\hat{n}_i = 0$ oder 1 ist und die Hardcore-Bosonen die folgende Kommutationsrelation erfüllen müssen

$$[b_i, b_j^\dagger] = \delta_{ij} (1 - 2b_i^\dagger b_i). \quad (\text{D.40})$$

Diese Relationen lassen sich nun dadurch realisieren, dass wir die Hardcore-Bosonen als kanonische Bosonen mit einer unendlichen Kontaktwechselwirkung behandeln,

$$\mathcal{H}_U = \frac{U}{2} \sum_i b_i^\dagger b_i^\dagger b_i b_i, \quad \text{mit } U \rightarrow \infty. \quad (\text{D.41})$$

Indem wir die Hardcore-Boson-Darstellung (D.39) in unseren Hamiltonian (D.38) einsetzen, erhalten wir den folgenden Hardcore-Boson-Hamiltonian,

$$\mathcal{H} = \sum_{\mathbf{k}} \xi_{\mathbf{k}} b_{\mathbf{k}}^\dagger b_{\mathbf{k}} + \frac{1}{2N} \sum_{\mathbf{k}, \mathbf{k}', \mathbf{q}} (J_{\mathbf{q}} + U) b_{\mathbf{k}+\mathbf{q}}^\dagger b_{\mathbf{k}'-\mathbf{q}}^\dagger b_{\mathbf{k}'} b_{\mathbf{k}}, \quad (\text{D.42})$$

wobei wir für die Erzeugungs- und Vernichtungsoperatoren der Hardcore-Bosonen eine Fourier-Transformation verwendet haben,

$$b_{\mathbf{k}} = \frac{1}{\sqrt{N}} \sum_i b_i e^{-i\mathbf{k} \cdot \mathbf{R}_i}, \quad b_{\mathbf{k}}^\dagger = \frac{1}{\sqrt{N}} \sum_i b_i^\dagger e^{i\mathbf{k} \cdot \mathbf{R}_i}. \quad (\text{D.43})$$

Die Anregungsenergien $\xi_{\mathbf{k}}$ können geschrieben werden als

$$\xi_{\mathbf{k}} = \varepsilon_{\mathbf{k}} - \mu, \quad (\text{D.44})$$

mit chemischem Potential

$$\mu = h_c - h, \quad (\text{D.45})$$

und Energiedispersion

$$\varepsilon_{\mathbf{k}} = \frac{1}{2} (J_{\mathbf{k}}^D - J_{\mathbf{Q}}^D). \quad (\text{D.46})$$

Dabei ist

$$J_{\mathbf{k}}^D = J_{\mathbf{k}} - iD_{\mathbf{k}} \quad (\text{D.47})$$

und die Fourier-Transformierten der Austausch- und Dzyaloshinskii-Moriya-Wechselwirkungen sind gegeben durch

$$\begin{aligned} J_{\mathbf{k}} &= \sum_{\mathbf{R}} J(\mathbf{R}) e^{-i\mathbf{k} \cdot \mathbf{R}} \\ &= 2J \cos(k_x b) + 4J' \cos(k_x b/2) \cos(k_y c/2), \end{aligned} \quad (\text{D.48})$$

$$\begin{aligned} D_{\mathbf{k}} &= \sum_{\mathbf{R}} D(\mathbf{R}) e^{-i\mathbf{k} \cdot \mathbf{R}} \\ &= -4iD \sin(k_x b/2) \cos(k_y c/2). \end{aligned} \quad (\text{D.49})$$

In Gl. (D.46) ist $J_{\mathbf{Q}}^D \approx -2.325 J$ das absolute Minimum von $J_{\mathbf{k}}^D$ bei $\mathbf{Q} \approx (3.474/b, 0)$ und das Saturierungsfeld ist gegeben durch

$$B_c = \frac{h_c}{g\mu_B} = \frac{1}{2g\mu_B} (J_0^D - J_{\mathbf{Q}}^D) \approx 8.4 \text{ T}. \quad (\text{D.50})$$

Im Folgenden werden wir den direkten experimentellen Wert für das Saturierungsfeld $B_c = 8.44(1) \text{ T}$ anstelle von $B_c \approx 8.4 \text{ T}$ verwenden. Der Wert des Saturierungsfeldes B_c ist wichtig, da es für ein gegebenes Magnetfeld die Energielücke Δ bestimmt,

$$\Delta = -\mu = h - h_c. \quad (\text{D.51})$$

Das zentrale Problem ist nun, wie wir die Wechselwirkungen zwischen den Hardcore-Bosonen berücksichtigen. Der Wechselwirkungsterm im Hamiltonian (D.42) ist gegeben durch

$$\mathcal{H}_{\text{int}} = \frac{1}{2N} \sum_{\mathbf{k}, \mathbf{k}', \mathbf{q}} (J_{\mathbf{q}} + U) b_{\mathbf{k}+\mathbf{q}}^\dagger b_{\mathbf{k}'-\mathbf{q}}^\dagger b_{\mathbf{k}'} b_{\mathbf{k}} \quad (\text{D.52})$$

und enthält die Austauschwechselwirkung $J_{\mathbf{q}}$ und die unendliche Kontaktwechselwirkung $U \rightarrow \infty$. Wir werden die beiden Wechselwirkungsterme getrennt behandeln: Für den $J_{\mathbf{q}}$ -Term verwenden wir eine selbstkonsistente Hartree-Fock-Entkopplung und für die Hardcore-Wechselwirkung U die selbstkonsistente Leiternäherung [48]. Die Hartree-Fock-Entkopplung führt zu der Näherung

$$\frac{1}{2N} \sum_{\mathbf{k}, \mathbf{k}', \mathbf{q}} J_{\mathbf{q}} b_{\mathbf{k}+\mathbf{q}}^\dagger b_{\mathbf{k}'-\mathbf{q}}^\dagger b_{\mathbf{k}'} b_{\mathbf{k}} \approx \sum_{\mathbf{k}} (J_{\mathbf{k}}^\tau + n J_0) b_{\mathbf{k}}^\dagger b_{\mathbf{k}} + E_{\text{MF}}, \quad (\text{D.53})$$

wobei

$$J_{\mathbf{k}}^\tau = 2J \text{Re}(\tau_1 e^{i\mathbf{k}\cdot\delta_1}) + 2J' \text{Re}(\tau_2 e^{i\mathbf{k}\cdot\delta_2} + \tau_3 e^{i\mathbf{k}\cdot\delta_3}), \quad (\text{D.54})$$

$$E_{\text{MF}} = -N \left[\frac{J_0}{2} n^2 + J |\tau_1|^2 + J' (|\tau_2|^2 + |\tau_3|^2) \right]. \quad (\text{D.55})$$

Diese Näherung führt zu einer Renormierung der Einteilchen-Anregungsenergien $\xi_{\mathbf{k}} \rightarrow \tilde{\xi}_{\mathbf{k}}$, wobei die renormierten Anregungsenergien gegeben sind durch

$$\tilde{\xi}_{\mathbf{k}} = \varepsilon_{\mathbf{k}} - \mu + J_{\mathbf{k}}^\tau + n J_0. \quad (\text{D.56})$$

Dabei erfüllen die Hartree-Fock-Parameter die folgenden Selbstkonsistenzgleichungen,

$$\tau_i = \frac{1}{N} \sum_{\mathbf{k}} n_{\mathbf{k}} e^{-i\mathbf{k}\cdot\delta_i}, \quad (\text{D.57a})$$

$$n = \frac{1}{N} \sum_{\mathbf{k}} n_{\mathbf{k}}, \quad (\text{D.57b})$$

wobei die Besetzungszahl des Zustands mit Impuls \mathbf{k} gegeben ist durch

$$n_{\mathbf{k}} = \langle b_{\mathbf{k}}^\dagger b_{\mathbf{k}} \rangle. \quad (\text{D.58})$$

Nach der Hartree-Fock-Entkopplung der $J_{\mathbf{q}}$ -Wechselwirkungen erhalten wir damit einen Hamiltonian, bei dem die einzige verbleibende Wechselwirkung die unendliche Kontaktwechselwirkung ist,

$$\mathcal{H} = \sum_{\mathbf{k}} \tilde{\xi}_{\mathbf{k}} b_{\mathbf{k}}^\dagger b_{\mathbf{k}} + \frac{U}{2N} \sum_{\mathbf{k}, \mathbf{k}', \mathbf{q}} b_{\mathbf{k}+\mathbf{q}}^\dagger b_{\mathbf{k}'-\mathbf{q}}^\dagger b_{\mathbf{k}'} b_{\mathbf{k}} + E_{\text{MF}}. \quad (\text{D.59})$$

Für die unendliche Kontaktwechselwirkung können wir nun die selbstkonsistente Leiternäherung verwenden, die in Ref. [48] entwickelt worden ist. In dieser Näherung wird die Selbstenergie $\Sigma(K)$ der Hardcore-Bosonen durch eine Summierung aller Teilchen-Teilchen-Leiterdiagramme genähert. Dazu drücken wir die Selbstenergie durch die effektive Wechselwirkung $\Gamma(P)$ aus,

$$\Sigma(K) = -2 \int_Q G(Q) \Gamma(Q+K) e^{i\omega_q 0^+}. \quad (\text{D.60})$$

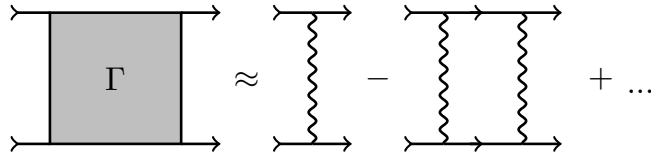


Abbildung D.11: Leiternäherung für die effektive Wechselwirkung Γ .

Wir verwenden hier die Indexnotation $K = (\mathbf{k}, i\omega_k)$ mit der zugehörigen Summe

$$\int_K = \frac{1}{\beta N} \sum_{\mathbf{k}} \sum_{\omega_k}, \quad (\text{D.61})$$

wobei ω_k bosonische Matsubara-Frequenzen sind und $\beta = 1/T$ die inverse Temperatur ist. Die effektive Wechselwirkung $\Gamma(P)$ besteht dann aus der unendlichen Reihe von Teilchen-Teilchen-Leiterdiagrammen, die in Abb. D.11 angedeutet sind, und lässt sich schreiben als

$$\Gamma(P) = \frac{U}{1 + U \int_Q G(Q)G(P-Q)}, \quad (\text{D.62})$$

wobei die Greensche Funktion $G(K)$ definiert ist durch

$$G(K) = \frac{1}{G_0^{-1}(K) - \Sigma(K)}, \quad (\text{D.63})$$

mit der freien Greenschen Funktion

$$G_0(K) = \frac{1}{i\omega_k - \tilde{\xi}_{\mathbf{k}}}. \quad (\text{D.64})$$

Dieses Selbstkonsistenzproblem für die Selbstenergie $\Sigma(K)$ formulieren wir nun um, indem wir die Spektraldarstellung der Greenschen Funktion verwenden,

$$G(K) = \int_{-\infty}^{\infty} dx \frac{A(\mathbf{k}, x)}{i\omega_k - x}, \quad (\text{D.65})$$

wobei die Spektralfunktion gegeben ist durch

$$\begin{aligned} A(\mathbf{k}, \omega) &= -\frac{1}{\pi} \text{Im}G(\mathbf{k}, \omega + i0^+) \\ &= -\frac{1}{\pi} \frac{\text{Im}\Sigma^R(\mathbf{k}, \omega)}{\left[\omega - \tilde{\xi}_{\mathbf{k}} - \text{Re}\Sigma^R(\mathbf{k}, \omega)\right]^2 + [\text{Im}\Sigma^R(\mathbf{k}, \omega)]^2} \end{aligned} \quad (\text{D.66})$$

und die retardierte Selbstenergie über die analytische Fortsetzung zu reellen Frequenzen erhalten werden kann,

$$\Sigma^R(\mathbf{k}, \omega) = \Sigma(\mathbf{k}, \omega + i0^+). \quad (\text{D.67})$$

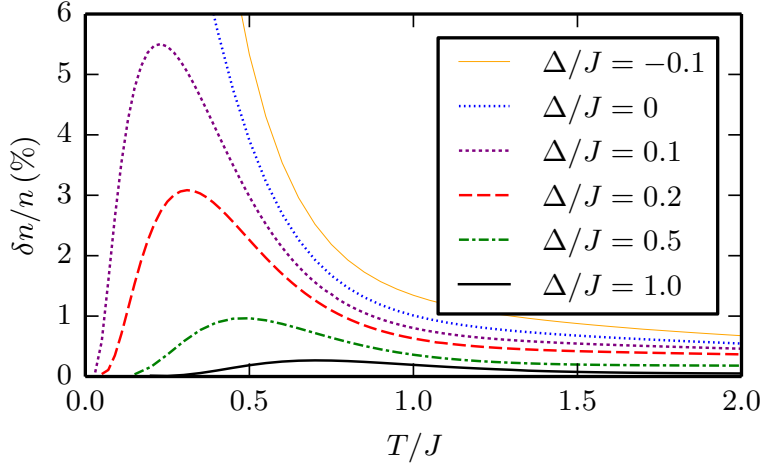


Abbildung D.12: Relativer Fehler $\delta n/n$ der Bosondichte (siehe Gl. (D.71)) in der selbstkonsistenten Leiternäherung für das eindimensionale XY -Modell als Funktion der Temperatur bei verschiedenen Energielücken Δ .

Nachdem wir dann den Limes $U \rightarrow \infty$ für die obigen Gleichungen genommen haben, können wir eine selbstkonsistente Lösung für die Spektralfunktion berechnen, indem wir von einer anfänglichen Spektralfunktion starten und aus den Gleichungen (D.60) und (D.66) die nächste Iteration erhalten. Nach jeder Iteration müssen die Hartree-Fock-Parameter n , τ_1 , τ_2 und τ_3 über die Selbstkonsistenzgleichungen (D.57a) und (D.57b) aktualisiert werden.

Bevor wir nun diese Methode für Cs_2CuCl_4 auswerten, ist es sinnvoll den Gültigkeitsbereich dieser Näherung für das exakt lösbare eindimensionale Spin-1/2- XY -Modell zu untersuchen. Dieses Modell ist gegeben durch

$$\mathcal{H}_{1D} = J \sum_i (S_i^x S_{i+1}^x + S_i^y S_{i+1}^y) - h \sum_i S_i^z \quad (\text{D.68})$$

und kann durch Hardcore-Bosonen dargestellt werden,

$$\mathcal{H}_{1D} = \sum_k \xi_k b_k^\dagger b_k + \frac{U}{2N} \sum_{k,k',q} b_{k+q}^\dagger b_{k'-q}^\dagger b_{k'} b_k, \quad (\text{D.69})$$

mit Anregungsenergie

$$\xi_k = J [\cos(k_x b) + 1] - \mu, \quad (\text{D.70})$$

wobei $\mu = h_c - h = -\Delta$ und $h_c = J$. Der relative Fehler der Bosondichte in der selbstkonsistenten Leiternäherung ist in Abb. D.12 dargestellt und ist definiert durch

$$\delta n/n = \frac{n_{\text{ladder}} - n_{\text{exact}}}{n_{\text{exact}}}. \quad (\text{D.71})$$

Dabei ist n_{ladder} das Ergebnis aus der selbstkonsistenten Leiternäherung und n_{exact} das exakte Ergebnis. Wir sehen, dass bei einer endlichen Energielücke

$\Delta > 0$ der Fehler sowohl bei niedrigen als auch hohen Temperaturen verschwindet, wobei der maximale Fehler bei $T \approx \Delta$ liegt. Zudem wird der Fehler mit wachsender Energielücke kleiner. Bei $\Delta = 0$ nimmt der Fehler für kleinere Temperaturen immer mehr zu (also in der Nähe des quantenkritischen Punktes bei $T = 0$), nimmt aber für höhere Temperaturen ab. Wir halten fest, dass die selbstkonsistente Leiternäherung gute Resultate über das ganze Temperaturspektrum liefert für Energielücken $\Delta \gtrsim 0.1 J$.

Wir werten nun die zuvor hergeleitete Methode zur Berechnung der Spektralfunktion für Cs_2CuCl_4 aus. Aufgrund der endlichen Energielücke $\Delta > 0$ ist die Spektralfunktion bei $T = 0$ gegeben durch die nicht-wechselwirkende Spektralfunktion,

$$A(\mathbf{k}, \omega) = A_0(\mathbf{k}, \omega) = \delta(\omega - \xi_{\mathbf{k}}). \quad (\text{D.72})$$

Bei endlichen Temperaturen wird der scharfe Deltapeak aufgeweicht, wie in Abb. D.13 zu sehen ist. Zudem bemerken wir, dass die Bandbreite reduziert wird und das Minimum der Spektralfunktion sich zu höheren Energien verschiebt, wodurch die effektive Energielücke größer wird als die ursprüngliche Energielücke Δ bei $T = 0$. Aufgrund der endlichen Frequenzauflösung in unseren numerischen Rechnungen können wir nicht beliebig niedrige Temperaturen erreichen und sind beschränkt auf Temperaturen $T \gtrsim 0.2\Delta$, für die die Spektralfunktion noch aufgelöst werden kann. Im Temperaturbereich $T \lesssim 0.2\Delta$ können wir aber die Hardcore-Wechselwirkung vernachlässigen und nur die selbstkonsistente Hartree-Fock-Entkopplung ohne Hardcore-Wechselwirkung verwenden.

Mit Hilfe der Spektralfunktion können wir das magnetische Moment m pro Gitterplatz berechnen,

$$m = \langle S_i^z \rangle = \frac{1}{2} - n, \quad (\text{D.73})$$

wobei

$$n = \frac{1}{N} \sum_{\mathbf{k}} n_{\mathbf{k}} = \frac{1}{N} \sum_{\mathbf{k}} \int_{-\infty}^{\infty} dx A(\mathbf{k}, x) \frac{1}{e^{\beta x} - 1}. \quad (\text{D.74})$$

Die magnetische Suszeptibilität erhalten wir dann via

$$\chi = \frac{dm}{dT}. \quad (\text{D.75})$$

Unsere numerischen Ergebnisse für die Suszeptibilität für Magnetfelder oberhalb des Saturierungsfeldes sind in Abb. D.14 dargestellt. Die interne Energie ist gegeben durch

$$E = \langle \mathcal{H} \rangle = \sum_{\mathbf{k}} \tilde{\xi}_{\mathbf{k}} n_{\mathbf{k}} + E_{\text{MF}}, \quad (\text{D.76})$$

womit sich die spezifische Wärme berechnen lässt via

$$C = \frac{dE}{dT}. \quad (\text{D.77})$$

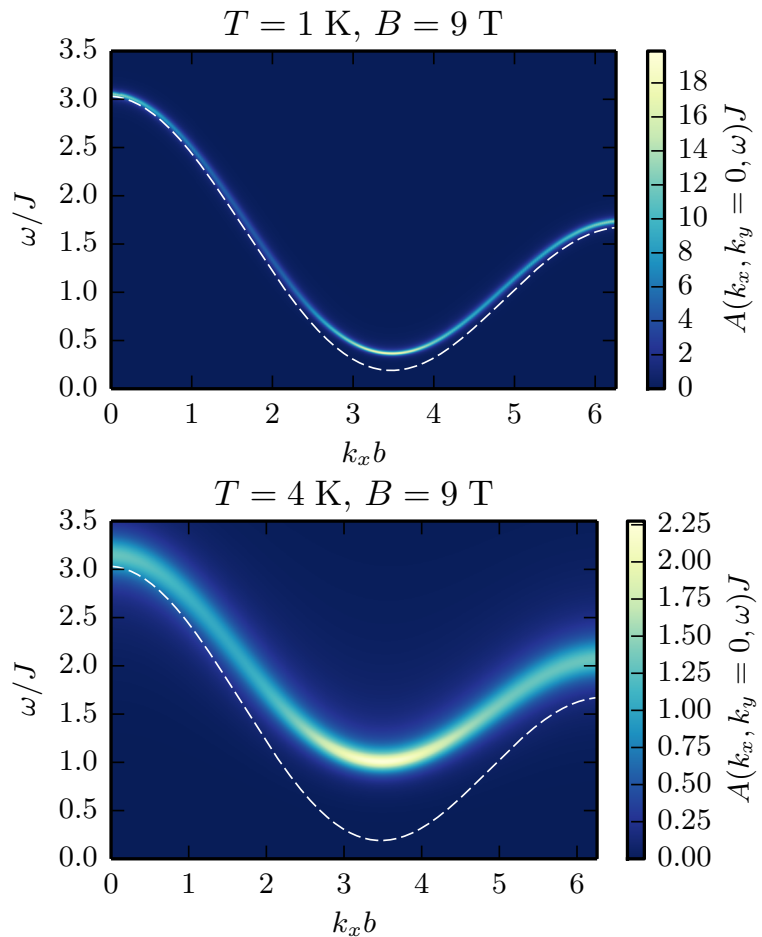


Abbildung D.13: Contourplots der Spektralfunktion $A(\mathbf{k}, \omega)$ der Hardcore-Bosonen bei $k_y = 0$ für Temperaturen von 1 K und 4 K in einem Magnetfeld $B = 9 \text{ T}$, was einer Energiefülle $\Delta = 0.19J$ entspricht. Die weiße gestrichelte Linie ist die unrenormierte Anregungsenergie $\xi_{\mathbf{k}}$, die durch Gl. (D.44) definiert ist.

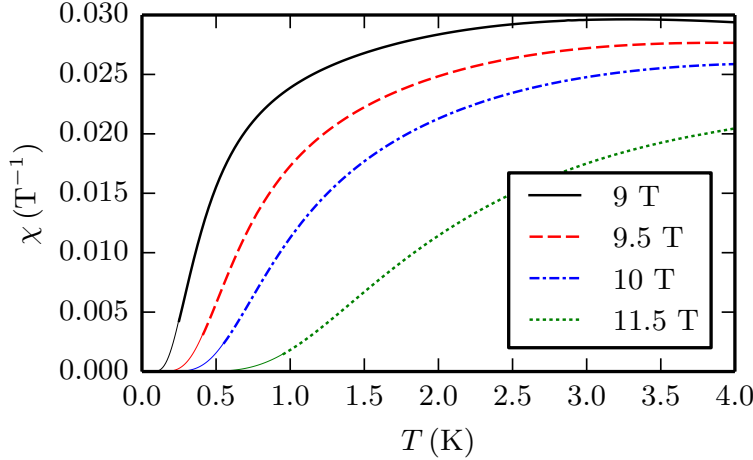


Abbildung D.14: Numerische Ergebnisse für die magnetische Suszeptibilität χ für Magnetfelder zwischen 9 T und 11.5 T. Die dünnen durchgehenden Linien sind Ergebnisse für niedrige Temperaturen aus der Hartree-Fock-Näherung ohne Hardcore-Wechselwirkung.

Der magnetische Beitrag zur spezifischen Wärme von Cs_2CuCl_4 ist experimentell bestimmt worden [14, 15] und wir vergleichen in Abb. D.15 unsere Ergebnisse mit den experimentellen Daten aus Ref. [15]. Wir stellen fest, dass unsere Theorie das experimentell beobachtete Verhalten sowohl qualitativ als auch quantitativ gut beschreibt.

Abschließend fassen wir zusammen, dass wir das für Cs_2CuCl_4 relevante Spin-1/2-Heisenberg-Modell auf ein Hardcore-Boson-Modell abgebildet haben, bei dem die Hardcore-Bedingung mit Hilfe einer unendlichen Kontaktwechselwirkung berücksichtigt worden ist. Da wir nur Magnetfelder $B > B_c$ betrachtet haben, konnten wir aufgrund der Energielücke die Hardcore-Wechselwirkung mit der selbstkonsistenten Leiternäherung [48] behandeln. Für die verbleibenden Austauschwechselwirkungen haben wir eine selbstkonsistente Hartree-Fock-Näherung verwendet. Wir haben für Cs_2CuCl_4 die magnetische Suszeptibilität und die spezifische Wärme berechnet, wobei das numerische Ergebnis für die spezifische Wärme in guter Übereinstimmung ist mit den verfügbaren experimentellen Daten. Während wir in dieser Arbeit von einem Spin-1/2-Modell ausgegangen sind, das wir auf Hardcore-Bosonen abgebildet haben, lässt sich unser theoretischer Ansatz generell immer dann anwenden, wenn die elementaren Anregungen eines System als Hardcore-Bosonen mit einer Energiefülle beschrieben werden können (für Beispiele siehe Ref. [48]).

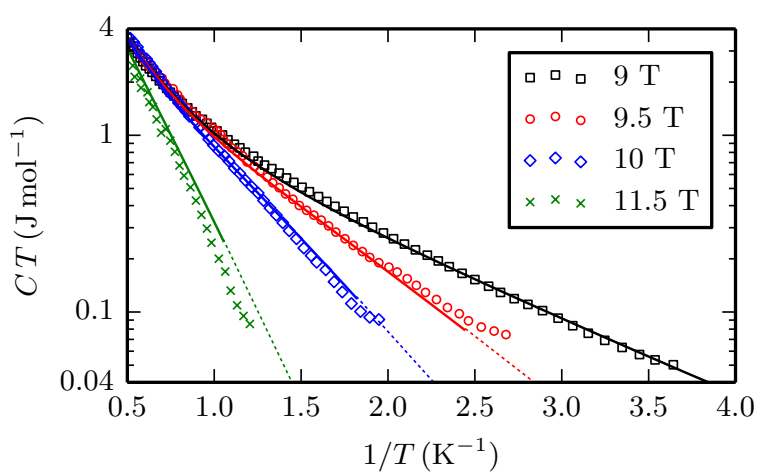


Abbildung D.15: Vergleich von unseren numerischen Ergebnissen für die spezifische Wärme (durchgehende Linien) mit den experimentellen Daten aus Ref. [15] (Symbole) für Magnetfelder zwischen 9 T und 11.5 T. Die gestrichelten Linien sind Ergebnisse für niedrige Temperaturen aus der Hartree-Fock-Näherung ohne Hardcore-Wechselwirkung.

Publications

- [P1] S. Streib, A. Isidori, and P. Kopietz, *Solution of the Anderson impurity model via the functional renormalization group*, Phys. Rev. B **87**, 201107(R) (2013).
- [P2] T. Herfurth, S. Streib, and P. Kopietz, *Majorana spin liquid and dimensional reduction in Cs_2CuCl_4* , Phys. Rev. B **88**, 174404 (2013).
- [P3] S. Streib, P. Kopietz, P. T. Cong, B. Wolf, M. Lang, N. van Well, F. Ritter, and W. Assmus, *Elastic constants and ultrasound attenuation in the spin-liquid phase of Cs_2CuCl_4* , Phys. Rev. B **91**, 041108(R) (2015).
- [P4] S. Streib and P. Kopietz, *Hard-core boson approach to the spin- $\frac{1}{2}$ triangular-lattice antiferromagnet Cs_2CuCl_4 at finite temperatures in magnetic fields higher than the saturation field*, Phys. Rev. B **92**, 094442 (2015).

(The publication [P1] resulted from my Master's project.)

Bibliography

- [1] R. Coldea, D. A. Tennant, and Z. Tyłczyński, *Extended scattering continua characteristic of spin fractionalization in the two-dimensional frustrated quantum magnet Cs_2CuCl_4 observed by neutron scattering*, Phys. Rev. B **68**, 134424 (2003).
- [2] R. Coldea, D. A. Tennant, A. M. Tsvelik, and Z. Tyłczyński, *Experimental Realization of a 2D Fractional Quantum Spin Liquid*, Phys. Rev. Lett. **86**, 1335 (2001).
- [3] S. Yunoki and S. Sorella, *Two spin liquid phases in the spatially anisotropic triangular Heisenberg model*, Phys. Rev. B **74**, 014408 (2006).
- [4] M. Q. Weng, D. N. Sheng, Z. Y. Weng, and R. J. Bursill, *Spin-liquid phase in an anisotropic triangular-lattice Heisenberg model: Exact diagonalization and density-matrix renormalization group calculations*, Phys. Rev. B **74**, 012407 (2006).
- [5] Y. Hayashi and M. Ogata, *Possibility of Gapless Spin Liquid State by One-Dimensionalization*, J. Phys. Soc. Jpn. **76**, 053705 (2007).
- [6] M. Kohno, O. A. Starykh, and L. Balents, *Spinons and triplons in spatially anisotropic frustrated antiferromagnets*, Nat. Phys. **3**, 790 (2007).
- [7] M. Kohno, *Quasiparticles of Spatially Anisotropic Triangular Antiferromagnets in a Magnetic Field*, Phys. Rev. Lett. **103**, 197203 (2009).
- [8] D. Heidarian, S. Sorella, and F. Becca, *Spin- $\frac{1}{2}$ Heisenberg model on the anisotropic triangular lattice: From magnetism to a one-dimensional spin liquid*, Phys. Rev. B **80**, 012404 (2009).
- [9] L. Balents, *Spin liquids in frustrated magnets*, Nature **464**, 199 (2010).
- [10] T. Tay and O. I. Motrunich, *Variational studies of triangular Heisenberg antiferromagnet in magnetic field*, Phys. Rev. B **81**, 165116 (2010).
- [11] M.-A. Vachon, G. Koutroulakis, V. F. Mitrović, O. Ma, J. B. Marston, A. P. Reyes, P. Kuhns, R. Coldea, and Z. Tyłczyński, *The nature of the low-energy excitations in the short-range-ordered region of Cs_2CuCl_4 as revealed by ^{133}Cs nuclear magnetic resonance*, New J. Phys. **13**, 093029 (2011).

- [12] L. F. Tocchio, C. Gros, R. Valentí, and F. Becca, *One-dimensional spin liquid, collinear, and spiral phases from uncoupled chains to the triangular lattice*, Phys. Rev. B **89**, 235107 (2014).
- [13] R. Coldea, D. A. Tennant, K. Habicht, P. Smeibidl, C. Wolters, and Z. Tyłczyński, *Direct Measurement of the Spin Hamiltonian and Observation of Condensation of Magnons in the 2D Frustrated Quantum Magnet Cs_2CuCl_4* , Phys. Rev. Lett. **88**, 137203 (2002).
- [14] T. Radu, H. Wilhelm, V. Yushankhai, D. Kovrizhin, R. Coldea, Z. Tyłczyński, T. Lühmann, and F. Steglich, *Bose-Einstein Condensation of Magnons in Cs_2CuCl_4* , Phys. Rev. Lett. **95**, 127202 (2005).
- [15] T. Radu, Y. Tokiwa, R. Coldea, P. Gegenwart, Z. Tyłczyński, and F. Steglich, *Field induced magnetic phase transition as a magnon Bose Einstein condensation*, Sci. Technol. Adv. Mater. **8**, 406 (2007).
- [16] D. L. Kovrizhin, V. Yushankhai, and L. Siurakshina, *Bose-Einstein condensation of magnons in Cs_2CuCl_4 : A dilute gas limit near the saturation magnetic field*, Phys. Rev. B **74**, 134417 (2006).
- [17] V. Zapf, M. Jaime, and C. D. Batista, *Bose-Einstein condensation in quantum magnets*, Rev. Mod. Phys. **86**, 563 (2014).
- [18] M. Y. Veillette, J. T. Chalker, and R. Coldea, *Ground states of a frustrated spin- $\frac{1}{2}$ antiferromagnet: Cs_2CuCl_4 in a magnetic field*, Phys. Rev. B **71**, 214426 (2005).
- [19] Y. Tokiwa, T. Radu, R. Coldea, H. Wilhelm, Z. Tyłczyński, and F. Steglich, *Magnetic phase transitions in the two-dimensional frustrated quantum antiferromagnet Cs_2CuCl_4* , Phys. Rev. B **73**, 134414 (2006).
- [20] O. A. Starykh, H. Katsura, and L. Balents, *Extreme sensitivity of a frustrated quantum magnet: Cs_2CuCl_4* , Phys. Rev. B **82**, 014421 (2010).
- [21] C. Griset, S. Head, J. Alicea, and O. A. Starykh, *Deformed triangular lattice antiferromagnets in a magnetic field: Role of spatial anisotropy and Dzyaloshinskii-Moriya interactions*, Phys. Rev. B **84**, 245108 (2011).
- [22] R. Chen, H. Ju, H.-C. Jiang, O. A. Starykh, and L. Balents, *Ground states of spin- $\frac{1}{2}$ triangular antiferromagnets in a magnetic field*, Phys. Rev. B **87**, 165123 (2013).
- [23] O. A. Starykh, *Unusual ordered phases of highly frustrated magnets: a review*, Rep. Prog. Phys. **78**, 052502 (2015).
- [24] S. A. Zvyagin, D. Kamenskyi, M. Ozerov, J. Wosnitza, M. Ikeda, T. Fujita, M. Hagiwara, A. I. Smirnov, T. A. Soldatov, A. Y. Shapiro, J. Krzystek, R. Hu, H. Ryu, C. Petrovic, and M. E. Zhitomirsky, *Direct Determination of Exchange Parameters in Cs_2CuBr_4 and Cs_2CuCl_4 : High-Field Electron-Spin-Resonance Studies*, Phys. Rev. Lett. **112**, 077206 (2014).

- [25] M. Lang, B. Wolf, A. Honecker, L. Balents, U. Tutsch, P. T. Cong, G. Hofmann, N. Krüger, F. Ritter, W. Assmus, and A. Prokofiev, *Field-induced quantum criticality - application to magnetic cooling*, Phys. Status Solidi B **250**, 457 (2013).
- [26] A. Sytcheva, O. Chiatti, J. Wosnitza, S. Zherlitsyn, A. A. Zvyagin, R. Coldea, and Z. Tyliczynski, *Short-range correlations in quantum frustrated spin system*, Phys. Rev. B **80**, 224414 (2009).
- [27] A. Kreisel, P. Kopietz, P. T. Cong, B. Wolf, and M. Lang, *Elastic constants and ultrasonic attenuation in the cone state of the frustrated antiferromagnet Cs_2CuCl_4* , Phys. Rev. B **84**, 024414 (2011).
- [28] N. Krüger, S. Belz, F. Schossau, A. A. Haghishirad, P. T. Cong, B. Wolf, S. Gottlieb-Schoenmeyer, F. Ritter, and W. Assmus, *Stable Phases of the $Cs_2CuCl_{4-x}Br_x$ Mixed Systems*, Cryst. Growth Des. **10**, 4456 (2010).
- [29] P. T. Cong, B. Wolf, M. de Souza, N. Krüger, A. A. Haghishirad, S. Gottlieb-Schoenmeyer, F. Ritter, W. Assmus, I. Opahle, K. Foyevtsova, H. O. Jeschke, R. Valentí, L. Wiehl, and M. Lang, *Distinct magnetic regimes through site-selective atom substitution in the frustrated quantum antiferromagnet $Cs_2CuCl_{4-x}Br_x$* , Phys. Rev. B **83**, 064425 (2011).
- [30] K. Foyevtsova, I. Opahle, Y.-Z. Zhang, H. O. Jeschke, and R. Valentí, *Determination of effective microscopic models for the frustrated antiferromagnets Cs_2CuCl_4 and Cs_2CuBr_4 by density functional methods*, Phys. Rev. B **83**, 125126 (2011).
- [31] N. van Well, K. Foyevtsova, S. Gottlieb-Schönmeyer, F. Ritter, R. S. Manna, B. Wolf, M. Meven, C. Pfleiderer, M. Lang, W. Assmus, R. Valentí, and C. Krellner, *Low-temperature structural investigations of the frustrated quantum antiferromagnets $Cs_2Cu(Cl_{4-x}Br_x)$* , Phys. Rev. B **91**, 035124 (2015).
- [32] F. H. L. Essler, H. Frahm, F. Göhmann, A. Klümper, and V. E. Korepin, *The One-Dimensional Hubbard Model* (Cambridge University Press, Cambridge, 2005).
- [33] I. Dzyaloshinsky, *A thermodynamic theory of weak ferromagnetism of antiferromagnetics*, J. Phys. Chem. Solids **4**, 241 (1958).
- [34] T. Moriya, *Anisotropic Superexchange Interaction and Weak Ferromagnetism*, Phys. Rev. **120**, 91 (1960).
- [35] R. Coldea, *talk at KITP Conference Exotic Order and Criticality in Quantum Matter, 7–11 Jun 2004*, http://online.kitp.ucsb.edu/online/exotic_c04/coldea/.
- [36] Y. R. Wang and M. J. Rice, *Spin-1/2 on-site exclusion principle and two-dimensional spin-wave theory*, Phys. Rev. B **45**, 5045 (1992).
- [37] J. W. Negele and H. Orland, *Quantum Many-Particle Systems* (Addison-Wesley, Redwood City, CA, 1988).

- [38] R. D. Mattuck, *A Guide to Feynman Diagrams in the Many-Body Problem* (Dover, New York, 1992).
- [39] D. C. Mattis, *The Theory of Magnetism Made Simple* (World Scientific, Singapore, 2006).
- [40] T. Holstein and H. Primakoff, *Field Dependence of the Intrinsic Domain Magnetization of a Ferromagnet*, Phys. Rev. **58**, 1098 (1940).
- [41] M. Y. Veillette, A. J. A. James, and F. H. L. Essler, *Spin dynamics of the quasi-two-dimensional spin- $\frac{1}{2}$ quantum magnet Cs_2CuCl_4* , Phys. Rev. B **72**, 134429 (2005).
- [42] M. Y. Veillette and J. T. Chalker, *Commensurate and incommensurate ground states of Cs_2CuCl_4 in a magnetic field*, Phys. Rev. B **74**, 052402 (2006).
- [43] D. Dalidovich, R. Sknepnek, A. J. Berlinsky, J. Zhang, and C. Kallin, *Spin structure factor of the frustrated quantum magnet Cs_2CuCl_4* , Phys. Rev. B **73**, 184403 (2006).
- [44] E. Lieb, T. Schultz, and D. Mattis, *Two soluble models of an antiferromagnetic chain*, Ann. Phys. **16**, 407 (1961).
- [45] T. Giamarchi, *Quantum Physics in One Dimension* (Oxford University Press, Oxford, 2003).
- [46] T. Matsubara and H. Matsuda, *A Lattice Model of Liquid Helium, I*, Prog. Theor. Phys. **16**, 569 (1956).
- [47] E. G. Batyev and L. S. Braginskii, *Antiferromagnet in a strong magnetic field: analogy with Bose gas*, Sov. Phys. JETP **60**, 781 (1984).
- [48] B. Fausch, J. Stolze, and G. S. Uhrig, *Finite-temperature line shapes of hard-core bosons in quantum magnets: A diagrammatic approach tested in one dimension*, Phys. Rev. B **90**, 024428 (2014).
- [49] A. M. Tsvelik, *Quantum Field Theory in Condensed Matter Physics* (Cambridge University Press, Cambridge, UK, 1995).
- [50] A. M. Tsvelik, *New fermionic description of quantum spin liquid state*, Phys. Rev. Lett. **69**, 2142 (1992).
- [51] B. S. Shastry and D. Sen, *Majorana fermion representation for an anti-ferromagnetic spin-chain*, Phys. Rev. B **55**, 2988 (1997).
- [52] D. Foerster and F. Triozon, *Majorana representation of the quantum $O(N)$ Heisenberg antiferromagnet: Its success at $N = \infty$ and the reason for its failure at $N = 3$* , Phys. Rev. B **56**, 8069 (1997).
- [53] W. Mao, P. Coleman, C. Hooley, and D. Langreth, *Spin Dynamics from Majorana Fermions*, Phys. Rev. Lett. **91**, 207203 (2003).
- [54] A. Shnirman and Y. Makhlin, *Spin-Spin Correlators in the Majorana Representation*, Phys. Rev. Lett. **91**, 207204 (2003).

- [55] R. R. Biswas, L. Fu, C. R. Laumann, and S. Sachdev, *SU(2)-invariant spin liquids on the triangular lattice with spinful Majorana excitations*, Phys. Rev. B **83**, 245131 (2011).
- [56] J. Nilsson and M. Bazzanella, *Majorana fermion description of the Kondo lattice: Variational and path integral approach*, Phys. Rev. B **88**, 045112 (2013).
- [57] A. A. Abrikosov, *Electron scattering on magnetic impurities in metals and anomalous resistivity effects*, Physics **2**, 5 (1965).
- [58] V. Popov and S. Fedotov, *The functional-integration method and diagram technique for spin systems*, Sov. Phys. JETP **67**, 535 (1988).
- [59] S. A. Kulagin, N. Prokof'ev, O. A. Starykh, B. Svistunov, and C. N. Varney, *Bold diagrammatic Monte Carlo technique for frustrated spin systems*, Phys. Rev. B **87**, 024407 (2013).
- [60] S. A. Kulagin, N. Prokof'ev, O. A. Starykh, B. Svistunov, and C. N. Varney, *Bold Diagrammatic Monte Carlo Method Applied to Fermionized Frustrated Spins*, Phys. Rev. Lett. **110**, 070601 (2013).
- [61] J. Brinckmann and P. Woelfle, *Diagrammatic approximations for the 2d quantum antiferromagnet: exact projection of auxiliary fermions*, arXiv:0803.3312.
- [62] R. Agra, F. van Wijland, and E. Trizac, *On the free energy within the mean-field approximation*, Eur. J. Phys. **27**, 407 (2006).
- [63] A. Altland and B. Simons, *Condensed Matter Field Theory* (Cambridge University Press, Cambridge, UK, 2006).
- [64] H. T. C. Stoof, K. B. Gubbels, and D. B. M. Dickerscheid, *Ultracold Quantum Fields* (Springer, Dordrecht, The Netherlands, 2009).
- [65] O. A. Starykh and L. Balents, *Ordering in Spatially Anisotropic Triangular Antiferromagnets*, Phys. Rev. Lett. **98**, 077205 (2007).
- [66] R. Tamura and N. Kawashima, *First-Order Transition to Incommensurate Phase with Broken Lattice Rotation Symmetry in Frustrated Heisenberg Model*, J. Phys. Soc. Jpn. **77**, 103002 (2008).
- [67] E. M. Stoudenmire, S. Trebst, and L. Balents, *Quadrupolar correlations and spin freezing in $S = 1$ triangular lattice antiferromagnets*, Phys. Rev. B **79**, 214436 (2009).
- [68] S. Okumura, H. Kawamura, T. Okubo, and Y. Motome, *Novel Spin-Liquid States in the Frustrated Heisenberg Antiferromagnet on the Honeycomb Lattice*, J. Phys. Soc. Jpn. **79**, 114705 (2010).
- [69] R. L. Carlin, R. Burriel, F. Palacio, R. A. Carlin, S. F. Keij, and D. W. Carnegie, *Linear chain antiferromagnetic interactions in Cs_2CuCl_4* , J. Appl. Phys. **57**, 3351 (1985).

- [70] I. J. Pomeranchuk, *Stability of a Fermi Liquid*, Sov. Phys. JETP **8**, 361 (1958).
- [71] B. Lüthi, *Physical Acoustics in the Solid State* (Springer, Berlin, 2005).
- [72] Y. Zhou and P. A. Lee, *Spinon Phonon Interaction and Ultrasonic Attenuation in Quantum Spin Liquids*, Phys. Rev. Lett. **106**, 056402 (2011).
- [73] M. Serbyn and P. A. Lee, *Spinon-phonon interaction in algebraic spin liquids*, Phys. Rev. B **87**, 174424 (2013).
- [74] E. Pytte, *Peierls instability in Heisenberg chains*, Phys. Rev. B **10**, 4637 (1974).
- [75] R. A. T. de Lima and C. Tsallis, *Magnetic field influence on the spin-Peierls instability in the quasi-one-dimensional magnetostriuctive XY model: Thermodynamical properties*, Phys. Rev. B **27**, 6896 (1983).
- [76] R. B. Griffiths, *Magnetization Curve at Zero Temperature for the Anti-ferromagnetic Heisenberg Linear Chain*, Phys. Rev. **133**, A768 (1964).
- [77] S. Eggert, I. Affleck, and M. Takahashi, *Susceptibility of the spin 1/2 Heisenberg antiferromagnetic chain*, Phys. Rev. Lett. **73**, 332 (1994).
- [78] A. Klümper, *The spin-1/2 Heisenberg chain: thermodynamics, quantum criticality and spin-Peierls exponents*, Eur. Phys. J. B **5**, 677 (1998).
- [79] M. Mourigal, M. Enderle, A. Klöpperpieper, J.-S. Caux, A. Stunault, and H. M. Rønnow, *Fractional spinon excitations in the quantum Heisenberg antiferromagnetic chain*, Nat. Phys. **9**, 435 (2013).
- [80] B. Lake, D. A. Tennant, J.-S. Caux, T. Barthel, U. Schollwöck, S. E. Nagler, and C. D. Frost, *Multispinon Continua at Zero and Finite Temperature in a Near-Ideal Heisenberg Chain*, Phys. Rev. Lett. **111**, 137205 (2013).
- [81] L. N. Bulaevskii, *Theory of a linear anti-ferromagnetic chain*, Sov. Phys. JETP **16**, 685 (1963).
- [82] A. Kreisel, F. Sauli, N. Hasselmann, and P. Kopietz, *Quantum Heisenberg antiferromagnets in a uniform magnetic field: Nonanalytic magnetic field dependence of the magnon spectrum*, Phys. Rev. B **78**, 035127 (2008).
- [83] B. Fauschew and G. S. Uhrig, *Low-temperature thermodynamics of multiflavored hardcore bosons by the Brückner approach*, Phys. Rev. B **92**, 214417 (2015).
- [84] S. Sachdev, T. Senthil, and R. Shankar, *Finite-temperature properties of quantum antiferromagnets in a uniform magnetic field in one and two dimensions*, Phys. Rev. B **50**, 258 (1994).
- [85] M. Frigo and S. Johnson, *The Design and Implementation of FFTW3*, Proc. IEEE **93**, 216 (2005).

- [86] H.-P. Liu and D. D. Kosloff, *Numerical evaluation of the Hilbert transform by the Fast Fourier Transform (FFT) technique*, Geophys. J. Royal Astr. Soc. **67**, 791 (1981).
- [87] J. Moreno and J. M. Soler, *Optimal meshes for integrals in real- and reciprocal-space unit cells*, Phys. Rev. B **45**, 13891 (1992).

Danksagung

Ich möchte hier am Ende die Gelegenheit nutzen, um allen Menschen zu danken, die einen Beitrag zum Gelingen dieser Arbeit geleistet haben.

Meinem Betreuer Peter Kopietz danke ich für die Möglichkeit in seiner Arbeitsgruppe forschen zu können – angefangen bei der Bachelor-Arbeit bis zur Promotion. Besonders hervorheben möchte ich, dass er mir bei meiner Forschung eine sehr große Freiheit gelassen hat und mich stets bei meinen Forschungsprojekten unterstützt hat.

Roser Valentí danke ich für die Übernahme des Zweitgutachtens.

Axel Pelster danke ich für die Organisation der Studentenseminare des SFB/TR49 und für interessante Diskussionen.

Ein besonderer Dank gilt den Menschen, die direkt an meiner Forschung beteiligt waren: Tim Herfurth, der einen wesentlichen Beitrag zum ersten Teil dieser Arbeit geleistet hat, Pham Thanh Cong, der die Ultraschallexperimente, die im zweiten Teil eine zentrale Rolle spielen, durchgeführt hat, und natürlich Peter Kopietz, der an allen drei Teilen mitgewirkt hat. Zudem möchte ich den Kristallzüchtern Natalija van Well, Franz Ritter und Wolf Aßmus danken, ohne deren Cs_2CuCl_4 -Kristalle die Ultraschallexperimente nicht möglich gewesen wären. Aus den Diskussionen mit Michael Lang, Lars Postulka und Bernd Wolf gingen wichtige Beiträge und Anregungen für den zweiten und dritten Teil dieser Arbeit hervor.

Abschließend danke ich allen Mitgliedern der Arbeitsgruppe Kopietz, des Instituts für Theoretische Physik und des SFB/TR49 für die vielen interessanten Seminarvorträge und Diskussionen.

Simon Streib

Lebenslauf



Persönliche Daten

Name Simon Streib
 Geburtsdatum 30. Juli 1987
 Geburtsort Frankfurt am Main, Deutschland
 Nationalität Deutsch

Ausbildung und beruflicher Werdegang

- 11.01.2016 **Promotion mit Auszeichnung.**
- 2013–2016 **Doktorand**, Goethe-Universität, Frankfurt.
Am Institut für Theoretische Physik.
Betreuer: Prof. Dr. Peter Kopietz
- 2011–2013 **Master Physik**, Goethe-Universität, Frankfurt.
Note: sehr gut (1,0)
Masterarbeit: Solution of the Anderson Impurity Model via the Functional Renormalization Group
Betreuer: Prof. Dr. Peter Kopietz
- 2008–2011 **Bachelor Physik**, Goethe-Universität, Frankfurt.
Note: sehr gut (1,2)
Bachelorarbeit: Functional Renormalization Group Approach to the Anderson Impurity Model
Betreuer: Prof. Dr. Peter Kopietz
- 2012–2013 **Lehrassistent**, Goethe-Universität, Frankfurt.
- 2007–2008 **Zivildienst**, Goethe-Universität, Frankfurt.
Prof. Dr. Kopp, Carolinum, Universitätsklinikum.
- 2007 **Abitur**, Heinrich-von-Gagern-Gymnasium, Frankfurt.
Note: sehr gut (1,0)